Technical Physics Letters, Vol. 30, No. 3, 2004, pp. 173–174. Translated from Pis'ma v Zhurnal Tekhnicheskoĭ Fiziki, Vol. 30, No. 5, 2004, pp. 1–5.

The Efficiency of an Optical Heat Pump in the Inverse Thermodynamic Cycle

S. N. Andrianov* and Yu. E. Polsky

State Institute of Applied Optics, Federal Unitary Enterprise, Kazan, Tatarstan, Russia

** e-mail: andrianov@bancorp.ru*

Received July 24, 2003

Abstract—Proceeding from the first law of thermodynamics and the laws of radiation, an expression for the efficiency of an optical heat pump in the inverse thermodynamic cycle is derived in terms of the system parameters. Based on these relations, general requirements to the parameters of an optical heat pump are formulated that can be used in designing real devices. © *2004 MAIK "Nauka/Interperiodica".*

In recent years, much attention has been devoted to the phenomenon of laser cooling of solids [1, 2] with a view to numerous expected technological applications. In this context, it is very important to study the efficiency of an optical heat pump in the inverse thermodynamic cycle. This problem has been extensively investigated [3–6] using the thermodynamic approach of Landau [7] to the description of photoluminescence. In these investigations, the thermodynamic efficiency was expressed through a change in the entropy of the radiation entering into the optical heat pump and that outgoing from the device. This approach implies the knowledge of the spectral density of the radiation under consideration and requires obtaining additional experimental data.

In constructing a real technological system, it would be convenient to have an expression for the efficiency in terms of the parameters of this system not requiring preliminary experimentation. In the aforementioned papers [3–6], the efficiency of the Carnot cycle (i.e., the limiting efficiency with neglect of the entropy increment inside the sample) was calculated, while the efficiencies of energy conversion in the direct [4] and inverse [5, 6] thermodynamic cycles were only roughly estimated.

Below, we will derive an expression for the energy conversion efficiency in the inverse thermodynamic cycle of an optical heat pump, proceeding from the first law of thermodynamics and the Bouguer–Beer and Stefan–Boltzmann radiation laws. Based on these relations, we will give practical recommendations for constructing optical refrigerators.

Following [3–7], the first law of thermodynamics for an optical heat pump in the inverse thermodynamic cycle can be written as

$$W = Q_1 + Q_2, \tag{1}$$

where Q_1 is the heat supplied with an external radiation to a body, Q_2 is the heat removed from this body via radiation, and $W = W_1 + W_2$ is the energy taken by the working body from the cold body during transitions between the corresponding sublevels in the anti-Stokes model of laser cooling (see figure). Equation (1) takes into account only the radiative heating from the environment and ignores small additions related to the contact heat exchange with the ambient medium as well as the heat evolution due to radiation scattering and relaxation processes in the working body. In the case under consideration, we have

$$W = P_1\tau, \tag{2}$$

where P_1 is the cooling power and τ is the observation

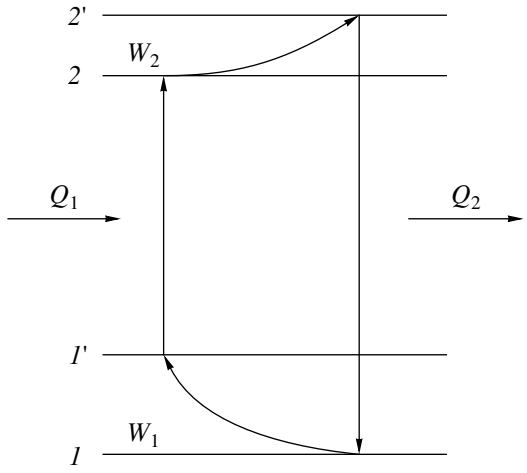

A schematic diagram showing the working electron levels (*1*, *2*), vibrational sublevels (*1*', *2*'), and resonance transitions in the working body: pumping laser radiation with the energy Q_1 and the frequency ν_4 induces the *1*' ⟶ *2* transition that takes the energy W_1 from the oscillatory system. Then, the energy W_2 is taken and the system exhibits fluorescence with the energy Q_2 at the frequency ν.

1063-7850/04/3003-0173$26.00 © 2004 MAIK "Nauka/Interperiodica"

time, and

$$Q_1 = (P_2 + P_3)\tau, \quad (3)$$

where P_2 is the incident laser radiation power and P_3 is the radiative heating power.

Using the Bouguer–Beer law and the results of Lamouche *et al.* [8], we obtain

$$P_1 = P_2\frac{\Delta\nu}{\nu_4}(1 - e^{-\alpha L}), \quad (4)$$

where ν_4 is the frequency of absorbed radiation, $\Delta\nu$ is the detuning of the central fluorescence frequency from the pump frequency in the longwave wing of the absorption line contour, α is the coefficient of optical absorption at the pump frequency, and L is the optical pathlength of the pumping radiation in the working body. According to the Stefan–Boltzmann law for blackbody radiation, we have

$$P_3 = \sigma S T_0^4, \quad (5)$$

where σ is the Stefan–Boltzmann constant, S is the surface area of the working body, and T_0 is the thermostat temperature. Finally, an expression for the efficiency of an optical heat pump in the inverse thermodynamic cycle takes the following form:

$$\kappa = \left|\frac{W}{Q_1}\right| = \frac{\Delta\nu(1 - e^{-\alpha L})}{\nu_4(1 + \sigma S T_0^4/P_2)}. \quad (6)$$

For $\alpha L \ll 1$, this relation simplifies to

$$\kappa_I = \frac{\Delta\nu\alpha L}{\nu_4(1 + \sigma S T_0^4/P_2)}. \quad (7)$$

As can be seen from Eq. (7), the efficiency increases for optically thin samples with increasing absorption and optical pathlength of the pumping radiation. In the case of optically thick samples ($\alpha L \gg 1$), relation (6) yields

$$\kappa_{II} = \frac{\Delta\nu}{\nu_4(1 + \sigma S T_0^4/P_2)}. \quad (8)$$

A comparison of expressions (7) and (8) shows that $\kappa_I < \kappa_{II} < 1$. Equation (8) indicates that the efficiency decreases with increasing ambient temperature and the working body surface area and increases with the pump power. For a sufficiently large pump power, we can approximately write

$$\kappa_{II} = \frac{\Delta\nu}{\nu_4}. \quad (9)$$

This formula shows that, for a constant detuning, the efficiency increases with decreasing pump frequency.

To summarize, the obtained expressions indicate that the efficiency of an optical heat pump grows with increasing permissible spectral detuning, increasing optical thickness of the working body, decreasing working body surface area and ambient temperature, increasing power of the incident laser radiation, and decreasing resonance transition frequency of the working impurity. However, it should be taken into account that

(i) an increase in the optical pathlength at the expense of absorption increasing due to a higher impurity concentration is well known to result in the luminescence quenching, which terminates laser cooling;

(ii) the possibility to increase the efficiency by increasing the incident radiation power is limited by the processes leading to saturation;

(iii) a decrease in the resonance transition frequency is limited by the increasing probability of multiphonon relaxation, which also terminates laser cooling.

Acknowledgments. This study was supported by the International Scientific-Technological Center (grant no. 2121), the Russian Foundation for Basic Research (project no. 01-02-17730a), and the Integration Program (project no. B0019).

REFERENCES

1. R. I. Epstein, M. I. Buchwald, B. C. Edwards, *et al.*, Nature **377**, 500 (1995).
2. C. W. Hoit, M. P. Hasselbeck, M. Sheik-Bahae, *et al.*, J. Opt. Soc. Am. B **20** (5), 1 (2003).
3. Yu. P. Chukova, *Anti-Stokes Luminescence and Its New Applications* (Radio i Svyaz', Moscow, 1980).
4. P. T. Landsberg and G. Tonge, J. Appl. Phys. **51** (7), R1 (1980).
5. R. Kosloff, E. Geva, and J. M. Gordon, J. Appl. Phys. **87**, 8093 (2000).
6. J. P. Palao, R. Kosloff, and J. M. Gordon, Phys. Rev. E **64**, 056130 (2001).
7. L. D. Landau, J. Phys. (Moscow) **10**, 503 (1946).
8. G. Lamouche, P. Lavallard, R. Suris, *et al.*, J. Appl. Phys. **84**, 509 (1998).

Translated by P. Pozdeev

Technical Physics Letters, Vol. 30, No. 3, 2004, pp. 175–177. Translated from Pis'ma v Zhurnal Tekhnicheskoĭ Fiziki, Vol. 30, No. 5, 2004, pp. 6–13.

A Change in the Character of Modulation Instability in the Vicinity of a Critical Frequency

A. A. Balyakin* and N. M. Ryskin**

Saratov State University, Saratov, Russia

*e-mail: * BalyakinAA@info.sgu.ru; ** RyskinNM@info.sgu.ru*

Received July 18, 2003; in final form, September 10, 2003

Abstract—Modulation instability of a quasi-harmonic wave propagating in a cubic nonlinear medium is analyzed in the vicinity of a critical frequency. As the wave amplitude increases, the character of instability changes from convective to absolute. This is explained by expansion of the range of unstable perturbations to the region of counterpropagating waves possessing a negative group velocity. The proposed theory is confirmed by the results of computer simulations. *© 2004 MAIK "Nauka/Interperiodica".*

A plane quasi-monochromatic wave propagating in a cubic nonlinear dispersive medium is usually described by the nonlinear Schrödinger equation [1–4],

$$i\left(\frac{\partial A}{\partial t} + V\frac{\partial A}{\partial x}\right) + \frac{\omega_0''}{2}\frac{\partial^2 A}{\partial x^2} + \beta|A|^2 A = 0. \qquad (1)$$

Here, A is the slowly varying complex wave amplitude, ω is the carrier wave frequency, $V = \partial\omega/\partial k$ is the group velocity, $\omega_0'' = \partial^2\omega/\partial k^2$ is the dispersion parameter, and β is the nonlinearity parameter. The simplest solution of Eq. (1) has the form of a monochromatic wave with a constant amplitude $A(x, t) = A_0\exp[i(kx - \omega t)]$, where the frequency ω and wavenumber k obey the nonlinear dispersion relation

$$\omega = kV + \omega_0'' k^2/2 - \beta A_0^2. \qquad (2)$$

If the medium is such that $\omega_0''\beta > 0$, the solution is known to be unstable with respect to slow modulations with the frequencies within a certain interval in the vicinity of the carrier frequency, or, in other words, the system exhibits modulation instability [1–4]. Without loss of generality, we assume below that $\omega_0'' > 0$ and $\beta > 0$.

Like any other instability, the modulation instability can be either absolute or convective. Obviously, the character of instability determines the wave propagation process. Consider a bounded medium excited at the left boundary ($x = 0$) with a harmonic signal $A(0, t) = A_0\exp(-i\omega t)$. In the case of a convective instability, growing perturbations will drift to the right and leave the system via the right-hand boundary. Upon termination of a transient process, a single-frequency regime will be attained. If the instability is absolute, perturbations will be continuously generated along the entire system, which will lead to a multifrequency regime. Moreover, physical and numerical experiments performed within the framework of investigations devoted to the propagation of nonlinear magnetostatic waves showed that irregular regimes of chaotic oscillations with a continuous spectrum may exist for a sufficiently large intensity of the input signal [5–7]. It should be emphasized that these phenomena possess an autooscillatory character and cannot be explained by the amplification of fluctuations.

Now, we will formulate a simple criterion that allows the character of instability to be determined. Following the usual approach to the analysis of instabilities [1–4], let us add a small perturbation to the monochromatic solution in the form of two satellites symmetric with respect to the carrier frequency. A dispersion relation between the frequency Ω and the wavenumber of these perturbations has the following form,

$$(\Omega - Kv_g(\omega))^2 = (\omega_0'' K^2/2)^2 - \beta\omega_0''|A_0|^2 K^2, \qquad (3)$$

where $v_g(\omega) = V + \omega_0'' k$ is the group velocity at a frequency ω. A conventional approach to the analysis of modulation instability consists in assuming K to be real, which allows relation (3) to be written in the form $\Omega = Kv_g(\omega) \pm i\lambda(K)$, where $\lambda(K) = [\beta\omega_0''|A_0|^2K^2 - (\omega_0'' K^2/2)^2]^{1/2}$ is the instability growth rate [1–4]. Perturbations with the wavenumbers falling within the interval $K^2 < K_0^2 = 4\beta|A_0|^2/\omega_0''$ are unstable. Perturbations with the wavenumber $K_m = K_0/\sqrt{2}$ are characterized by the maximum growth rate.

However, this is insufficient for determining the character of instability. We use the well-known method based on an analysis of the asymptotic expression for

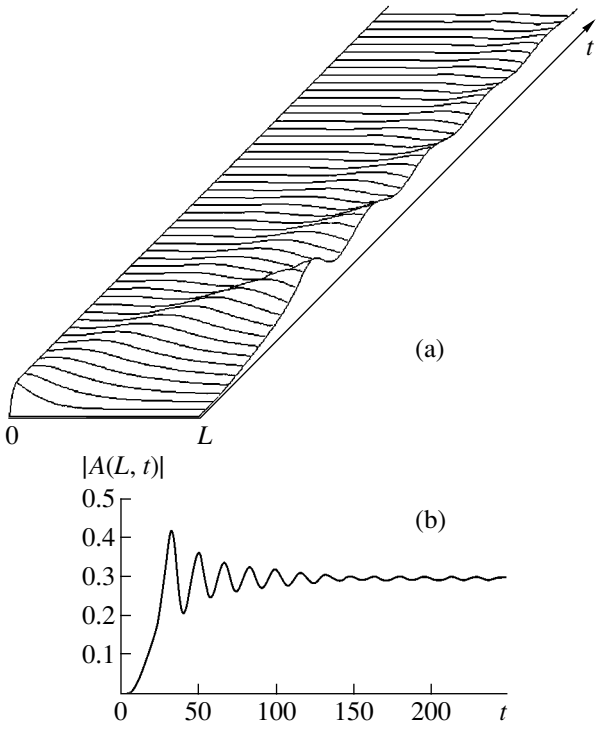

Fig. 1. Wave propagation in a system with convective instability (V = 1.2, A_0 = 0.3): (a) spatiotemporal dynamics; (b) waveform at the point L = 10.

perturbations calculated using the method of steepest descent (see, e.g., [4, Ch. 12]). Here, both Ω and K in relation (3) are treated as complex quantities. After simple but somewhat lengthy calculations (to be published separately), we arrive at a criterion of absolute instability, that is, a condition under which perturbations increase with time at a certain point of space:

$$\beta|A_0|^2 > V^2/2\omega_0'' + \omega. \quad (4)$$

This relation implies that, for a fixed external signal frequency, an increase in the signal intensity will lead to a nonlinear effect whereby the character of instability will change from convective to absolute.

From the standpoint of physics, a change in the character of instability is explained as follows. The parabolic dispersion law (2) admits the propagation of waves with frequencies above the critical frequency $\omega_c = -V^2/2\omega_0'' - \beta|A_0|^2$ that depends on the amplitude. This frequency corresponds to a critical wavenumber $k_c = -V/\omega_0''$. Then, condition (4) can be rewritten in the following form:

$$k - K_0 < k_c, \quad (5)$$

where k and K_0 depend on the amplitude. Assuming the frequency ω to be given, we can use relation (2) to determine the carrier wavenumber $k(\omega, A_0)$. In this case, it is necessary to select a root corresponding to the wave propagating from left to right. Since perturbations with the wavevectors in the interval $[k - K_0; k + K_0]$ are unstable, criterion (5) indicates that an instability is absolute if there are increasing perturbations with a negative group velocity. This leads to an internal distributed feedback necessary for the excitation of self-oscillations. As a result, the monochromatic state loses stability and a self-modulation appears manifested by periodic oscillations in the wave amplitude. The self-modulation frequency can be determined by substituting a threshold value of the amplitude into the expression for the critical frequency:

$$\omega_a = -\omega - V^2/\omega_0''. \quad (6)$$

It should be noted that important factors in this case are the existence of a critical frequency and the presence of waves with a negative group velocity. On the other hand, a description in terms of the nonlinear Schrödinger equation is approximate and is based on the approximation of the dispersion relation of a real system by a parabola, which is valid only in a certain vicinity of the carrier frequency [2, 4]. If the initial dispersion law does not admit counterpropagating waves, the modulation instability can be only convective. In this case, the transition to the absolute instability determines the boundaries of applicability of the model employing Eq. (1). Nevertheless, the situation considered in this study is typically encountered in many important problems, for example, those pertaining to the propagation of waves in various periodic nonlinear structures.

The above conclusions are confirmed by the results of numerical solution of Eq. (1) with the left boundary condition in the form $A(0, t) = A_0 \tanh(t)\exp(-i\omega t)$, which provides for a smooth increase in the input signal amplitude. The initial condition was selected in the form $A(x, t = 0) = 0$. In order to exclude the effects of reflection and realize the regime of unidirectional propagation, the condition on the right boundary corresponded to the so-called perfectly matched layers. According to this, the region of interest is assumed to possess a finite length L and damping with the coefficient gradually increasing with the coordinate is introduced into Eq. (1) at $x > L$. The numerical calculations were performed in a broad range of control parameters. For definiteness, all the results present below correspond to $\beta = 1$, $\omega_0''/2 = 1$, $\omega = 0$ (the other parameters are specified in legends to the figures).

Figures 1 and 2 give examples of the spatiotemporal dynamics and time variation of the amplitude at $x = L$ in the regimes of convective and absolute instability, respectively. As can be seen in first case, perturbations appearing on the leading front drift to the right and leave the system via the right-hand boundary. At a fixed

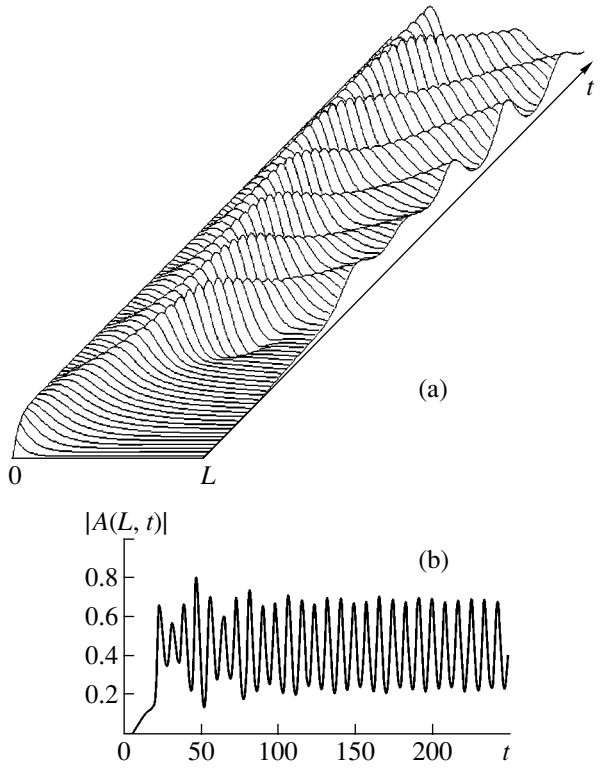

Fig. 2. Wave propagation in a system with the absolute instability ($V = 1.4$, $A_0 = 0.6$): (a) spatiotemporal dynamics; (b) waveform at the point $L = 10$.

point, the amplitude oscillations gradually decay and a single-frequency wave propagation regime with a constant wave amplitude is established. In the case of absolute instability, the increasing perturbations are continuously generated along the entire system length and a self-modulation regime is established with a periodically oscillating signal amplitude. Note that the numerically calculated instability threshold and self-modulation frequency are completely consistent with theoretical values (4) and (6), respectively. Since the fundamental and self-modulation frequencies in the general case do not obey the resonance relationship, the system exhibits two-frequency quasiperiodic oscillations. As the input signal intensity grows, the self-modulation depth increases and the signal at the point $x = L$ acquires the form of a sequence of soliton-like pulses.

When the absolute instability threshold is significantly exceeded, the oscillations acquire a chaotic character. The main form of transition to chaos, known as the Ruelle–Takens scenario, is via breakage of a quasiperiodic regime. The results of calculations illustrating the transition to chaos are qualitatively analogous to those reported by Dudko *et al.* [6, 7] and are not presented here. However, the works cited did not reveal a relationship with the transition from convective to absolute instability and with the proximity to the critical frequency. It is difficult to perform direct quantitative comparison because the analysis in [6, 7] was performed for the case of a strongly dissipative medium. Since the nonlinear Schrödinger equation plays the role of a universal model describing the propagation of a wave packet envelope in a dispersive medium [1–4], the obtained results are of interest from the standpoint of elucidating the nature of spatiotemporal chaos (turbulence).

The regimes of periodic self-modulation involving generation of the sequences of solitons are also of interest from the standpoint of obtaining ultrashort pulses. Here, it is interesting to note an obvious analogy with the recently reported experimental observation of similar regimes in the so-called "active ring" [8], whereby the output of a nonlinear system is connected to the input via a feedback chain involving a broadband amplifier. In our case, an advantage consists in that there is no need for any additional elements since the absolute instability provides for the internal feedback. Because of a small group velocity, a soliton is formed over a short distance and the length of a nonlinear medium can be not very large.

Acknowledgments. This study was supported by the US Civilian Research and Development Foundation for the Independent States of the Former Soviet Union (CRDF Award No. REC-006) and the Russian Foundation for Basic Research (project nos. 03-02-06257 and 03-02-16192).

REFERENCES

1. G. B. Whitham, *Linear and Nonlinear Waves* (Wiley, New York, 1974; Mir, Moscow, 1977).
2. R. K. Dodd, J. C. Eilbeck, J. Gibbon, and H. C. Morris, *Solitons and Nonlinear Wave Equations* (Academic Press, New York, 1982; Mir, Moscow, 1988).
3. A. C. Newell, *Solitons in Mathematics and Physics* (SIAM, Philadelphia, 1985; Mir, Moscow, 1989).
4. N. M. Ryskin and D. I. Trubetskov, *Nonlinear Waves* (Nauka, Moscow, 2000).
5. B. A. Kalinikos, N. G. Kovshikov, and A. N. Slavin, Zh. Éksp. Teor. Fiz. **94**, 159 (1988) [Sov. Phys. JETP **67**, 303 (1988)].
6. G. M. Dudko, G. T. Kazakov, A. V. Kozhevnikov, and Yu. A. Filimonov, Pis'ma Zh. Tekh. Fiz. **13**, 736 (1987) [Sov. Tech. Phys. Lett. **13**, 306 (1987)].
7. G. M. Dudko and Yu. A. Filimonov, Pis'ma Zh. Tekh. Fiz. **15**, 55 (1989) [Sov. Tech. Phys. Lett. **15**, 61 (1989)].
8. B. A. Kalinikos, N. G. Kovshikov, M. P. Kostylev, and H. Benner, Pis'ma Zh. Éksp. Teor. Fiz. **76**, 310 (2002) [JETP Lett. **76**, 253 (2002)].

Translated by P. Pozdeev

Technical Physics Letters, Vol. 30, No. 3, 2004, pp. 178–179. Translated from Pis'ma v Zhurnal Tekhnicheskoĭ Fiziki, Vol. 30, No. 5, 2004, pp. 14–17.

Probing Hydrogen Molecules with a Laboratory Raman Lidar

E. I. Voronina, V. E. Privalov*, and V. G. Shemanin

St. Petersburg State Technical University, St. Petersburg, 195251 Russia

** e-mail: VEP@peterlink.ru*

Received July 16, 2003

Abstract—The intensity of Raman backscattering from molecular hydrogen in a cell was studied by Raman lidar as a function of the sounding distance. From these data, the differential Raman scattering cross section of hydrogen molecules at a wavelength of 532 nm is determined for sounding distances within 2 m. © *2004 MAIK "Nauka/Interperiodica".*

At present, there are lidars of various types that can be used for monitoring the molecules of gases present in the atmosphere. The development of lidar measurements of the concentration of molecular hydrogen in technological gaseous mixtures of various compositions, including pure hydrogen, is of interest in view of the wide use of H_2 as a heat-transfer agent and a fuel [1–4]. Previously [3–5], we have numerically solved the lidar equation for various types of lidars and established that the most favorable technique for detecting low concentrations of hydrogen molecules at large distances is offered by the Raman lidar technique.

This study was aimed at experimental investigation of the dependence of the intensity of Raman backscattering from pure molecular hydrogen contained in a special cell on the distance of sounding by a Raman lidar.

The experiments were performed with a laboratory lidar prototype (Fig. 1) [6] with a sounding distance of up to 8 m, employing a pulsed YAG:Nd laser operating at a radiation wavelength of 532 nm, a pulse duration of 10 ns, and an energy of 10 mJ. The probing laser beam was incident at the Brewster angle onto a gas cell of special design filled with pure molecular hydrogen. The Raman backscattering signal was measured at a distance of up to 2 m by means of the Newton type telescope with an 0.4-m-diam spherical mirror. The collected light passed through a special optical filter with the maximum transmission at a Raman scattering wavelength of 684 nm and a transmission band halfwidth of 5 nm and was detected by a FEU-79 photomultiplier. The output voltage pulses of the detector were recorded by an S8-14 storage oscillograph and fed to a microprocessor-based measuring system [6]. The measurements were multiply repeated (up to 15 runs).

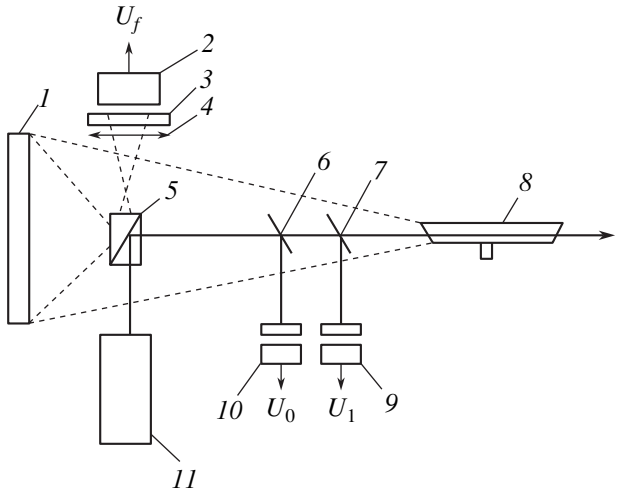

Fig. 1. Schematic diagram of the experimental setup: (*1*) spherical mirror; (*2*) photomultiplier; (*3*) interference filter; (*4*) lens; (*5*) tilting prism; (*6*, *7*) glass plates; (*8*) gas cell; (*9*, *10*) photodiodes; (*11*) laser.

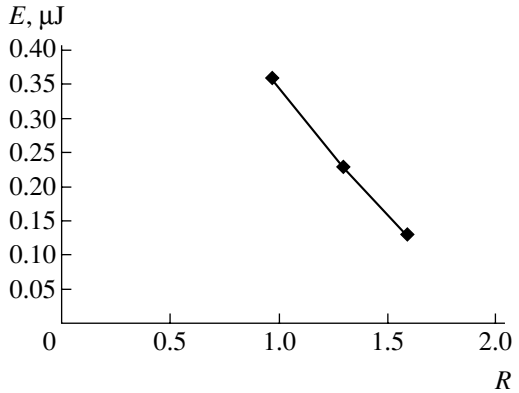

Fig. 2. A plot of the pulse energy E versus sounding distance R for the Raman backscattering from molecular hydrogen.

1063-7850/04/3003-0178$26.00 © 2004 MAIK "Nauka/Interperiodica"

The averaged pulse amplitudes are presented in the third column of the table.

In order to convert the Raman signal amplitude into a pulse energy, we performed special calibration experiments and determined the transfer coefficient of the photodetector employing an FEU-79 photomultiplier. This calibration was performed using the second-harmonic radiation with a wavelength of 532 nm, attenuated by calibrated neutral optical filters and detected by a photomultiplier operating in the working range of control voltages. The laser pulse energies were determined using an IMO-2M power meter. The transmission coefficient determined in this way, $K = 0.375 \pm 0.064$ μJ/V, was used to calculate the Raman scattering pulse energies presented in the fourth column in the table. Figure 2 shows a plot of the calculated pulse energy E of Raman scattering from molecular hydrogen versus the lidar sounding distance R.

Using a numerical solution of the Raman lidar equation [3] with the parameters of the lidar employed in this study, we determined the differential cross section of Raman scattering for hydrogen molecules excited by laser radiation with a wavelength of 532 nm: $(d\sigma/d\Omega)_F = (4.3 \pm 0.97) \times 10^{-30}$ cm^2/sr. This result is in good agreement with a published value of 1.4×10^{-30} cm^2/sr [2].

Thus, our experimental results confirm the possibility of using remote probing by Raman lidar for detecting molecular hydrogen. Processing of the results of measurements gave the differential cross section of Raman scattering for hydrogen molecules probed by laser radiation with a wavelength of 532 nm at a distance of up to 2 m.

Raman signal intensities and pulse energies for various distances of lidar sounding

R, m	U_R, V	ΔU_R, V	$E(R)$, μJ
0.97	0.95	0.12	0.36
1.3	0.68	0.18	0.23
1.6	0.35	0.21	0.13

REFERENCES

1. V. E. Privalov, V. B. Smirnov, and V. G. Shemanin, Calculating the Parameters of Remote Laser Probing of Molecular Hydrogen (A Preprint) (Russian Center of Laser Physics, St. Petersburg, 1998).
2. R. M. Measures, *Laser Remote Sensing: Fundamentals and Applications* (Wiley, New York, 1984; Mir, Moscow, 1987).
3. V. E. Privalov and V. G. Shemanin, Opt. Spektrosk. **82**, 873 (1997) [Opt. Spectrosc. **82**, 809 (1997)].
4. G. V. Laktyushkin, V. E. Privalov, and V. G. Shemanin, Zh. Tekh. Fiz. **68** (1), 20 (1998) [Tech. Phys. **43**, 16 (1998)].
5. V. E. Privalov and V. G. Shemanin, Proc. SPIE **3403**, 276 (1998).
6. E. I. Voronina, V. E. Privalov, and V. G. Shemanin, Opt. Spektrosk. **93**, 699 (2002) [Opt. Spectrosc. **93**, 643 (2002)].

Translated by P. Pozdeev

Technical Physics Letters, Vol. 30, No. 3, 2004, pp. 180–182. Translated from Pis'ma v Zhurnal Tekhnicheskoĭ Fiziki, Vol. 30, No. 5, 2004, pp. 18–22.

Fatigue Testing of Materials under Extremal Conditions by Acoustic Method

V. M. Baranov*, Yu. K. Bibilashvili, V. A. Karasevich, and G. A. Sarychev

Moscow Institute of Engineering Physics (State University), Moscow, 115409 Russia

** e-mail: bar@kpu.mephi.ru*

Received July 7, 2003

Abstract—Increasing fuel cycle time requires fatigue testing of the fuel clad materials for nuclear reactors. The standard high-temperature fatigue tests are complicated and tedious. Solving this task is facilitated by the proposed acoustic method, which ensures observation of the material damage dynamics, monitoring of the experimental parameters, and determination of the dynamic yield stress. Ring samples cut from zirconium cladding tubes were irradiated with fast neutrons to a total fluence of 2.2×10^{26} m^{-2} and fatigue tested at temperatures up to 360–400°C, including the tests in an iodine vapor—a uranium fission product capable of inducing corrosion cracking of the fuel elements. © *2004 MAIK "Nauka/Interperiodica"*.

We have developed methods [1] and designed special capsules for fatigue testing ring samples cut from fuel cladding tubes. A sample with a height of 1–5 mm, an external diameter of 9.15 mm, and a thickness of 0.7 mm is placed into a small hermetically sealed cylindrical capsule with a diameter of 32 mm and a height of 70 mm. Excited by electromagnetic field, the sample is an element of the oscillatory system involving the mobile and immobile clamps. The immobile clamp is welded to one end of a long rod introduced into the capsule via a welded joint, the other end being in contact with a piezoelectric gauge detecting the acoustic waves. The acoustic signal is used for monitoring the development of fatigue cracks by detecting acoustic emission, counting the number of cycles, and determining the moment of sample fracture. It is also possible to monitor the aggressive medium in the capsule (by detecting the acoustic noise due to evaporation), determine the sample temperature (by measuring the resonance frequency of the oscillatory system), control the quality of sample fixation in the clamps (by detecting the signals due to the sample slack), and study the amplitude dependence of the system damping constant (decrement) for evaluation of the dynamic yield stress.

A block scheme of the measuring system is depicted in the figure. A PZT ceramic piezoelectric gauge (TsTS-26 type) receives the acoustic signal via a 30-cm-long rod-shaped waveguide with a diameter of 5 mm introduced via a welded joint into the hermetic capsule. The sample is clamped in the capsule between a fixed clamp welded to the other end of the rod and a mobile clamp bearing a load. Made of a magnetic material, the load acts as a pendulum driven by an external magnetic field. The capsule can be filled with an aggressive test medium from a vapor generator containing crystalline iodine. When the generator is heated, iodine evaporates and the heavy vapor gradually displaces air (via a capillary in the top lid) and fills the whole capsule volume.

The capsule is placed between the poles of an electromagnet. During the test, the oscillatory system is either excited at a resonance frequency to perform vibrations in the sample plane or is driven to tilt about a horizontal axis between poles of the magnet, whereby the load exhibits cyclic displacements from one wall to the opposite and deforms the sample. The maximum

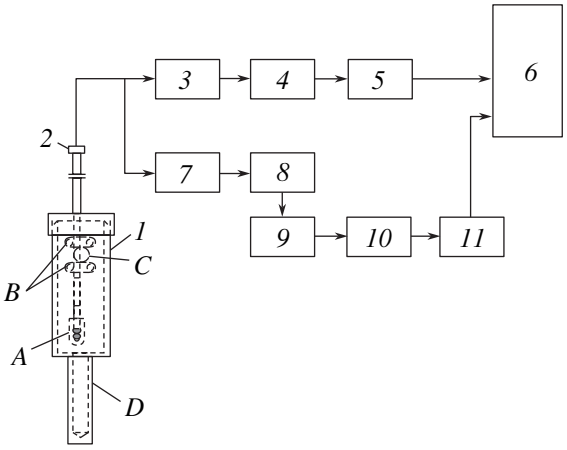

Schematic diagram of the test capsule and a block scheme of the measuring and data processing system: (*1*) capsule with a sample; (*2*) piezoelectric gauge; (*3*, *7*) amplifiers; (*4*) low-pass filter; (*5*, *11*) interfaces; (*6*) computer; (*8*) high-pass filter; (*9*) frequency converter; (*10*) amplitude demodulator; (*A*) load; (*B*) clamps; (*C*) sample; (*D*) vapor generator.

1063-7850/04/3003-0180$26.00 © 2004 MAIK "Nauka/Interperiodica"

angle of deviation is controlled by moving the load along the threaded holder. The cycle asymmetry can be varied by setting the side shift of the sample in the clamps and by rotating the load in the vertical plane. Precise setting of the loading cycle parameters is achieved through fine adjustment in a transparent model of the capsule that allows visual control of the sample deformation. A detailed analysis of sample straining was performed by optical method using a large-scale model of the measuring unit and ring-shaped samples made of polyethylene tubes with a diameter of 63 mm for gas pipelines. The model samples were cut so as to ensure their geometric similarity to the test samples of clad materials.

The acoustic response signals were monitored in two channels, low- and high-frequency, and the data were recorded onto hard or compact disks. The real sensitivity of the system was improved by using computer processing of the signals including procedures of the optimum filtration, high-precision amplitude and frequency demodulation, and the spectral, correlation, and wavelet analysis techniques. The signal of acoustic emission was separated as the high-frequency component of the piezoelectric response within a narrow frequency band in the vicinity of the natural resonance in a frequency interval from 50 to 1000 kHz. The channel of the acoustic emission measurements corresponds to the lower branch of the block scheme. The amplitude-modulated signal was demodulated and the resulting envelope was studied by methods of the amplitude and time pattern analysis. The other problems were solved by measuring signals in a range of frequencies not exceeding 20 kHz.

The task of counting loading cycles is readily solved by detecting pulses corresponding to the load impacts on the walls; the disappearance of these pulses is evidence of sample fracture. It is very important to thoroughly control the quality of sample fixation in the clamps: The loss of rigidity as a result of stress relaxation makes further testing senseless. This control is provided by detecting characteristic signals generated due to the sample slack in the clamps. Once such a signal is detected, the test is terminated and the accumulated data are analyzed. Parameters of the curve of cyclic loading are determined from data on the decrement of sample oscillations. The decrement was determined by monitoring the decay of oscillations after switching off the electromagnet. At large amplitude of oscillations, the logarithm of the amplitude of natural oscillation is a nonlinear function of the number of half-cycles. The passage to a linear relation reflects the transition to elastic straining and indicates that the yield stress is reached. Using well-known relations [2], the maximum stresses can be calculated from the values of deformation. The sample temperature was determined from the temperature dependence of the elastic modulus. The resonance frequency of the oscillatory system is determined by its most readily deformable part, that is, by the sample cross section in the immobile clamp. This frequency was evaluated by measuring the impedance of the piezoelectric gauge, after which the temperature was determined using the results of preliminary calibration experiments. It was experimentally established that this method allows the sample temperature to be determined with an error not exceeding 2–3 K.

The results of fatigue testing of a Zr–1.2% Sn–1% Nb–0.4% Fe alloy by cyclic loading at a frequency of 0.5 s^{-1} and a temperature of 360°C in the absence and presence of iodine vapor

Iodine vapor density, mg/cm^2	Maximum stress σ_{max}, MPa	Minimum stress σ_{min}, MPa	Number of cycles to acoustic emission onset, N_{AE}	Number of cycles to fracture, N_f
0	280	–100	125300	162180
0.6	280	–100	117800	194980
0	320	–80	142400	173780
0.2	320	–80	85030	95500
0.6	320	–100	41220	53700

Monitoring of the presence of aggressive medium in the test capsule is necessary for eliminating the risk of incorrect results related to the leak of the aggressive agent. The control was provided by heating the vapor generator at a rate of 10–20 K/min, whereby iodine evaporation gives rise to an acoustic noise. When necessary, cyclic loading of a sample was interrupted for a short period of time and the generator noise was detected without the background of the test system noise.

Using the above facilities, we have studied the fatigue life of zirconium alloys for cladding tubes. The samples were irradiated with fast neutrons ($E >$ 0.1 MeV) to a total fluence of 2×10^{26} m^{-2} and tested at a working temperature (360°C). Comparative data on the fatigue life of an irradiated clad alloy with the composition Zr–1.2% Sn–1% Nb–0.4% Fe tested in an inert medium and in iodine vapor are presented in the table. In the case of the aggressive medium, the exposure was restricted to 50 h. Limited volume of the experimental data and relatively short exposure time do not allow us to make reliable conclusions concerning the effect of iodine vapor on the fatigue life of the alloy studied.

It was found that a significant acoustic emission corresponds to a crack jump of 2–4 μm. The results obtained for 66 unirradiated samples showed that the time to the onset of cracking (expressed as the relative number of cycles to fracture) obeys the normal distribution N (0.65; 0.026). The distributions exhibited no significant distinctions upon variation of the asymmetry coefficient and the level of stresses in the loading cycle. Therefore, the appearance of the acoustic emission sig-

nal allows the moment of fracture to be predicted with certain reliability, so that the test can be terminated before fracture. In the case of irradiated samples, the average ratio N_{AE}/N_f increases to 0.77 (see table). This is naturally explained by an increase in the brittleness of the material and a decrease in the relative time to fracture.

The proposed technique can be applied in various fields of industry. It is most effective in the development of new materials for operation under extremal conditions of high temperatures, aggressive media, and ionizing radiation.

REFERENCES

1. V. M. Baranov and V. A. Karasevich, in *Proceedings of the 14th Scientific-Technological Conference on Sensors and Data Converters: Application to Measurement, Monitoring, and Control, Moscow, 2002*, pp. 204–205.
2. *Strength, Stability, Oscillations: A Handbook*, Ed. by I. A. Birger and Ya. G. Panovko (Mashinostroenie, Moscow, 1968) [in Russian], Vol. 1.
3. I. M. Dremin, Usp. Fiz. Nauk **170**, 1235 (2000) [Phys. Usp. **43**, 1137 (2000)].

Translated by P. Pozdeev

Technical Physics Letters, Vol. 30, No. 3, 2004, pp. 183–185. Translated from Pis'ma v Zhurnal Tekhnicheskoĭ Fiziki, Vol. 30, No. 5, 2004, pp. 23–29.

A Model of Nonlinear Ion Drift Spectrometry for Gas Detectors with Separating Chamber of Cylindrical Geometry

A. A. Elistratov* and S. V. Shibkov

Institute for Cryptosystems, Communications, and Informatics, Moscow, Russia

** e-mail: elist@fssr.ru*

Received July 23, 2003

Abstract—A model of nonlinear ion drift spectrometry for modern gas analyzers with separating chamber of cylindrical geometry is developed. In this case, a peak in the ionogram corresponds to the appearance of a limit cycle in the space of trajectories of the dynamical system. The experimentally observed ion beam focusing is theoretically calculated. For the separating voltage described by a piecewise constant function and the nonlinear mobility component described by a simple model, the shape of ionograms is determined and an analytical expression for the compensating voltage as a function of the separating field is obtained. © *2004 MAIK "Nauka/Interperiodica".*

Gas analyzers employing the principle of nonlinear ion drift spectrometry (NIDS) are widely used for detecting traces of explosives, drugs, and poisons in the atmosphere [1–7]. Using a model justified previously [8], we will consider the principle of ion separation in such gas analyzers with a drift chamber of cylindrical geometry.

The typical scheme of a gas analyzer employing the NIDS principle was described in [1–5]. Let us consider a device with the drift chamber representing a cylindrical capacitor of length l with the inner and outer electrode radii r_1 and r_2, respectively. A voltage applied to the electrodes is the sum of a high asymmetric separating voltage $U_S(t)$ with the period T and a small compensating voltage U_C obeying the conditions

$$\int_0^T U_S(t)dt = 0,\ \int_0^T U_S^{2n+1}(t)dt \neq 0\ (n = 1, 2, \ldots),$$

and $U_C \ll U_0 = \max_{0<t<T} U_S(t)$. The sample of air containing impurity ions to be detected is pumped through the gap between electrodes.

For the typical parameters of motion of the impurity ions and the carrier gas used in most modern gas analyzers, the transverse drift of ions is described by the equation

$$\frac{dr}{dt} = k(E)E(r, t), \qquad (1)$$

which essentially coincides in form with the equation of motion for a single ion in a viscous medium. Here, r is the distance of the ion from the chamber axis, $E(r, t)$ is the electric field strength in the gap, and $k(E)$ is the field dependence of ion mobility in the gas. The latter quantity can be expressed as $k(E) = k(0)(1 + \alpha(E))$, where $k(0)$ is the mobility in the zero field limit and $\alpha(E)$ is the nonlinear mobility component. A consistent theoretical justification of this approach with neglect of the diffusion and the space charge of ions was given previously [8]. In further considerations, it will be convenient to pass from the distance r to a dimensionless variable $x = (r/r_2)^2$.

Equation (1) offers the example of a nonautonomous dynamical system. Such systems are usually analyzed in terms of a cylindrical phase manifold in the phase space (Fig. 1b) generated by identifying points in the coordinate space corresponding to the beginning and end of each period [9]. A region on the cylinder surface in which ions move without touching the drift chamber walls (i.e., the ion trajectories $x(t)$ are confined between $x_{1SW}(t)$ and $x_{2SW}(t)$ in Fig. 1a) represents a ring to within a zero-order accuracy with respect to $\alpha(E)$. The exact shape of this region is determined by the form factor of the separating voltage $U_S(t)$. A cross section of this ring corresponding to a given phase (for certainty, $\varphi = 0$) will be referred to below as the survival window. The trajectory of an individual particle on the cylindrical phase manifold appears as an open winding in which the particle displacement over a period, $\Delta x_T(x_0, U_{C0}) = x_T(x_0, U_{C0}) - x_0$, depends on the initial position x_0 in the beginning of the period ($U_{C0} = U_C/U_0$ is the dimensionless compensating voltage). Below, the quantity $\Delta x_T(x_0, U_{C0})$ representing the difference of the trace function (introduced in the theory of dynamical systems [9]) and the initial coordinate will be referred to as the trace function. This function may possess a root x_0^* such that $\Delta x_T(x_0^*, U_{C0}) = 0$, which corresponds to a selection rule in the case of a planar drift chamber [8].

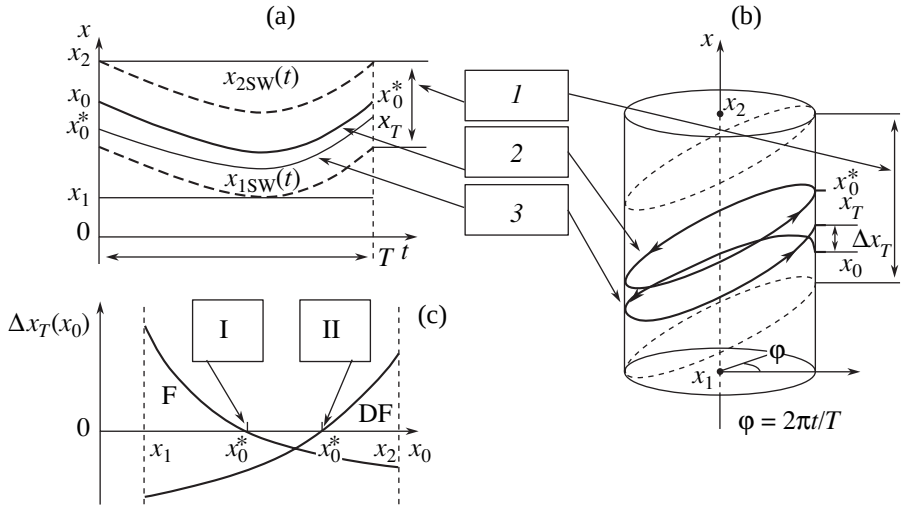

Fig. 1. Schematic diagrams showing (a) ion trajectories in the gap of the drift chamber, (b) cylindrical phase manifold in the phase space, and (c) trace functions corresponding to the regimes of ion focusing (F) and defocusing (DF): (*1*) survival window; (*2*) limit cycle; (*3*) ion trajectory; (I) stable limit cycle; (II) unstable limit cycle.

Let us introduce the parameter

$$\eta = \left.\frac{\partial(\Delta x_T(x_0, U_{C0}))}{\partial x_0}\right|_{x_0 = x_0^*}, \qquad (2)$$

called the focusing intensity. A closed trajectory passing through the point x_0^* is a limit cycle of the dynamical system. This cycle is stable for $\eta < 0$ and unstable for $\eta > 0$. In the case of a stable limit cycle, the particle trajectories wound onto the cylinder gradually converge to the limit cycle, which corresponds to ion focusing. On the contrary, for an unstable limit cycle, the trajectories diverge toward the drift chamber walls. As the number of periods increases, this leads to an increase in the fraction of ions recombining on the walls and, hence, to a decrease in the corresponding peak intensity on the ionogram.

For example, consider an analytical solution obtained by averaging over fast rotations for the simplest field dependence of ion mobility $k(E) = k(0)(1 + \beta(E/E_{max})^2)$, where E_{max} is the scale of the field strength for which the ion mobility is substantially nonlinear, and a piecewise constant voltage $U(\tau) = U_0 g(\tau)$. Here, $g(\tau) = \{(1 + U_{C0}), 0 < \tau < \tau_1; -\tau_1/(1 - \tau_1) + U_{C0}, \tau_1 < \tau < 1\}$, $\tau = t/T$ is the current dimensionless time, τ_1 corresponds to the moment of voltage polarity switching, and $E_0 = U_0/(r_2 \ln(r_2/r_1))$ is the characteristic field strength in the gap. Integrating Eq. (1) to within the terms linear with respect to β, we obtain

$$\Delta x_T(x_0, U_{C0}) = 2cU_{C0} + \beta_1 \theta \ln\left(1 + \frac{2c\tau_1}{x_0}\right), \qquad (3)$$

where $c = k(0)E_0 T/r_2$, $\beta_1 = \beta(E_0/E_{max})^2$, and

$$\theta = (1/\tau_1)\int_0^1 (U_S(t)/U_0)^3 d\tau = (1 - 2\tau_1)/(1 - \tau_1)^2.$$

The equation $\Delta x_T(x_0^*, U_{C0}) = 0$ implicitly determines the position of the limit cycle as dependent on the compensating voltage. Solving Eq. (3) with allowance of the latter condition, we obtain the function

$$x_0^*(U_{C0}) = \frac{2c\tau_1}{\exp\left\{-\dfrac{2cU_{C0}}{\beta_1\theta}\right\} - 1}, \qquad (4)$$

which will be referred to as the limit cycle trajectory in the space of parameters of the dynamical system. Examples of the trajectories of limit cycles for the positive and negative ions with sublinear ($\beta_1 < 0$) and superlinear ($\beta_1 > 0$) characters of the nonlinear mobility are presented in Fig. 2. Note that the negative ions ($c < 0$), for example, with $0 < \tau_1 < 0.5$, exhibit focusing (i.e., possess a stable limit cycle) only in the case of a sublinear ($\beta_1 < 0$) mobility, whereby the peak in the ionogram is observed in the region of positive compensating voltages ($U_{C0} > 0$).

Using Eqs. (2)–(4), we obtain the following expression for the focusing intensity:

$$\eta = -\frac{2\beta_1\theta}{c\tau_1}\sinh^2\left(\frac{cU_{C0}}{\beta_1\theta}\right). \qquad (5)$$

When the compensating voltage U_{C0} varies, the limit cycle "moves" along the trajectory and crosses the survival window, whereby a peak appears on the ionogram (Fig. 2). In the case of a stable limit cycle, the top part of the peak (corresponding to the limit cycle occurring inside the survival window) represents a plateau, because all ions whose trajectories pass through the survival window are focused, irrespective of the limit cycle position (and, hence, of the U_{C0} value) in the

vicinity of this cycle. The values of the compensating voltage bounding the top part of the peak, U_1 and U_2, are determined using relation (4):

$$U_1 = -\frac{\beta_1\theta}{2c}\ln\left(1+\frac{2c\tau_1}{x_1}\right),$$
$$U_2 = \frac{\beta_1\theta}{2c}\ln\left(1-\frac{2c\tau_1}{x_2}\right), \quad (6)$$

where $x_1 = (r_1/r_2)^2$ and $x_2 = 1$.

Expressions describing the peak shape are not presented here since they are very cumbersome. It should only be noted that a decrease in the air flow rate (i.e., an increase in the ion drift time) results in steeper fronts of the ion peak corresponding to a stable limit cycle (at a constant height of the plateau), while the peak corresponding to an unstable limit cycle gradually vanishes.

As can be seen from Eqs. (4) and (5) for $c < 0$, $0 < \tau_1 < 0.5$, and $\beta_1 < 0$, in the limit of $U_{C0} \longrightarrow \infty$, we obtain $x_0^* \longrightarrow -2c\tau_1$ and $\eta < 0$. Therefore, when $-2c\tau_1 \in [x_1, x_2]$, the stable limit cycle will be "suspended" in the survival window. In experiment, this should be manifested by virtually uniform filling of the entire drift spectrum. For $-2c\tau_1 > x_2$, the limit cycle trajectory does not fall within the survival window for any value of U_{C0}. This implies that ions of the given type cannot be detected using the drift chamber with such parameters. The effect of the nonmonotonic character of the nonlinear ion mobility on the behavior of limit cycles will be considered in detail in a special publication.

The dependence of a compensating voltage corresponding to the position of a given ion peak in the ionogram on the maximum separating voltage applied to the drift chamber electrodes is a characteristic that is most frequently measured in experiment [2, 3, 6]. Defining U_C/U_0 as $(U_1 + U_2)/2$ and using relation (6), we obtain the following analytical expression for this dependence:

$$U_C(U_0) = AU_0^2\left\{B + \ln\left(\frac{C+U_0}{D-U_0}\right)\right\}, \quad (7)$$

where $A = -\beta\theta/(2E_{max}^2 k(0)TB)$, $B = 2\ln(r_2/r_1)$, $C = r_1^2 B/(\tau_1 k(0)T)$, and $D = C(r_2/r_1)^2$. In the limit of $U_0 \longrightarrow 0$, relation (7) reveals to within a logarithmic accuracy the trend $U_C(U_0) \sim U_0^2$. This result agrees well with the experimental data reported in [2, 3, 6]. If $r_1, r_2 \longrightarrow \infty$ so that $d = (r_2 - r_1)$ remains finite, relation (7) yields $U_C(U_0) \sim U_0^3$, in agreement with the results of theoretical calculations for the drift chamber with a planar geometry [8].

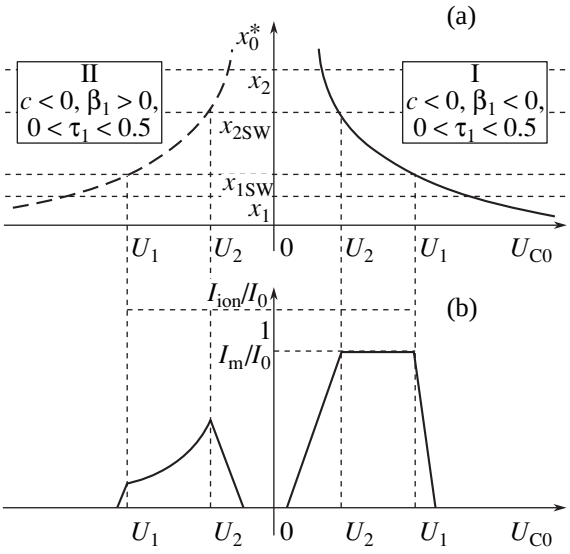

Fig. 2. Schematic diagrams showing (a) the dependence of the position of stable (I) and unstable (II) limit cycles on the compensating voltage U_{C0} and (b) the shapes of the corresponding peaks on the ionogram.

In concluding, it should be noted that the proposed NIDS model can be used as a methodological basis for constructing gas analyzers with cylindrical drift chambers and for the analysis of their operation.

REFERENCES

1. I. A. Buryakov, E. V. Krylov, A. L. Makas', *et al.*, Pis'ma Zh. Tekh. Fiz. **17** (12), 60 (1991) [Sov. Tech. Phys. Lett. **17**, 446 (1991)].
2. I. A. Buryakov, E. V. Krylov, A. L. Makas', *et al.*, Zh. Anal. Khim. **48**, 156 (1993).
3. I. A. Buryakov, Yu. N. Kolomiets, and V. B. Luppu, Zh. Anal. Khim. **56**, 381 (2001).
4. A. V. Kudryavtsev and A. L. Makas, in *Proceedings of the 10th International Conference on Ion Mobility Spectrometry, Wernigrode, 2001*, Vol. 4, pp. 117–120.
5. E. G. Nasarov, R. A. Miller, G. A. Eiceman, *et al.*, in *Proceedings of the 10th International Conference on Ion Mobility Spectrometry, Wernigrode, 2001*, Vol. 4, pp. 43–46.
6. I. A. Buryakov, Zh. Tekh. Fiz. **72** (11), 109 (2002) [Tech. Phys. **47**, 1453 (2002)].
7. O. A. Bannykh, K. B. Povarova, and V. I. Kapustin, Zh. Tekh. Fiz. **72** (12), 88 (2002) [Tech. Phys. **47**, 1570 (2002)].
8. A. A. Elistratov and S. V. Shibkov, Pis'ma Zh. Tekh. Fiz. **29** (2), 88 (2003) [Tech. Phys. Lett. **29**, 81 (2003)].
9. A. A. Andronov, E. A. Leontovich, I. I. Gordon, and A. G. Maier, *Theory of Bifurcations of Dynamical Systems on a Plane* (Nauka, Moscow, 1967; Halsted Press, New York, 1973).

Translated by P. Pozdeev

Technical Physics Letters, Vol. 30, No. 3, 2004, pp. 186–189. Translated from Pis'ma v Zhurnal Tekhnicheskoĭ Fiziki, Vol. 30, No. 5, 2004, pp. 30–39.

Dynamical Control in Multistable Systems

E. N. Egorov* and A. A. Koronovskiĭ

State Scientific Center "College," Saratov State University, Saratov, Russia

** e-mail: Egorov@cas.ssu.runnet.ru*

Received August 5, 2003

Abstract—The possibility of controlling oscillatory regimes in a dynamical system in which multistability is observed for certain values of the control parameters is considered for the Hénon map. It is shown that, in the case of such parametric action suppressing the undesired dynamic regime, the system either passes to a different state or exhibits unlimited growth of the dynamic variable characterizing the state of the system. The new regime is sensitive to small fluctuations of the phase of the parametric action. *© 2004 MAIK "Nauka/Interperiodica".*

Multistability is a phenomenon rather frequently encountered in systems of various types [1–6]. This phenomenon can be observed both in real physical systems, described in terms of ordinary differential equations (e.g., in laser [4] or radio physics [6–8]), and in model systems with discrete time, such as the Hénon map [9]. Multistability accounts for the possible coexistence of various oscillatory regimes in the phase space of the system for the same values of control parameters. For a system exhibiting such behavior, it is frequently very difficult to predict the asymptotic regime which this system will attain at $t \longrightarrow \infty$ for the given initial conditions. In particular, the boundaries of the basin of attraction in the phase space may possess a fractal structure [10–12], making the behavior of the system substantially unpredictable. As a rule, multistability may hinder functioning of the system and, therefore, is not desirable; moreover, this property is sometimes harmful. For this reason, the problem of controlling the dynamic state of such systems is of importance.

Solving the problem of controlling multistability implies the possibility to act upon the system so as to select one of the dynamic regimes and suppress the others. One possible means of controlling the state of a dynamical system is via parametric action [7, 8, 13]. This approach is based on a periodic modulation of some control parameter,

$$p = p_0 + F(t), \tag{1}$$

where p is the selected control parameter and $F(t)$ is a time-dependent periodic function. Mechanisms of this parametric action can be either resonance or nonresonance (see below). Selection of a particular mechanism depends on the system under consideration. Effective control of the oscillatory regimes requires selecting optimum values of the modulation frequency and amplitude.

The parametric method of control is frequently referred to as the "nonfeedback" control, in contrast to the other methods employing feedback for controlling the system dynamics. Advantages of the nonfeedback control are that (i) this approach does not require that the system behavior in the phase space be a priori known in detail and (ii) no feedback chain is required. The latter circumstance is especially important in cases when introduction of the feedback into a given system is difficult or principally impossible.

Investigations devoted to nonfeedback control usually consider the possibility of stabilizing unstable orbits confined within a strange attractor corresponding to a chaotic regime in the phase space [13, 14]. However, the control of multistability implies solving the inverse problem: it is necessary to select a certain regime in the system dynamics and suppress the other, coexisting regimes. In order to solve this task [15, 16], a method employing the same nonfeedback control (or parametric action) was proposed and applied to the Hénon map [17].

As is known, an important role in external action upon a dynamical system is played by the phase relation between oscillations in the system and the driving action [18]. This study was aimed at elucidating the role of the initial phase in the parametric action upon a system with multistability.

Following [15, 16], we select a model system in the form of the Hénon map

$$\begin{aligned} x_{n+1} &= 1 - \mu x_n^2 + y_n, \\ y_{n+1} &= -J x_n. \end{aligned} \tag{2}$$

For the set of control parameters ($\mu = 1.083$, $J = 0.9$), this system exhibits multistability manifested by three limiting cycles corresponding to period 1, period 3, and period 9 coexisting in the phase space. This behavior is retained in a very narrow interval of $1.077 < \mu < 1.089$,

1063-7850/04/3003-0186$26.00 © 2004 MAIK "Nauka/Interperiodica"

outside which there are two coexisting regimes, corresponding to period 3 and period 1. The basins of attraction of the corresponding attractors in the phase space exhibit a complicated fractal structure (Fig. 1a).

The parametric action upon the system under consideration is applied as follows. For the values of parameters corresponding to the coexistence of several oscillatory regimes, we select a transient process sufficient for the system to attain a certain cycle. At a discrete time n_0, a parametric action is switched on in the form of an oscillating additive to the control parameter μ. The coordinates of the imaging point in the phase space and the parameter J remain unchanged. Following [16], the parameter μ was modulated by a periodic signal,

$$\mu = \mu_0 + \mu_c \sin(2\pi f_c n + \psi_0), \qquad (3)$$

where μ_0 is the initial constant value of the control parameter about which the small periodic oscillations are performed with the amplitude μ_c and the frequency f_c. A distinctive feature of our method consists in that the parametric modulation is introduced with a certain initial phase ψ_0, while other researchers usually ignore the phase dependence of the oscillatory regime and consider the case of zero initial phase.

For this parametric action to influence the stability of the attracting point (cycle), it is necessary that this point (cycle) be characterized by complex-conjugate multiplicators. The natural (relaxation) frequency f_r, as well as the frequency of an oscillator with damping, can be determined numerically after driving the system out of equilibrium [16]. Thus, by selecting f_c close to f_r and varying the amplitude μ_c of the parametric action, it is possible to provide that the (previously) stable state will lose stability and the system will pass to a different dynamic regime [16]. The amplitude of the parametric action is such that variation of the parameter μ by the increment μ_c in the absence of the harmonic additive does not lead to qualitative changes in the system behavior. In this case, the parametric action is of a resonance type. In the case of a nonresonance action, the frequency f_c does not necessarily coincide with f_r. This method is also called low-frequency parametric action, meaning that $f_c \ll f_r$. However, in such cases, the amplitude of the parametric action must be sufficient to provide that the system even without resonance interaction can cross the boundary of the basin of attraction of the suppressed regime [14].

A change in the dynamics of the system under parametric action is most conveniently traced by studying the structure of the basins of attraction in the phase space. Figures 1b and 1c show the basins of attraction for the attractors realized in the phase space of system (2) for various phases of the parametric action with $f_c = 0.11$,

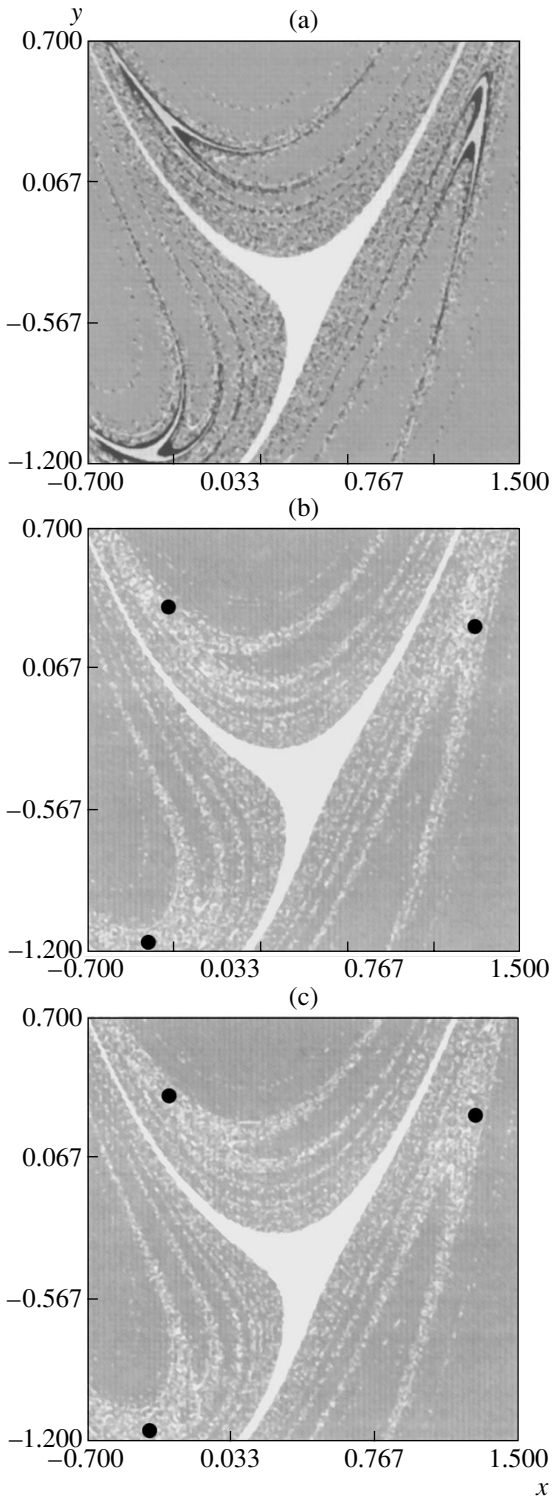

Fig. 1. Schematic diagrams showing the structure of the basins of attraction in the phase space of the Hénon map for the control parameters (μ =1.083, J = 0.9): (a) in the absence of a parametric action; color gradations indicate the basins of attraction of the cycles of period 1 (white), period 3 (light-gray), period 9 (black), and the region of expansion of the phase trajectories (dark-gray); (b, c) in the presence of a parametric action with the parameters μ_c = 0.05, f_c = 0.11 and the initial phase ψ_0 = 0.31 (b) and 1.51 (c), black circles indicate the points of period 3.

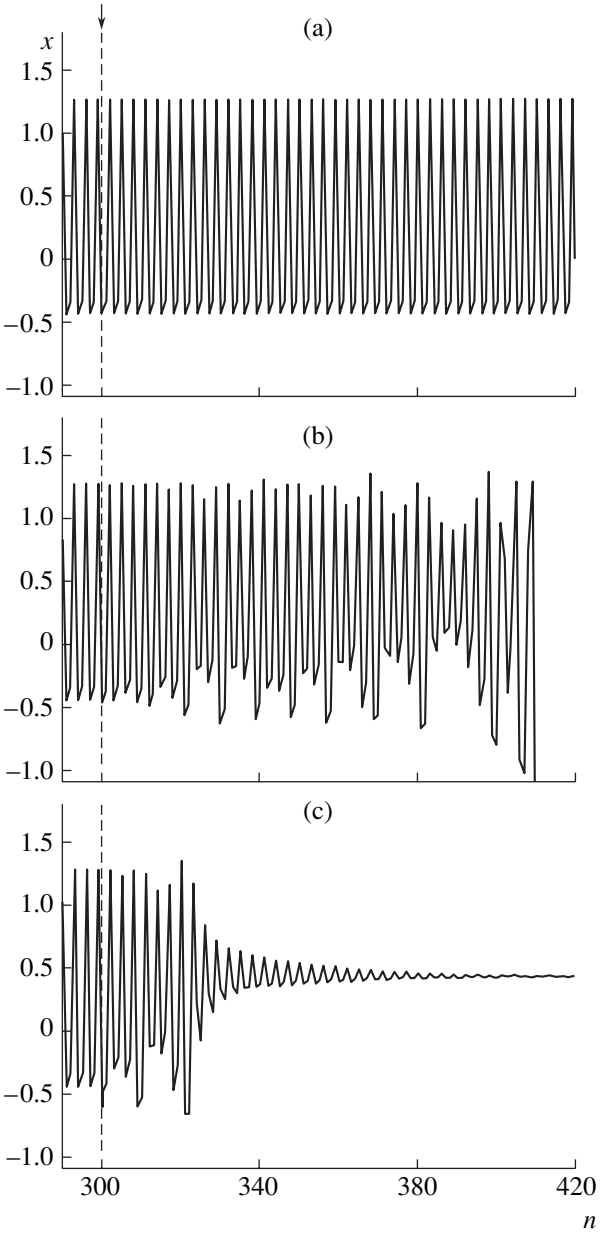

Fig. 2. Fragments of time series for the Hénon maps (a) in the absence of a parametric action and (b, c) in the presence of a parametric action with the initial phase $\psi_0 = 0.31$ (b) and 1.51 (c); the arrow and the dashed line indicate the moments of discrete time n_0 corresponding to the onset of the parametric action.

$\mu_c = 0.05$. As can be seen, the parametric action results in destruction of the basins of attraction of the cycles of period 3 and period 9.

It should be noted that the amplitude of the parametric action selected in this study is significantly greater than the value of parameter μ necessary for suppressing the cycle of period 9 [16]. Thus, the system with the parameters $\mu_1 = \mu_0 + \mu_c$ and $\mu_2 = \mu_0 - \mu_c$ no longer exhibits the oscillatory regime of period 9, while the cycle of period 3 is retained. Under this action, the system occurs in a stationary state.[1] The regions of the phase portrait previously occupied by the basins of attraction of the cycles of period 3 and period 9 are now (Figs. 1b and 1c) occupied by the basins of attraction of the cycle of period 1 and the attractor occurring at infinity. At the same time, no significant differences in the structure of the basins of attraction is observed for various values of the initial phase of the parametric action.

It should be noted that the basins of attraction of both attractors at the points previously occupied by the elements of the cycle of period 3 appear as "riddled." In other words, small perturbations (which can be represented either by noise or by variations of the initial phase ψ_0 of the parametric action) play a key role, determining which of the remaining attractors will attract the imaging point. This is illustrated by Fig. 2a, showing a time series corresponding to the behavior of the system realizing the cycle of period 3 in the absence of a parametric action, in comparison to Figs. 2b and 2c, which show the behavior of the system starting from the same initial conditions but in the presence of the parametric action switched at the moment indicated by the arrow. As can be clearly seen, the parametric action switched in the same phase of oscillations of the system, but with different initial phases, may lead to opposite results. After switching of the parametric action leading to the destruction of the cycle of period 3, the dynamic variable can either reach a stationary level (Fig. 2c) or exhibit infinite growth (Fig. 2b). In attempts to use the parametric action for controlling the behavior of a real physical (biological, chemical, etc.) system, such phenomena may lead to destruction of the system and, hence, are not desirable.

Thus, we have considered a method of parametric action for controlling oscillatory regimes of a system with multistability. The problem was studied in application to a system with discrete time representing the Hénon map. Investigation of the parametric action upon this model system showed that the regime established as a result of such control action may significantly depend on small variations in phase of the parametric action and/or the noise.

Acknowledgments. This study was supported by the Russian Foundation for Basic Research (project no. 02-02-16351), the Program "Universities of Russia. Basic Research" (project UR.01.01.065), and the Scientific-Education Center "Nonlinear Dynamics and Biophysics" at Saratov State University (Grant REC-006 from the US Civilian Research and Development Foundation for the Independent States of the Former Soviet Union).

[1] Note also that the resulting oscillations are modulated at a frequency corresponding to that of the parametric action, but the depth of this modulation is much smaller than the signal amplitude. Such small oscillation (on the order of 10^{-3}) can be ignored on the background of the main signal (on the order of unity).

REFERENCES

1. F. T. Arecchi, R. Meucci, G. Puccioni, and J. Tredicce, Phys. Rev. Lett. **49**, 1217 (1982).
2. C. Grebogi, E. Ott, and J. A. Yorke, Phys. Rev. Lett. **50**, 935 (1983).
3. C. Grebogi, E. Kostelich, E. Ott, and J. A. Yorke, Physica D **25**, 347 (1987).
4. F. T. Arecchi, G. Puccioni, A. Poggi, *et al.*, Phys. Rev. Lett. **55**, 339 (1985).
5. A. V. Andrushkevich, A. A. Kipchatov, L. V. Krasichkov, and A. A. Koronovskiĭ, Izv. Vyssh. Uchebn. Zaved., Radiofiz. **38**, 1195 (1995).
6. E. N. Egorov and A. A. Koronovskiĭ, Izv. Vyssh. Uchebn. Zaved., Prikl. Nelineĭnaya Din. **10** (1–2), 104 (2002).
7. M. I. Rabinovich and D. I. Trubetskov, *Introduction to the Theory of Oscillations and Waves* (Nauka, Moscow, 1984; Kluwer, Dordrecht, 1989).
8. V. S. Anishchenko, T. E. Vadivasova, and V. V. Astakhov, *Nonlinear Dynamics of Chaotic and Stochastic Systems* (Saratovsk. Gos. Univ., Saratov, 1999) [in Russian].
9. J. Curry, Commun. Math. Phys. **68**, 129 (1979).
10. E. Eschenazi, H. G. Solari, and R. Gilmore, Phys. Rev. A **39**, 2609 (1989).
11. U. Feudel, A. Witt, Y.-C. Lai, and C. Grebogi, Phys. Rev. E **58**, 3060 (1998).
12. M. Schmick, E. Goles, and M. Markus, Phys. Rev. E **62**, 397 (2000).
13. R. Lima and M. Pettini, Phys. Rev. A **41**, 726 (1990).
14. A. N. Pisarchik, V. N. Chizevsky, R. Corbalan, and R. Vilaseca, Phys. Rev. E **55**, 2455 (1997).
15. A. N. Pisarchik and B. K. Goswami, Phys. Rev. Lett. **84**, 1423 (2000).
16. A. N. Pisarchik, Phys. Rev. E **64**, 46203 (2001).
17. M. Henon, Commun. Math. Phys. **50**, 69 (1976).
18. A. A. Koronovskiĭ, D. I. Trubetskov, and A. E. Khramov, Dokl. Ross. Akad. Nauk **389**, 749 (2003) [Dokl. Phys. **48**, 166 (2003)].

Translated by P. Pozdeev

Technical Physics Letters, Vol. 30, No. 3, 2004, pp. 190–192. Translated from Pis'ma v Zhurnal Tekhnicheskoĭ Fiziki, Vol. 30, No. 5, 2004, pp. 40–45.

The Fracture of Microscopic Metal Samples in a Strong Electrostatic Field

S. V. Zaĭtsev

Institute of Theoretical and Experimental Physics, Federal Unitary Enterprise, Moscow, Russia

e-mail: zai336@mail.ru

Received July 29, 2003

Abstract—The level of mechanical stresses arising in a conductor under the action of a strong electric field is evaluated. It is shown that the mutual repulsion of surface charges has to be taken into account for correct determination of the critical cross section. © *2004 MAIK "Nauka/Interperiodica".*

Conductors occurring under the action of a strong electric field are subject to development of the field-induced mechanical stresses. The level of these stresses may reach the ultimate strength, leading to mechanical fracture and undesired electric discharges (breakdown) [1]. Therefore, it is important to estimate the magnitude of possible critical stresses.

It is a usual practice to estimate the field-induced mechanical stresses in a conductor using an expression for the so-called "negative electrostatic pressure" $\sigma = \varepsilon_0 E^2/2$, where E is the electric field strength at a given point of the conductor surface, ε is the permittivity, and σ is the pressure [2]. There were numerous experiments with an electric field applied to microscopic samples for evaluating the magnitude of breaking stresses [3–7]. In these experiments, the samples were in the form of microscopic points placed in vacuum at a distance of several centimeters from a plane screen and oriented perpendicularly to this screen. Then, a positive electric potential was applied to the sample and increased to a level at which the material was broken by "ponderomotive" forces. The level of mechanical stresses in a given cross section of the sample was determined by summing forces calculated using the above formula as described in [8]. The results obtained for the samples with diameters within 50–100 nm qualitatively agree with the existing notions about the strength of metals [9].

However, there is certain doubt concerning the validity of the approach described above. The author carried out a series of experiments on the fracture of metal points in an electrostatic field. The samples with a diameter of 50–100 nm at the point tip were made of tungsten, molybdenum, and stainless steel as described in [10]. During the experiments, the samples were exposed to an electric field linearly increasing at various rates within 10^2–10^4 V/s and a temperature in the interval from 78 to 300 K. Prior to this, all samples were treated at an applied voltage of 5 kV until complete termination of the field evaporation processes, which ensured that the samples had the same initial radius of the point tip. In order to avoid electric discharge at the moment of sample fracture, the sample was connected to the electric circuit in series with a resistance of 10^{11} Ω. The moment of sample fracture was detected by a characteristic change in the image.

The results of these experiments generally agree with the data reported in the aforementioned papers, provided that the final sample diameter is taken equal to that of the point tip immediately before fracture of the sample. However, examination of the broken samples in a scanning electron microscope showed that the fracture takes place in most cases far from the point tip, involving that part of a sample where the level of mechanical stresses calculated using the traditional approach is three to five orders of magnitude lower than the experimentally determined material strength in the corresponding cross section. For a given cross section, the strength was determined by fracture of the sample during electropolishing of the central part of a microwire with an attached load. Figure 1 shows a plot of the breaking voltage U versus final sample diameter at the point tip.

An assumption that the strength may sharply drop under the action of the applied electric field can hardly be accepted because (i) the effect is very large and (ii) it

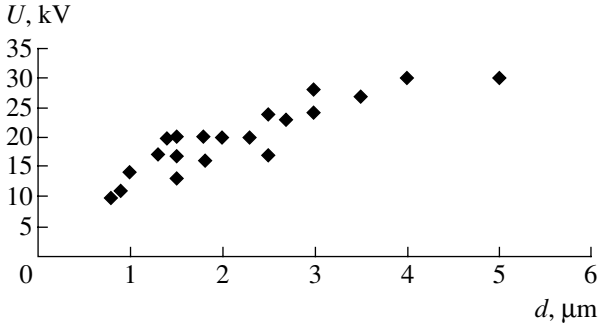

Fig. 1. A plot of the breaking voltage U versus final sample diameter d at the point tip.

would be difficult to explain why the fracture does not take place at the point tip, where the electric field strength is much higher, and is so dramatically manifested at a distance of several microns from the tip. This discrepancy led the author to the conclusion that correct estimates of the level of mechanical stresses at a certain distance from the point can be obtained only taking into account the mutual repulsion of electric charges accumulated at the sample surface.

In order to verify this hypothesis, let us obtain a simple estimate using a model depicted in Fig. 2. A cross section in which the tensile stress has to be determined occurs at a distance A from the point tip, the total point length being $A + B$. The X and Y axes point to the opposite directions from this cross section. To the first approximation, the charge density χ on the surface of the microscopic point can be estimated using the formula for a cylindrical capacitor,

$$\chi = \varepsilon_0 U/R\ln(b/R),$$

where $b \approx 3$ cm is the distance to an external electrode, R is the current radius, and U is the voltage. The charge density at the rounded tip can be evaluated using the formula $\chi = \varepsilon_0 U/(kR_0)$, where k is a coefficient varying between 5 and 10. This approximation for the electric field distribution differs only slightly from that obtained in cases when the point tip is modeled by as a paraboloid or hyperboloid [8].

The total force F in a given cross section can be determined by summing the mutual repulsion forces between all charges $\chi_1 R_1 d\varphi_1 dx$ and $\chi_2 R_2 d\varphi_2 dy$ situated on different sides from the section:

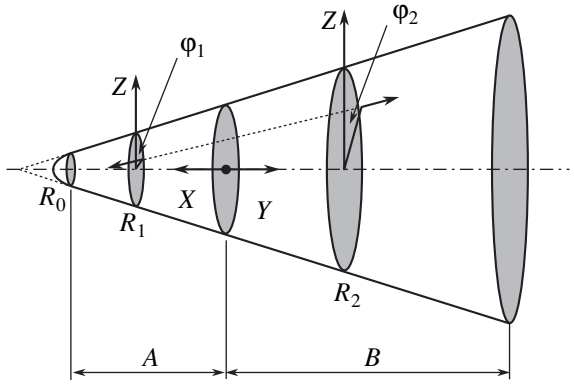

Fig. 2. The model of a microscopic point used for the calculation of mechanical stresses in a given cross section (see the text for explanation).

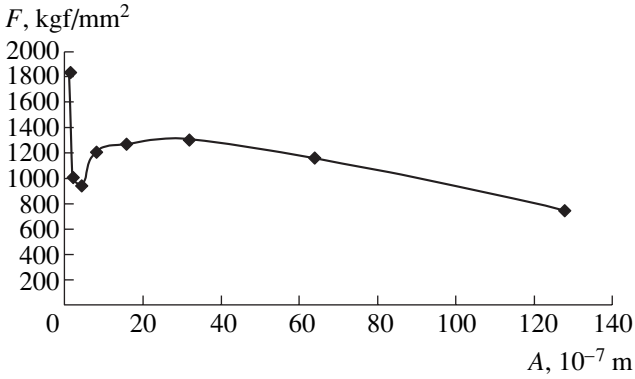

Fig. 3. The profile of tensile stresses in a microscopic point (A is the distance from the point tip).

$$F = \frac{1}{4\pi\varepsilon_0} \times \int_{x=\lambda}^{A}\int_{y=\lambda}^{B}\int_{\varphi_1=0}^{2\pi}\int_{\varphi_2=0}^{2\pi} \frac{\chi_1\chi_2 R_1 R_2 (x+y)\,d\varphi_1 d\varphi_2 dx dy}{\{(x+y)^2 + (R_1\cos(\varphi_1) - R_2\cos(\varphi_2))^2 + (R_1\sin(\varphi_1) - R_2\sin(\varphi_2))^2\}^{3/2}},$$

where $R_1 = R_0 + (A - x)\tan\alpha$, $R_2 = R_0 + (A + y)\tan\alpha$, α is the cone half-angle, and φ_1 and φ_2 are the angles measured from the Z axis in the planes perpendicular to the X axis. In the case under consideration, the integration limit λ cannot be zero (otherwise, the integral would diverge). It can be assumed that λ is of the same order of magnitude as the distance between ion islands protruding from the surface.

The results of numerical calculations performed by the Monte Carlo method using the latter formula agree with the experimental values and weakly depend on λ (Fig. 3). As can be seen from Fig. 3, there is a local maximum of mechanical stresses at a certain distance from the point tip. Taking into account that the material strength sharply (more than tenfold) increases with decreasing diameter below one micron, we can explain why the microscopic points exhibit fracture far from the tip. In the region of local maximum, the field-induced mechanical stresses reach the level of ultimate strength for the corresponding diameter. The field strength can be even higher (e.g., by a factor of five) near the point tip, but the material strength at the sharp tip increases to an even greater extent (e.g., by a factor of six), which hinders material fracture in this region.

Based on the obtained results, we may conclude that mechanical stresses arising in a charged body should be calculated by summing the forces of interaction between all electric charges (this is valid not only for conductors). Additional evidence in favor of this con-

clusion is provided by the following mental experiment. Let a wire be the electrode of a long (probably, toroidal) cylindrical capacitor. Then, calculations using the formula $\sigma = \varepsilon_0 E^2/2$ yields a zero axial mechanical stress, which is obviously incorrect. Apparently, this formula is expediently used for calculating the total force acting upon an object but not for determining stresses inside the object.

Of course the above conclusion has to be further verified. However, should it be valid, the factor under consideration has to be taken into account in designing structures (especially in nanotechnology) operating in strong electric fields. It will also provide for better understanding microscopic mechanisms of electric discharge involving particle detachment from the electrode surface.

REFERENCES

1. I. N. Slivkov, *High-Voltage Processes in Vacuum* (Énergoatomizdat, Moscow, 1986) [in Russian].
2. L. D. Landau and E. M. Lifshitz, *Course of Theoretical Physics*, Vol. 8: *Electrodynamics of Continuous Media* (Nauka, Moscow, 1982; Pergamon, New York, 1984).
3. R. I. Garber, Zh. I. Dranova, and I. M. Mikhaĭlovskiĭ, Dokl. Akad. Nauk SSSR **174**, 1044 (1967) [Sov. Phys. Dokl. **12**, 946 (1967)].
4. A. L. Suvorov and G. M. Kukavadze, Fiz. Met. Metalloved. **28**, 238 (1969).
5. R. I. Garber, Zh. I. Dranova, and I. M. Mikhaĭlovskiĭ, Fiz. Met. Metalloved. **30**, 445 (1970).
6. I. M. Mikhaĭlovskiĭ, P. Ya. Poltinin, and L. I. Fedorova, Fiz. Tverd. Tela (Leningrad) **23**, 1291 (1981) [Sov. Phys. Solid State **23**, 757 (1981)].
7. S. V. Zaĭtsev and A. L. Suvorov, Preprint No. 154 ITEF (Institute of Theoretical and Experimental Physics, Moscow, 1987).
8. H. C. Eaton and R. J. Bayusick, Surf. Sci. **70**, 408 (1978).
9. S. N. Zhurkov, Fiz. Tverd. Tela (Leningrad) **22**, 3344 (1980) [Sov. Phys. Solid State **22**, 1958 (1980)].
10. S. V. Zaitsev and A. V. Karpov, Prib. Tekh. Éksp., No. 4, 144 (2000).

Translated by P. Pozdeev

Technical Physics Letters, Vol. 30, No. 3, 2004, pp. 193–196. Translated from Pis'ma v Zhurnal Tekhnicheskoĭ Fiziki, Vol. 30, No. 5, 2004, pp. 46–53.

The Competition between Aluminum and Group IV (Si, C) Atoms on the Rhenium Surface

N. R. Gall*, E. V. Rut'kov, and A. Ya. Tontegode

Ioffe Physicotechnical Institute, Russian Academy of Sciences, St. Petersburg, 194021 Russia

** e-mail: gall@ms.ioffe.rssi.ru*

Received August 1, 2003

Abstract—Electropositive atoms of aluminum adsorbed on a $(10\bar{1}0)$Re surface exhibit competition with nonmetals (Si, C) for the adsorption sites at high temperatures (1200–1500 K). In this system, silicon displaces aluminum, while aluminum displaces carbon. The mechanism of this competition is fully analogous to that observed previously for Si, C, and S atoms on the surface of refractory metals, despite the fact that aluminum atoms (in contrast to the nonmetals) in the adsorbed state possess a positive charge. © *2004 MAIK "Nauka/Interperiodica".*

As is known, nonmetal atoms of groups IV, V, and VI during joint high-temperature adsorption on a refractory metal surface exhibit competition for the adsorption sites. This competition accounts for a number of phenomena such as the displacement of one adsorbate by another from the surface to the bulk of a substrate with the formation of a solid solution [1–4], joint desorption of two adsorbates [5, 6], and some others [4, 7]. Aluminum atoms possess a low ionization potential and, in contrast to the aforementioned nonmetals, apparently bear a positive charge in the adsorbed state on refractory metals [8]. On the other hand, the properties of the bulk aluminides of tungsten, rhenium, molybdenum, and iridium have much in common with the properties of oxides, carbides, and especially silicides [9]. It is a priori unclear how Al atoms will behave in the course of their joint adsorption with nonmetals at high temperatures making the mobility of adatoms sufficient both for entering into chemical reactions and for penetrating into the bulk of a substrate.

Previous investigations of the deposition of aluminum onto rhenium at high temperatures [8, 10] showed that aluminum atoms at 1250–1300 K occur in a thermally stable adsorption state with a nearly monolayer density. We call this state surface aluminide. All aluminum atoms deposited at $T > 1250$ K onto a surface aluminide layer are dissolved in the bulk of rhenium. The concentration of adatoms in the surface aluminide layer estimated using quantitative Auger electron spectroscopy (AES) amounts to $N_{Al} = (1.6 \pm 0.15) \times 10^{15}$ cm^{-2}. The relative composition of this layer determined with respect to metal atoms of the uppermost layer of the substrate is ReAl. Surface aluminide decomposes only during thermal desorption at $T > 1450$ K.

The deposition of silicon atoms onto rhenium at high temperatures (1300–1400 K) leads to the formation of surface silicide with a relative composition of ReSi and the surface atomic density of $N_{Si} = 1.6 \times 10^{15}$ cm^{-2}. This adlayer forms via the same mechanism as that mentioned above for surface aluminide: unless the surface compound is formed, all deposited Si atoms are retained on the surface of rhenium, while all atoms adsorbed after that are dissolved in the bulk of substrate [11].

Rhenium does not form bulk carbides, and the surface compounds with adsorbed carbon are formed via a more complicated mechanism: their composition depends on the amount of carbon dissolved in the bulk of substrate [12] and varies from $Re_{10}C$ in the initial stage to ReC for an adsorbate dose close to the solubility limit. Surface carbide with the composition Re_4C used in our experiments was obtained by depositing 4–5 monolayers of carbon onto the surface of a rhenium ribbon, followed by dissolution of this adlayer in the bulk of substrate. The resulting density of carbon atoms in this surface carbide, $N_C = 4 \times 10^{14}$ cm^{-2}, is self-maintained by segregation and remains constant within a rather broad range of adsorbed carbon doses (from 4–5 to 200 monolayers) dissolved in the bulk. In the absence of other adsorbates, this carbide is thermally stable at temperatures up to $T = 2000$ K and exhibits reversible dissolution in the bulk at higher temperatures, emerging on the surface again upon cooling.

It should be noted that all three adsorbates form high-temperature surface compounds with the same (ReSi and ReAl) or proportional (Re_4C) content of adsorbed atoms. During the coadsorption of Si and C at 1300–1400 K, carbon is displaced by silicon from the surface into bulk and passes into a dissolved state [2, 4].

The experiments were performed under ultrahigh vacuum (UHV) conditions ($p \sim 1 \times 10^{-10}$ Torr) in a high-resolution ($\Delta E/E < 0.1\%$) Auger electron spectrometer with a prism electron energy analyzer

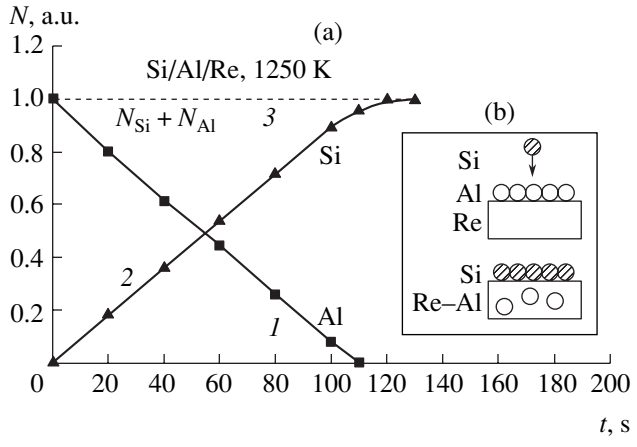

Fig. 1. Deposition of Si atoms onto surface aluminide ReAl on a rhenium substrate at 1250 K: (a) variation of the relative surface densities of (*1*) aluminum, (*2*) silicon, and (*3*) their sum (normalized to the atomic densities of adsorbates in the corresponding surface compounds on rhenium); (b) schematic diagram of events.

described elsewhere [12]. The instrumental facilities allowed the Auger electron spectra to be measured *in situ* on a sample heated to any temperature in the range from 300 to 2200 K. The samples were thin rhenium ribbons with dimensions of $0.02 \times 1 \times 40$ mm, which were thoroughly cleaned from possible impurities by high-temperature annealing for several hours, first in an oxygen atmosphere and then under UHV conditions. The ribbon surface texture for more than 99.5% represented a $(10\bar{1}0)$ rhenium crystal face. The sample surface was homogeneous with respect to the electron work function ($e\varphi = 5.15$ eV). Carbon, silicon, and aluminum were deposited onto the substrate surface from specially designed sources, with the absolute atomic flux densities determined using the methods described previously [10–12].

Let us first consider the joint adsorption of aluminum and silicon on the surface of rhenium. Figure 1a shows the pattern of variation of the Auger signals from both adsorbates in the course of silicon deposition onto surface aluminide at 1250 K. Since both adsorbates occur in the form of surface compounds, the signal intensity is directly proportional to the surface concentration of the corresponding element. As can be seen, every sequential dose of adsorbed silicon leads to a decrease in intensity of the response signal from aluminum. When silicon is deposited in an amount corresponding to surface silicide, the Auger signal from aluminum fully vanishes. This cannot be explained by the screening effect: the same dose of silicon deposited onto the surface aluminide layer at room temperature attenuates the Auger signal from aluminum only by a factor of ~1.5. Therefore, the only possible explanation consists in that silicon atoms deposited at 1300 K displace aluminum from the surface of rhenium (Fig. 1b) by analogy with the displacement of carbon observed previously [3]. It should also be noted that the curves of silicon deposition onto clean rhenium surface and onto that with aluminum adlayer agree with very high accuracy, which implies that silicon atoms behave as if there were no adsorbed aluminum.

It was found that the total surface atomic density of both adsorbates remains virtually constant, so that the amount of displaced aluminum is exactly that required for liberating the necessary adsorption sites for the supplied silicon atoms (Fig. 1a, dashed line *3*).

The reverse order of adsorption, whereby aluminum is deposited onto rhenium covered with surface silicide, does not lead to the accumulation of aluminum even in small amounts on the metal substrate. Note that, in the absence of silicon, all Al atoms striking the substrate are retained in the adlayer until reaching a coverage corresponding to the formation of surface aluminide.

It was interesting to study an intermediate state formed when aluminum was deposited at 1300 K onto a substrate covered with silicon at a concentration corresponding to half of that in surface silicide. In this case, aluminum accumulates on the substrate surface in the initial deposition stage but to a limiting surface density amounting precisely to half of that in surface aluminide. When the total adsorbate density reaches $N_y = (1.6 \pm 0.15) \times 10^{15}$ cm^{-2}, all subsequently deposited aluminum atoms dissolve in the bulk of substrate. Special experiments showed that aluminum and silicon present on the surface of rhenium in a total concentration of $(1.6 \pm 0.15) \times 10^{15}$ cm^{-2} may coexist for many hours (and, probably, longer) at 1300–1400 K, not showing evidence of displacing each other.

The experiments described above do not allow us to make a definite conclusion about the way in which aluminum atoms are displaced by silicon, distinguishing between desorption and dissolution in the bulk of rhenium. Both these outcomes are possible, but dissolution seems to be preferred because thermal desorption of aluminum from a clean rhenium surface takes place at much higher temperatures [8].

Now, let us proceed to the joint adsorption of aluminum and carbon on rhenium. When Al atoms were deposited onto a substrate covered with a layer of surface carbide Re_4C at 1200 K (Fig. 2), the Auger signal from aluminum gradually increased until the formation of surface aluminide. This process was developed in the same way as in the absence of carbon (Fig. 2a, curve *1*). The adsorption of aluminum was accompanied by a decrease in intensity of the Auger signal from carbon, but not to zero: by the time of surface aluminide formation, the response of carbon decreased by 80% (Fig. 2a, curve *2*). Such a decrease in the Auger signal intensity cannot be explained by the screening action of the aluminum adlayer: a monolayer of Al atoms deposited at 300 K attenuated the response of carbon by only ~20%.

Apparently, this system also features the displacement of one adsorbate (C) by another (Al). The probable scheme of events is depicted in Figs. 2b and 2c. The

thermal desorption of aluminum at 1500 K resulted in restoration of the initial amount of carbon (Fig. 2d). Multiply repeated, this experiment did not show any evidence of carbon exhaustion in a source supplying it to the surface. This implies that carbon atoms displaced from the surface are dissolved in the bulk of rhenium rather than desorbed into vacuum. Indeed, if the removed carbon atoms were desorbed, their surface concentration could be restored only at the expense of carbon preliminarily dissolved in the bulk of substrate and several displacement–annealing cycles would exhaust this source and make complete restoration of the carbon coverage impossible. Moreover, the thermal desorption of carbon from clean rhenium takes pace only at $T > 2200$ K [12].

It is interesting to note that, despite the difference in the content of carbon in surface carbide and aluminum in surface aluminide, their mutual exchange is congruent: desorption of ~50% of Al atoms restores surface carbide also approximately by 50%, which implies that no competition between atoms (as in the Al–Si/Re system) takes place. If the deposition of aluminum is suspended at any intermediate point in Fig. 2a, the adsorbed carbon and aluminum coexist on the substrate surface for hours without changes in their surface densities. For surface carbide ReC (instead of Re_4C) with the surface density of carbon $N_C \sim 1.6 \times 10^{14}$ cm^{-2}, the displacement proceeds via the same mechanism, whereby the amount of carbon on the surface decreases with every new dose of adsorbed aluminum and the formation of surface aluminide drives virtually all carbon atoms to dissolve in the bulk of substrate.

For the reverse order of adsorption, whereby carbon is deposited onto rhenium with surface aluminide at 1200–1400 K, all carbon supplied to the sample surface was dissolved in the bulk of rhenium. Deposited in the absence of adsorbed aluminum, carbon immediately forms surface carbide Re_4C.

Let us summarize the obtained results. Previously [1–6], we have observed competition between nonmetal atoms such as Si, C, S, and P. These elements exhibit substantially different properties and the competition for adsorption sites was not evident a priori. However, one important property in common for all these elements is that their atoms adsorbed on refractory metals probably acquire a negative charge, as evidenced by an increase in the electron work function of rhenium (and the other studied substrates). The competition between such atoms can be adequately described using the well-known McLean–Guttmann theory [13]. At the same time, aluminum atoms adsorbed on rhenium apparently bears a positive charge. This follows both from a comparison of the electronegativities of the adsorbate (1.61) and the substrate (~2.2) [14] and from a decrease in the electron work function of rhenium [8, 15] upon aluminum adsorption.

According to the McLean–Guttmann theory, we might expect that the joint adsorption will lead to association or even stimulated segregation on the substrate surface rather than to the displacement of one adsorbate by another. However, such expectations were not confirmed in experiment. In our opinion, the obtained results indicate that the adsorbate charging does not play as significant a role in determining the surface processes as was stipulated by the aforementioned theory [13]. A more important factor is the limited adsorption capacity of a substrate surface, the active centers of which can be occupied by any adsorbate accumulated in excess in a huge reservoir offered by the bulk of substrate, where the impurity atoms may occur in the form of solid solutions. Apparently, the competition for adsorption sites is observed for atoms of the elements capable of forming surface compounds with the substrate. For example, Cs atoms do not form surface compounds and do not displace carbon when cesium is deposited onto a metal substrate covered with surface carbide.

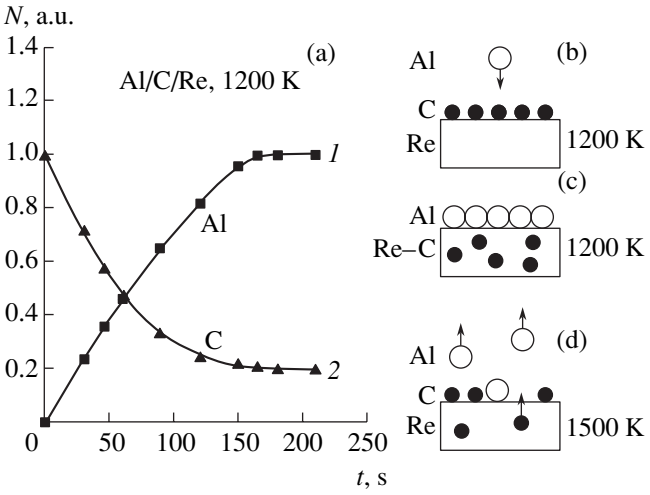

Fig. 2. The interaction of deposited Al atoms with surface carbide Re_4C: (a) variation of the relative surface densities of (*1*) aluminum and (*2*) carbon during deposition of Al onto Re_4C at 1200 K (normalized to the atomic densities of adsorbates in the corresponding surface compounds on rhenium); (b, c) schematic diagram of sequential events during adsorption; (d) desorption of Al atoms and recovery of surface carbide at 1500 K.

In conclusion, aluminum atoms adsorbed on rhenium exhibit active competition with adsorbed nonmetals for the high-temperature (1200–1400 K) adsorption sites. In this case, silicon displaces aluminum, while aluminum displaces carbon. The mechanism of this competition is fully analogous to that observed previously for Si, C, and S atoms on the surface of many refractory metals, despite the fact that aluminum atoms (in contrast to the nonmetals) in the adsorbed state possess a positive charge. It is concluded that the ability to compete for the adsorption sites on metal substrates is determined primarily by the ability of elements to form surface compounds with these metals.

Acknowledgments. This study was performed within the framework of the Program "Surface Atomic

Structures" (project no. 4G157) supported by the Ministry of Science and Technology of the Russian Federation.

REFERENCES

1. V. N. Ageev, E. Yu. Afanas'eva, N. R. Gall', *et al.*, Pis'ma Zh. Tekh. Fiz. **12**, 565 (1986) [Sov. Tech. Phys. Lett. **12**, 231 (1986)].
2. N. R. Gall, E. V. Rut'kov, A. Ya. Tontegode, and M. M. Usufov, Phys. Low-Dimens. Semicond. Struct. **9**, 79 (1994).
3. N. R. Gall', E. V. Rut'kov, and A. Ya. Tontegode, Pis'ma Zh. Tekh. Fiz. **26** (12), 31 (2000) [Tech. Phys. Lett. **26**, 510 (2000)].
4. N. R. Gall, E. V. Rut'kov, and A. Ya. Tontegode, Thin Solid Films **226**, 229 (1995).
5. N. R. Gall', E. V. Rut'kov, A. Ya. Tontegode, and M. M. Usufov, Fiz. Tverd. Tela (St. Petersburg) **38**, 2541 (1996) [Phys. Solid State **38**, 1394 (1996)].
6. N. R. Gall', E. V. Rut'kov, A. Ya. Tontegode, and M. M. Usufov, Pis'ma Zh. Tekh. Fiz. **20** (18), 65 (1994) [Tech. Phys. Lett. **20**, 752 (1994)].
7. N. R. Gall', E. V. Rut'kov, and A. Ya. Tontegode, Pis'ma Zh. Tekh. Fiz. **15** (7), 52 (1989) [Sov. Tech. Phys. Lett. **15**, 269 (1989)].
8. V. G. Samsonov and I. M. Vinitskiĭ, *Handbook of Refractory Compounds* (Metallurgiya, Moscow, 1976; Plenum Press, New York, 1980).
9. M. Parschan and K. Cristmann, Surf. Sci. **347**, 63 (1996).
10. N. R. Gall', E. V. Rut'kov, and A. Ya. Tontegode, Fiz. Tverd. Tela (St. Petersburg) **44**, 1332 (2002) [Phys. Solid State **44**, 1394 (2002)].
11. N. R. Gall', E. V. Rut'kov, and A. Ya. Tontegode, Zh. Tekh. Fiz. **60** (4), 125 (1990) [Sov. Phys. Tech. Phys. **35**, 475 (1990)].
12. N. R. Gall, S. N. Mikhailov, E. V. Rut'kov, and A. Ya. Tontegode, Surf. Sci. **191**, 185 (1987).
13. M. Guttmann and D. McLean, *Interfacial Segregation*, Ed. by W. C. Johnson and J. M. Blakely (Am. Soc. Metals, Ohio, 1979), pp. 261–347.
14. H. B. Gray, *Electrons and Chemical Bonding* (Benjamin, New York, 1964; Mir, Moscow, 1967).
15. V. S. Fomenko, *Emission Properties of Materials: A Handbook* (Naukova Dumka, Kiev, 1981) [in Russian].

Translated by P. Pozdeev

Technical Physics Letters, Vol. 30, No. 3, 2004, pp. 197–199. Translated from Pis'ma v Zhurnal Tekhnicheskoĭ Fiziki, Vol. 30, No. 5, 2004, pp. 54–59.

Modeling the Process of Impurity Removal from Semiconductor Wafers in Inhomogeneous Temperature Field

V. I. Rudakov*, A. V. Bashmakov, and V. V. Ovcharov

Institute of Microelectronics and Informatics, Russian Academy of Sciences, Yaroslavl, Russia

** e-mail: vir@uniyar.ac.ru*

Received July 21, 2003

Abstract—A sufficiently high temperature gradient in the direction perpendicular to the surface of a semiconductor wafer forces impurities occurring in the subsurface region to emerge at the surface. The process of impurity thermodiffusion was numerically calculated for the initial impurity distributions in the form of a Gaussian source or a uniform layer. The curves illustrating the kinetics of impurity accumulation at the surface are obtained and the stationary solutions are found, which coincide in the two cases provided that the initial impurity content was the same. © *2004 MAIK "Nauka/Interperiodica".*

An important problem in integrated circuit (IC) technology is the preliminary gettering of undesired impurities from silicon wafers aimed at obtaining pure and structurally perfect single crystal substrates. Since ICs are fabricated using predominantly the near-surface layers, it is of primary importance to remove impurities from this very region. At present, this task is usually solved by methods driving impurities toward the rear wafer surface or into the bulk, with the formation of deep buried precipitates. In this case, undesired impurities are removed from the working layers but are still present in the vicinity of this region [1]. It would be of interest to search for new methods of gettering impurities which would provide for their complete removal.

Kamenetskaya *et al.* [2] suggested using a temperature gradient for the band purification of single crystal ingots from impurities in the solid state. The idea is that the temperature field would drive the impurity to emerge at the edge surface, after which it can be eliminated by etching. The applicability of this approach to gettering impurities from semiconductor wafers was indirectly confirmed by the results of our experiments [3] where oxygen atoms moved under the action of a temperature gradient to form buried SiO_2 layers in the course of nonisothermal annealing of silicon implanted with oxygen ions. The direction of oxygen diffusion depended on that of the temperature gradient.

This Letter presents the results of our theoretical investigation of the possibility of removing impurities from the working regions of semiconductor wafers under the action of a temperature gradient.

Let us consider a one-dimensional flow of impurity atoms related to the concentration and temperature gradients by the equation [4]

$$J = -D\left(\frac{\partial C}{\partial x} + \frac{CQ^*}{kT^2}\frac{\partial T}{\partial x}\right), \quad (1)$$

where $C = C(x, t)$ is the impurity concentration, $T = T(x)$ is the absolute temperature, $D = D_0\exp[-E/kT(x)]$ is the diffusion coefficient, D_0 is the preexponential factor, E is diffusion activation energy, k is the Boltzmann constant, and Q^* is the heat of transfer.

As can be seen from Eq. (1), the magnitude and direction of the impurity flux in an inhomogeneous temperature field with a given temperature gradient are determined by the heat of transfer. Under these conditions, the process of impurity redistribution depending on the coordinate x and time t is described by the equation

$$\frac{\partial C}{\partial t} = \frac{\partial}{\partial x}\left[D\left(\frac{\partial C}{\partial x} + \frac{Q^*C}{kT^2}\frac{\partial T}{\partial x}\right)\right]. \quad (2)$$

The model system is a thin film of thickness $l \sim 25$ μm with reflecting boundaries applied onto a semiconductor plate (substrate). The film surfaces are maintained at different temperatures. If the thermal conductivity of the film material is constant in time and independent of the coordinates, a linear temperature profile $T(x) = T_0 + Gx$ will be established across the film within a short time, where G is the constant temperature gradient.

A solution to Eq. (2) will be found for two cases usually encountered in semiconductor technology. In case 1, the impurity is concentrated at a certain distance from the film surface. Let the initial impurity profile be

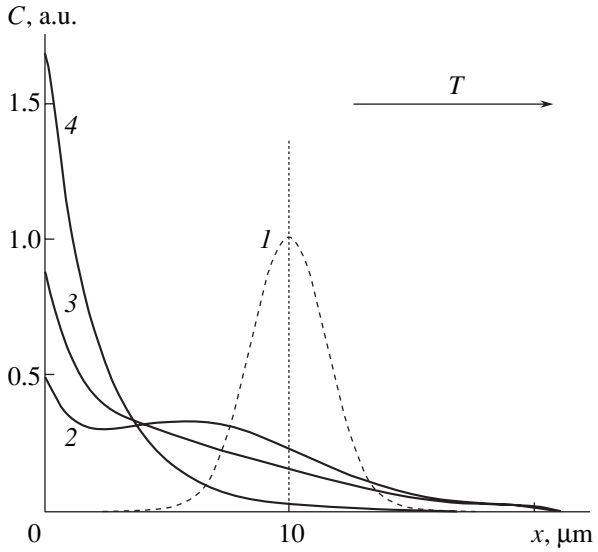

Fig. 1. Impurity depth–concentration profiles calculated in case 1 for T_0 = 1000°C, Q^* ~ 2.6 eV, $\nabla T = 10^5$ K/cm and various diffusion times: (*1*) initial Gaussian distribution; (*2*) $t \sim 10^4$ s; (*3*) $t \sim 1.5 \times 10^4$ s; (*4*) $t > 3.6 \times 10^5$ s (stationary state). The arrow indicates the direction of temperature increase.

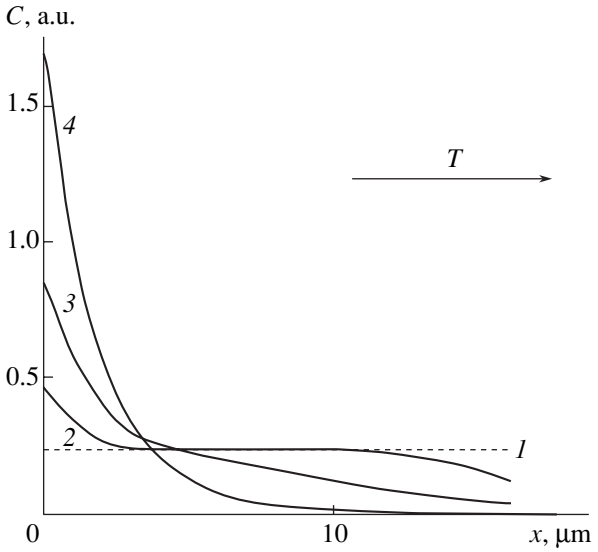

Fig. 2. Impurity depth–concentration profiles calculated in case 2 for T_0 = 1000°C, Q^* ~ 2.6 eV, $\nabla T = 10^5$ K/cm and various diffusion times: (*1*) initial uniform distribution; (*2*) $t \sim 10^4$ s; (*3*) $t \sim 1.5 \times 10^4$ s; (*4*) $t > 3.6 \times 10^5$ s (stationary state). The arrow indicates the direction of temperature increase.

described by the Gaussian distribution with the center displaced to a depth of 10 μm from the surface $x = 0$:

$$C = \exp(-\alpha \times x^2), \tag{3}$$

where $\alpha \sim 2 \times 10^{-11}$ m^{-2}. The boundary conditions are as follows:

$$\begin{cases} J(0, t) = 0, \\ C(l, t) = 0. \end{cases} \tag{4}$$

In case 2, the impurity is initially uniformly distributed across the film, so that C = const and the corresponding boundary conditions are

$$\begin{cases} J(0, t) = 0, \\ J(l, t) = 0. \end{cases} \tag{5}$$

For the sake of simplicity, the total amount of impurity atoms in both cases is assumed to be the same:

$$\int_0^l C_1(x)dx = \int_0^l C_2(x)dx = M, \tag{6}$$

where C_1 and C_2 are the impurity profiles in cases 1 and 2, respectively. The problem was numerically solved on a computer for the following parameters: substrate surface temperature, T_0 = 1000°C; temperature gradient, $G = 10^5$ K/cm; and heat of transfer, $Q^* \sim 2.6$ eV.

Figure 1 shows the impurity depth–concentration profiles obtained in case 1 for various times of diffusion. As can be seen for the time $t \sim 10^4$ s (curve *2*), the peak of the Gaussian distribution shifts toward the surface $x = 0$ and decreases in amplitude. This implies that all impurity atoms are driven toward the surface by a force caused by the temperature gradient. Since the surface is assumed to possess reflecting properties, the impurity accumulates in the vicinity of this boundary. When the diffusion time increases to $t \sim 1.5 \times 10^4$ s, the Gaussian distribution exhibits virtually complete blurring (curve *3*). As the diffusion proceeds further ($t \sim 3.6 \times 10^5$ s), the system attains a stationary state, whereby the flux of atoms related to the concentration gradient is compensated by the opposite flux of atoms driven by the temperature gradient (curve *4*). In this state, the impurity profile no longer changes and the surface concentration acquires the stationary value $C = C_s$. According to Eq. (1), this state mathematically corresponds to $J = 0$.

Figure 2 shows the impurity depth–concentration profiles for case 2. In the initial state with a uniform distribution of the diffusant in depth of the sample (curve *1*), a flux due to the concentration gradient is absent and the impurity redistribution is caused only by the temperature gradient. As can be seen, the concentration of impurity atoms at a certain distance from the surface remains unchanged for a time of $t \sim 10^4$ s (curve *2*) and the diffusant flux at this distance is constant. This

behavior agrees with Eq. (2): if a constant concentration $C(x, t) = C(x_0, t) = C_0$ is retained in the vicinity of a certain point $x = x_0$, the concentration will remain constant during the time of existence of such a region. With time, the diffusion modifies the right-hand part of the impurity profile (curve *3*). After diffusion for a sufficiently long time (curve *4*), the impurity profile becomes identical to that obtained for the stationary regime in case 1. Therefore, stationary solutions for the two initial conditions are the same for otherwise identical conditions and equal initial amounts of the impurity.

Thus, the results of our theoretical investigation show that, irrespective of the initial impurity distribution in the subsurface region, the temperature gradient drives the impurity to concentrate at the surface of a semiconductor wafer. For the same initial content of impurity atoms, their stationary depth–concentration profiles have the same shape, provided that the surface concentration does not exceed the solubility limit.

REFERENCES

1. *VLSI Technology*, Ed. by S. M. Sze (McGraw-Hill, New York, 1983; Mir, Moscow, 1986), Vol. 1.
2. D. S. Kamenetskaya, I. B. Piletskaya, and V. I. Shiryaev, Dokl. Akad. Nauk SSSR **178**, 323 (1968).
3. V. I. Rudakov, Yu. N. Denisenko, and B. V. Mochalov, Mikroélektronika **29**, 367 (2000).
4. V. I. Rudakov and V. V. Ovcharov, Int. J. Heat Mass Transf. **45**, 743 (2002).

Translated by P. Pozdeev

Technical Physics Letters, Vol. 30, No. 3, 2004, pp. 200–201. Translated from Pis'ma v Zhurnal Tekhnicheskoĭ Fiziki, Vol. 30, No. 5, 2004, pp. 60–63.

Detecting Mixed State in $YBa_2Cu_3O_{7-x}$ Superconductors by Method of Acoustic Emission

E. Dul'kin

School of Applied Science, The Hebrew University of Jerusalem, Jerusalem 91904, Israel

e-mail: dulkin@pob.huji.ac.il

Received August 18, 2003

Abstract—The formation of a mixed state in $YBa_2Cu_3O_{7-x}$ superconductors during the transport current buildup (i.e., under the action of the internal magnetic field) at $T = 77$ K was detected by method of acoustic emission (AE). The AE signals were detected for the currents of $I = 0.5$ and 2.7 A. The former signal corresponds to the lower critical magnetic field (H_{c1}), as was established previously [4]. It is shown that the latter signal corresponds to the formation of a mixed state. Application of the AE method to detecting overloads in high-power superconducting circuits is considered. © *2004 MAIK "Nauka/Interperiodica".*

One of the main features of type II high-T_c superconductors is the penetration of magnetic field into such materials in the form of vortices, leading to the formation of a mixed state. The field penetration implies surmounting a surface barrier related to the Meissner effect and takes place when an external magnetic field (or the internal field induced by the transport current) exceeds the lower critical field H_{c1}. As the magnetic field strength increases, the vortices penetrate deeper into the material, meet at the center of the sample, and form a triangular lattice at a magnetic field H_s corresponding to the mixed state [1]. The formation of the mixed state leads to a significant decrease in the critical current I_c, thus making the use of high-T_c wires practically impossible.

Altshuler *et al.* [2] determined the H_s value in the samples of $YBa_2Cu_3O_{7-x}$ ceramics by measuring the decrease in I_c with increasing external field strength H. However, the $I_c(H)$ curve measured in this way is somewhat smeared, which hinders accurate determination of H_s. More recently, Arzhavitin *et al.* [3] measured H_c and H_s for $YBa_2Cu_3O_{7-x}$ ceramics with a 2 × 2-mm cross section using the method of internal friction sensitive to the vortex pinning on defects. The values of $H_{c1} = 90$ Oe was determined at the onset of buildup in the internal friction exhibiting saturation with increasing external field strength. In view of the saturation, only a lower boundary of ~350 Oe was given for the field strength at which the mixed state begins to form [3].

In recent years, high-T_c superconductors have been successfully studied by the method of acoustic emission (AE). A mechanism accounting for the possibility of using this method is related to the vortex pinning on (or interaction with) defects in the material, leading to the emission of elastic acoustic waves. Previously [4], the value of H_{c1} was determined for $YBa_2Cu_3O_{7-x}$ ceramics with a 5 × 5-mm cross section using the AE signal observed during an increase in the transport current in the internal field. A clear peak in the AE intensity $\dot{N}$ was detected at $I = 0.5$ A, corresponding to $H_{c1} = 104$ Oe. Recently [5], the AE was studied in $YBa_2Cu_3O_{7-x}$ ceramics with a 5 × 5-mm cross section exposed to an external magnetic field. These experiments showed the presence of two AE peaks corresponding to $H_{c1} = 100$ Oe and $H_s = 2500$ Oe.

While the lower critical fields H_{c1} reported in [3–5] show satisfactory agreement, the H_s values exhibit significant scatter. Coincidence of the H_{c1} values is evident, since the critical field is virtually independent of the sample geometry. On the contrary, the scatter in H_s can be related both to differences in the sample cross section and to the influence of individual sample parameters, such as the grain size and shape, and the presence of second phases, microcracks, etc.

This Letter reports on the result of investigations of the AE intensity $\dot{N}$ in the samples of $YBa_2Cu_3O_{7-x}$ ceramics under the action of a transport current (i.e., in the intrinsic field), aimed at determining the moment of formation of the mixed state.

The experiments were performed with samples of $YBa_2Cu_3O_{7-x}$ ceramics with the dimensions 5 × 5 × 20 mm. The material was characterized by $T_c = 92$ K, $\Delta T_c = 0.2$ K, $\rho \sim 4.7$ g/cm^3, and $I_c = 2.5$ A (four-point-probe dc measurements) at a voltage drop of 1 μV/cm. The AE measurements were carried out as described in [4]. The sample was glued with superglue to the edge of a quartz cylindrical acoustic waveguide, while a TsTS-19 (PZT ceramics) based piezoelectric AE sensor was glued with an epoxy resin to the opposite waveguide end. Electrodes were connected to the oppo-

1063-7850/04/3003-0200$26.00 © 2004 MAIK "Nauka/Interperiodica"

site sample edges with the aid of a silver paste. The waveguide with the sample was placed into a Dewar vessel with liquid nitrogen, after which a dc current increasing at a rate of 0.5 A/s was passed through the sample. The AE intensity $\dot{N}$ as a function of the current was measured on a real-time scale with the aid of an analog-to-digital converter DT-302(01) connected to a personal computer. In order to eliminate the experimental error related to the magnetic flux trapping, each subsequent measurement was performed on a new sample.

The results of these measurements are presented in the figure. During the transport current buildup, the AE intensity $\dot{N}$ exhibited two peaks, analogous to those observed in an external magnetic field [5]. The first AE peak observed at $I = 0.5$ A confirms the results obtained previously [4] under analogous experimental conditions. The second maximum is observed at a current somewhat greater than I_c ($I = 2.7$ A $\approx 1.1I_c$). The $\dot{N}$ value for this maximum exceeds that of the first peak by a factor of more than four. This difference in the AE intensity $\dot{N}$ is related to the difference in the number of vortices. In the case of penetration through the surface barrier, vortices exhibit pinning in the near-surface region, while vortices forming the mixed state interact over the entire sample volume. For this reason the intense AE peak allows the moment of formation of the mixed state in $YBa_2Cu_3O_{7-x}$ ceramics with sufficiently high precision.

It should be noted that the investigations of losses in high-T_c $(Bi,Pb)_2Sr_2Ca_2Cu_3O_x$ ribbons and wires showed that the level of losses sharply increases for the transport currents about $(1.1–1.3)I_c$ [6–8]. These data are consistent with the result obtained in this study, where a clear AE maximum was observed precisely at $I \approx 1.1I_c$.

Thus, the experimental results of this study and the above considerations show the applicability of the AE method both to determination of the mixed state formation and to detection of overloads in high-power superconducting circuits.

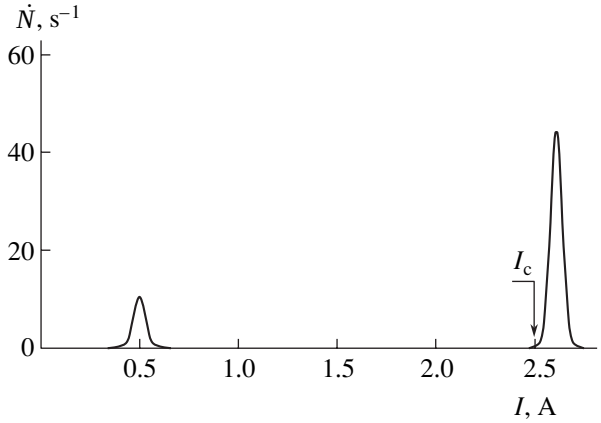

A plot of the AE intensity $\dot{N}$ versus increasing transport current in $YBa_2Cu_3O_{7-x}$ ceramics at 77 K.

REFERENCES

1. D. M. Ginsberg, *Physical Properties of High-Temperature Superconductors*, Ed. by D. M. Ginsberg (World Scientific, Singapore, 1989; Mir, Moscow, 1990).
2. E. Altshuler, S. Garcia, and J. Barrosso, Physica C **177**, 61 (1991).
3. V. M. Arzhavitin, N. N. Efimova, M. B. Ustimenkova, and V. A. Finkel', Fiz. Tverd. Tela (St. Petersburg) **42**, 1361 (2000) [Phys. Solid State **42**, 1398 (2000)].
4. E. Dul'kin, V. Beilin, E. Yashchin, *et al.*, Supercond. Sci. Technol. **15**, 1081 (2002).
5. E. Dul'kin and M. Roth, Supercond. Sci. Technol. **16**, 361 (2003).
6. N. Savvides, J. Herrmann, D. Reilly, *et al.*, Physica C **306** (1–2), 129 (1998).
7. S. Fleshler, L. T. Cronis, G. E. Conway, *et al.*, Appl. Phys. Lett. **67**, 3189 (1995).
8. T. Fukunaga, T. Abe, and A. Oota, Appl. Phys. Lett. **66**, 2128 (1995).

Translated by P. Pozdeev

Technical Physics Letters, Vol. 30, No. 3, 2004, pp. 202–204. Translated from Pis'ma v Zhurnal Tekhnicheskoĭ Fiziki, Vol. 30, No. 5, 2004, pp. 64–69.

Viscoelastic Recovery of Various Materials in the Region of a Dynamic Nanocontact

Yu. I. Golovin*, V. I. Ivolgin, and R. I. Ryabko

Tambov State University, Tambov, Russia

** e-mail: golovin@tsu.tmb.ru*

Received August 13, 2003

Abstract—The process of elastic and viscoelastic recovery in locally strained submicron regions in various solids has been studied. The influence of the scale and loading rate factors on the process parameters is revealed.

In recent years, several domestic and foreign (IBM, Hewlett-Packard, Hitachi, Nanochip, Seagate) companies have been extensively developing the systems of high-density data recording by method of dynamic local straining of the surface of a recording medium [1, 2]. Using this method stipulates detailed knowledge of the mechanical properties of a material for recording on a submicroscopic scale, which may significantly differ for many reasons from the macroscopic properties of this material. In particular, the magnitude and kinetics of the elastic and viscoelastic recovery upon unloading has never been studied under the conditions of short-time local straining. However, this factor may determine the operation speed and reliability of the aforementioned systems of data recording and readout. In addition, the dynamic response in nanocontacts determines various characteristics of a surface with microroughnesses, including the parameters of dry friction, abrasive wear, etc.

Data on the elastic recovery of the indenter impression size in various materials probed to a depth of $h > 1$ μm were reported in [3, 4]. However, the viscoelastic recovery was studied only in polymeric materials, since it was believed that the extent of this recovery in materials of other types is negligibly small. In particular, the kinetics of viscoelastic recovery in poly(methyl methacrylate) (PMMA), poly(ethylene), and gelatin films was studied at a time resolution of about 1 s [5–7].

The method of nanoindentation, ensuring high spatial and temporal resolution, allows the above situations to be modeled under thoroughly controlled conditions. This is achieved through continuous monitoring of the indentation depth h as a function of the load P, which provides valuable information about the kinetics and mechanisms of local straining, the structure of a material in the region of indentation, etc. Using modern nanoindenters, it is possible to study time-dependent characteristics of a probed material both in the stage of loading and in the course of elastic or viscoelastic recovery upon unloading [8, 9].

This study was aimed at elucidating the influence of the scale factor on the elastic and viscoelastic recovery in the region of a dynamic nano- and microcontact between a sharp indenter and various solids, including ionic and covalent crystals, metals and alloys, polymeric materials, and ceramics.

The experiments were performed with a series of materials including PMMA, ZrO_2 based ceramics, LiF and Ge single crystals, polycrystalline Al and Cu, Wood's alloy (50% Bi, 25% Pb, 12.5% Sn, 12.5% Cd), and Rose's alloy (50% Bi, 28% Pb, 22% Sn). These materials represent the main groups of solids with respect to hardness, the nature of binding forces, and the microscopic mechanisms of plastic straining.

The measurements were performed at 296 K with an original nanoindentometer possessing high spatial (up to 1 nm) and temporal (50 μs) resolution. The device is described in more detail elsewhere [8]. The indenter had the form of a trihedral Bercovic diamond pyramid. In the first series of experiments, the indenter was incorporated into a polished sample surface under the action of delta-shaped impulses of force with various amplitudes P_{max} = 4–235 mN, so that the same maximum dynamic indentation depth h_{max} = 650 nm would be reached in various materials for the times of load buildup τ_1 = 10 s and decay τ_2 = 200 ms. In order to provide for a reliable contact of the indenter with the impression upon load-off, the residual load was maintained on a level of several percent of P_{max}. In this regime, the nanoindentometer measured the indentation depth, which varied with time as a result of the relaxation processes.

We have measured the "instantaneous" elastic recovery Δh_e (determined as the recovery during unloading within τ_2 = 200 ms), viscoelastic recovery Δh_{ve} (within τ_3 = 25 s upon complete load-off), and total recovery Δh (over the time $\tau = \tau_2 + \tau_3$) normalized to h_{max}. The relative characteristics for various materials are presented in Fig. 1. It was found that, for the fixed

maximum dynamic indentation depth h_{max} = 650 nm, the value of $\beta = \Delta h_e/h_{max}$ was maximum in Ge, ZrO_2 based ceramics, and PMMA (50–55%), while not exceeding 18% in all other materials. The relative viscoelastic recovery $\gamma = \Delta h_{ve}/h_{max}$ was rather high in all studied materials, varying from 5% in Al to 28% in Wood's alloy (the latter value even exceeds the analogous characteristic for PMMA).

An analysis of the results of determination of the values of Δh, Δh_e, and Δh_{ve} as functions of the maximum indentation depth h_{max} showed that these recovery characteristics are very sensitive with respect to the scale factor, especially in the interval of 50 nm < h_{max} < 1 μm (Fig. 2). As the value of h_{max} decreases in this interval, the elastic recovery in metals and in ionic and covalent crystals (exhibiting predominantly elastic character of recovery) increased by a factor of two and above. For PMMA and Rose's alloy, Δh_e in the same interval varied by 10–30%, while Δh_{ve} changed by a factor greater than two. The samples of Ge and Cu showed a significant increase in Δh_{ve} in a narrow interval of 50 nm < h < 200 nm.

It was also established that complete recovery in all studied materials depends on the rate of loading $R = dP/dt$. As R was increased from 2 mN/s to 1 N/s (this was achieved by decreasing τ_1 to 0.05 s for various P_{max}), the ratio $\alpha = \Delta h/h_{max}$ increased by 15–40%, depending on the particular material. In the case of Ge, the rather high value of the total recovery was attributed to a considerable elastic component (up to 90%). In Wood's alloy, the elastic and viscoelastic recovery values were on the same order of magnitude; moreover, Δh_{ve} even exceeded Δh_e at low loading rates. When R increased in the aforementioned interval, the contribution of Δh_{ve} to the total recovery decreased by a factor varying from 1.5 (PMMA) to 2 (Ge).

It should be noted that the lower the rate of unloading and the temporal resolution of instrumentation, the greater part of the time-dependent viscoelastic recovery will appear as elastic. It is possible that even the rather high rates of unloading and fast system response (50 μs between measurements) achieved in our experiments were insufficient for completely eliminating this uncertainty.

In the materials with $\beta > \gamma$, the value of Δh_e was most sensitive with respect to variations of the indentation depth. In solids with $\beta \approx \gamma$ (PMMA and Rose's alloy), the passage to small indentation depths most significantly influenced Δh_{ve}. As the h_{max} value decreases, the fraction of elastic recovery grows and that of the viscoelastic recovery drops in all studied materials. This behavior is probably related to the fact that, on the passage to small indentation depths, some viscoelastic recovery mechanisms are blocked and the relative contribution of Δh_e increases. The increase in γ observed for some materials in the region of h < 200 nm can be attributed both to certain features of their surface properties and to switching of some special mechanisms of the structural relaxation (suppressed by the traditional mechanisms at large indentation depths). In particular, in ionic and covalent crystals, a decrease in P_{max} and

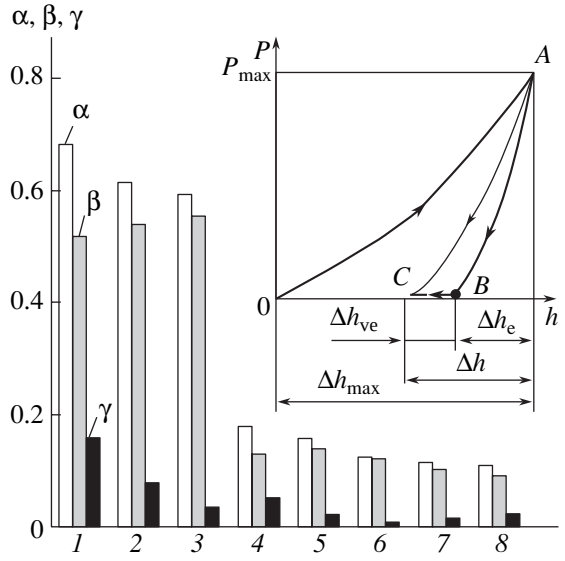

Fig. 1. A histogram of the relative values of the total ($\alpha = \Delta h/h_{max}$), elastic ($\beta = \Delta h_e/h_{max}$), and viscoelastic ($\gamma = \Delta h_{ve}/h_{max}$) indentation recovery characteristics for various materials: (*1*) PMMA; (*2*) ZrO_2 based ceramics; (*3*) Ge; (*4*) Wood's alloy; (*5*) LiF; (*6*) Al; (*7*) Cu; (*8*) Rose's alloy. Maximum dynamic indentation depth for all materials was h_{max} = 650 nm. The inset presents the plots of load P versus depth h, showing the curves of purely elastic recovery upon fast unloading (*AB*), viscoelastic recovery (*BC*), and the recovery during slow unloading (*AC*).

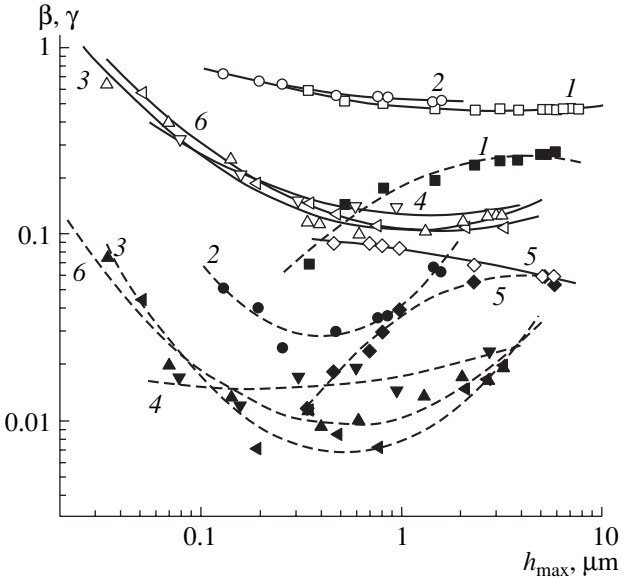

Fig. 2. Plots of the relative elastic recovery β (open symbols, solid curves) and viscoelastic recovery γ (black symbols, dashed curves) versus maximum dynamic indentation depth h_{max} for (*1*) PMMA, (*2*) Ge, (*3*) Cu, (*4*) LiF, (*5*) Rose's alloy, and (*6*) Al.

h_{max} is accompanied by an increase in the role of point defects and by a decrease in the influence of dislocations [9, 10].

Thus, using the dynamic nanoindentation technique, we have determined for the first time the relative contributions of the elastic and viscoelastic components in the recovery of various solids, studied the recovery characteristics as functions of the loading rate, and revealed their sensitivity to the scale factor. It was found that the relative recovery characteristics β and γ determined under identical loading conditions vary in the series of solid materials studied and, hence, can be considered as characteristic parameters of a given material. An approach has been developed for determining the influence of the scale factor and the loading rate on the recovery kinetics. These results can be of practical significance, in particular, in the development of systems of high-density data recording employing the principle of nanoindentation.

Acknowledgments. This study was supported by the Russian Foundation for Basic Research (project no. 01-02-16573) and the Ministry of Education of the Russian Federation (Natural Sciences Program, project no. E00-3.4 -263).

REFERENCES

1. G. Binnig and H. Rohrer, Rev. Mod. Phys. **71**, 324 (1999).
2. P. Vettiger, G. Cross, M. Despont, *et al.*, IEEE Trans. Nanotechnol. **1**, 39 (2002).
3. S. I. Bulychev and V. P. Alekhin, *Testing Materials by Continuous Indentation* (Mashinostroenie, Moscow, 1990) [in Russian].
4. Yu. S. Boyarskaya, D. Z. Grabko, and M. S. Kats, *Physics of Microindentation Processes* (Shtiintsa, Kishinev, 1986) [in Russian].
5. J. C. Merino, B. Martin, and J. M. Pastor, Meas. Sci. Technol. **2**, 740 (1991).
6. M. J. Adams, D. M. Gorman, S. A. Johnson, *et al.*, Philos. Mag. A **82**, 2121 (2002).
7. B. Y. Ni, G. R. Bisson, and A. H. Tsou, Mater. Res. Soc. Symp. Proc. **308**, 489 (1993).
8. Yu. I. Golovin, A. I. Tyurin, V. I. Ivolgin, and V. V. Korenkov, Zh. Tekh. Fiz. **70** (5), 82 (2000) [Tech. Phys. **45**, 605 (2000)].
9. Yu. I. Golovin and A. I. Tyurin, Materialovedenie, No. 1, 14 (2001); No. 2, 19 (2001).
10. Yu. I. Golovin, A. I. Tyurin, and B. Y. Farber, J. Mater. Sci. **37**, 895 (2002).

Translated by P. Pozdeev

Technical Physics Letters, Vol. 30, No. 3, 2004, pp. 205–207. Translated from Pis'ma v Zhurnal Tekhnicheskoĭ Fiziki, Vol. 30, No. 5, 2004, pp. 70–75.

The Structure of Thermomigration Channels in Silicon

É. Yu. Buchin*, Yu. I. Denisenko, and S. G. Simakin

Institute of Microelectronics and Informatics, Russian Academy of Sciences, Yaroslavl, Russia

** e-mail: imi.buchin@rambler.ru*

Received September 3, 2003

Abstract—We have studied deep and through channels formed in *n*-Si wafers by means of thermal migration of thin discrete aluminum zones. The region of thermal migration channels was investigated using selective chemical etching of silicon in combination with secondary ion mass spectrometry for the analysis of impurity distributions. It is established that the channels are surrounded by two distinct peripheral shells. © *2004 MAIK "Nauka/Interperiodica".*

The process of thermal migration of liquid inclusions in the volume of a solid, also known as the method of temperature-gradient zone melting, was originally developed in the mid-1950s [1]. The essence of this process consists in sequential recrystallization of the solid by a liquid zone moving under the action of a temperature gradient. Using this method, it is possible to drive the eutectic zone of required composition at a rate significantly (by three to five orders of magnitude) exceeding that of solid-state diffusion. Thermal migration is widely employed in various technologies, in particular, in microelectronics, where this process is used to obtain buried doped regions of various shapes, through conducting channels, monolithic connections between semiconductor fragments, etc. The main laws, theoretical models, and technological regimes of various thermal migration processes are most exhaustively presented in monograph [2] and papers of the research group of Antony and Cline (see reviews [3] and references therein).

This study was aimed at determining the structure and composition of the channels formed in *n*-Si wafers by means of thermal migration of thin discrete aluminum zones. This method of channel formation is among the least studied thermal migration processes.

Our experiments were performed with (100)-oriented silicon wafers of KEF-4.5 grade with a diameter of 100 mm and a thickness of 460 μm. The thermal migration process was effected in a thermal gradient setup employing IR heating [4]. The initial wafer with electron-beam-deposited 2- to 5-μm-thick aluminum pads of various shapes were heated from rear side up to a temperature of 1100°C. The temperature of the front side, on which the melted zone entered the substrate, was 8–10°C lower due to conductive heat exchange with a water-cooled copper substrate holder. The working chamber was filled with argon. The thermal migration time was varied from 10 to 45 min. In the case of through channels, the process termination was detected with the aid of a pyrometer.

Heating to the temperature indicated above results in the formation of liquid eutectic zones in the regions of contact between aluminum and silicon, which move toward the hot side of the plate under the action of the temperature gradient. The process of thermal migration of aluminum proceeds by means of silicon dissolution at the hot front of the zone, diffusion transfer via the melt, and crystallization at the cold end of the zone. A certain fraction of aluminum is retained in the recrystallized region, while the maximum metal concentration of $(1–2) \times 10^{19}$ cm^{-3} is on the channel axis. The metal also partly crosses the metallurgical boundary as a result of diffusion. The shape of the aluminum concentration profile in the channel cross section is close to erfc distribution. The passage of such discrete zone results in the formation of thermal migration channels of the *p* type in the *n*-Si substrate, with *p–n* junctions on the outer boundaries of the channels.

Since the initial silicon grown by the Czochralski technique contains intrinsic impurities (phosphorus, 5×10^{15} cm^{-3}; oxygen, ~10^{18} cm^{-3}), the process of thermal migration is accompanied by their redistribution as a result of thermodiffusion, zone refining, complex formation, etc. In addition, the propagation of a eutectic zone through single crystal silicon leads to the development of stresses in the wafer, which can result in a plastic shear at the metallurgical boundary. The lattice deformation also influences the distribution of impurities and defects at the channel boundaries. In order to obtain narrow recrystallized channels with a width not exceeding the size of the initial aluminum pads, it is recommended to use (100)-oriented silicon wafers and fine (below 20 μm) discrete zones. However, the edge effects, which are most pronounced during the thermal migration of fine zones, may significantly influence the composition and structure of the channels and, hence, the characteristics of *p–n* junctions.

We have studied the thermal migration channels using selective chemical etching of silicon in combination with secondary ion mass spectrometry (SIMS) for

1063-7850/04/3003-0205$26.00

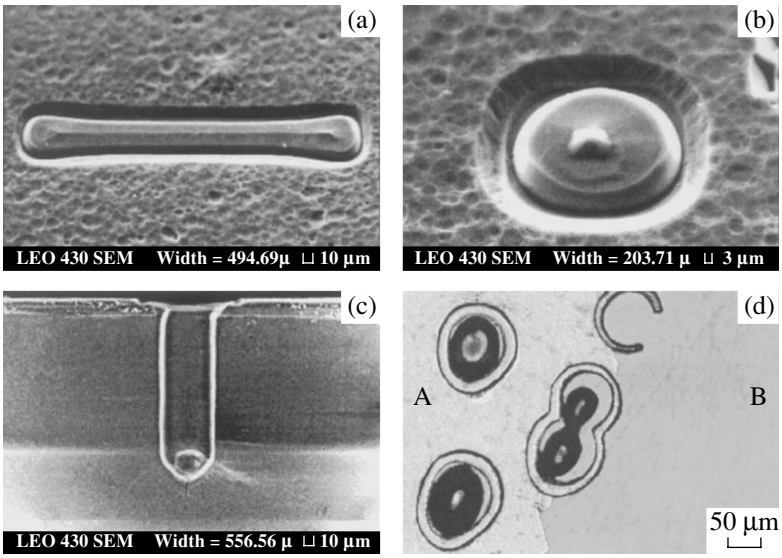

Fig. 1. (a–c) Scanning electron micrographs and (d) optical micrograph of the thermal migration channels upon selective etching (region A represents *n*-Si; region B is microscope glass). See the text for explanations.

the analysis of impurity distributions. The process of selective etching was performed in a mixture of aqueous hydrofluoric (48% HF), nitric (67–70% HNO_3), and glacial acetic acids taken in a 1 : 5 : 1 volume ratio. This mixture is characterized by different potentials for *n*- and *p*-Si, which results in the formation of a galvanic couple with *p* and *n* type regions acting as the anode and cathode, respectively. The anode region features oxidation and dissolution of silicon, while the dominating cathode process is HNO_3 reduction. As a result, the *p* type regions are etched at a higher rate [5]. In the presence of acetic acid, etching proceeds in a soft polishing regime. In order to exclude additional protoproduction of holes on the silicon surface, the etching was performed in the dark. In addition, chemical etching reveals the regions containing crystallographic defects, dislocation pileups, etc., where the reaction of silicon oxidation proceeds at a higher rate.

The results of etching of the thermal migration channels are presented in Fig. 1. The electron micrographs in Figs. 1a and 1b show the patterns observed at the sites on the sample surface where the eutectic zones enter into silicon. The data are presented for two channels with different shapes of cross sections in the sample plane upon 20-s etching in the acid mixture. As a result of this short-time treatment, the central channel body was faceted in (111) directions and several-micron-wide region at the channel periphery was deeply etched, while the initial *n*-Si substrate surface remained virtually intact. Figure 1c is a micrograph of the etched surface of a transverse cleavage, showing a deep channel with a solidified eutectic zone on the bottom. As can be seen, the region of selective etching (dark field) extends along the entire channel length. The channel is also surrounded by a clearly distinguished bright contour approximately several microns wide. This region was not etched during the short-time treatment and exhibited charging and bright luminescence when scanned in the electron microscope. The two regions represent shells surrounding the channel body in the region of the metallurgical boundary. Figure 1d shows the result of a long (30 min) etching of a sample containing several through thermal migration channels. This micrograph clearly illustrates the difference in the etching rates of various structural elements of the channels: the inner shells completely dissolved, the central channel bodies decreased in diameter (and sometimes fell out of the channels), and the outer shells retained their shape. Thus, the selective chemical etching revealed the presence of two distinct shells possessing different physicochemical properties.

In order to determine the compositions of these shells, we have analyzed the corresponding regions by SIMS to determine the distributions of impurities in the channel cross section. The measurements were performed with a CAMECA IMS-4F ion microprobe using oxygen and nitrogen primary ion beams. The size of the secondary ion take-off region determining the spatial (lateral) resolution was 33 and 8.3 µm, respectively. In order to increase the sensitivity of SIMS during measurements of the phosphorus profile, the working chamber was filled with oxygen. Figure 2b shows averaged and smoothened concentration profiles of aluminum, phosphorus, and oxygen. As can be seen from these data, the outer shell is characterized by an increased content of oxygen and phosphorus. These inhomogeneities in the impurity concentrations are probably due to interplay of the gettering and thermodiffusion processes at the phase boundary. Thus, the outer shell can be considered as an n^+ type region, in

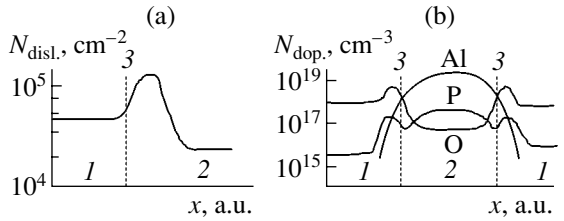

Fig. 2. The profiles of (a) dislocation density and (b) impurity concentrations across thermal migration channels: (*1*) initial silicon substrate; (*2*) thermal migration channel; (*3*) metallurgical boundary.

good agreement with the above data on the selective etching according to which the outer shell was dissolved at a minimum rate (even slower than the initial *n*-Si substrate). The region of the inner shell does not contain any acceptor impurities. Increased etching rate in this region is probably explained by increased density of defects. Figure 2a shows the distribution of dislocation density in the vicinity of the metallurgical boundary, constructed based on the data reported in [6]. The increase in the density of dislocations near the channel boundaries is related to mechanical stresses arising during the passage of the melted zone.

Upon additional thermal annealing of the samples for 2 h at 1200°C, the thickness of the inner shell was somewhat reduced as a result of stress release. On the contrary, the outer shell exhibited a severalfold increase in thickness and smeared boundaries as a result of impurity diffusion.

In conclusion, the results of this study showed that thermal migration channels formed in *n*-Si wafers by means of thermal migration of thin discrete aluminum zones possess an inhomogeneous structure. Two distinct shells with different physicochemical properties are found at the periphery of each channel. These shells may significantly influence the characteristics of *p–n* junctions in the channels.

REFERENCES

1. W. G. Pfann, J. Metals **7**, 961 (1955).
2. V. N. Lozovskiĭ, L. S. Lunin, and V. P. Popov, *Temperature-Gradient Band Recrystallization of Semiconductor Materials* (Metallurgiya, Moscow, 1987) [in Russian].
3. V. I. Rudakov and L. A. Koledov, Zarubezhn. Élektron. Tekh., Nos. 3–4, 27 (1993); Nos. 5–6, 25 (1993).
4. V. B. Mochalov and V. I. Rudakov, Prib. Tekh. Éksp., No. 2, 155 (1996).
5. F. F. Red'ko and S. O. Izidinov, Élektrokhimiya **2**, 1128 (1966); **2**, 1282 (1966); **12**, 1494 (1976).
6. G. A. Wolf and A. I. Mlavski, in *Crystal Growth. Theory and Techniques*, Ed. by C. Goodman (Plenum, London, 1974; Mir, Moscow, 1977), Vol. 1, pp. 244–296.

Translated by P. Pozdeev

Technical Physics Letters, Vol. 30, No. 3, 2004, pp. 208–210. Translated from Pis'ma v Zhurnal Tekhnicheskoĭ Fiziki, Vol. 30, No. 5, 2004, pp. 76–81.

Evaluating the Attractor Dimension of a Nonlinear Oscillator

E. P. Seleznev and A. M. Zakharevich

Saratov Branch of the Institute of Radio Engineering and Electronics, Russian Academy of Sciences, Saratov, Russia

e-mail: sbire@sgu.ru

Received July 14, 2003

Abstract—The correlation dimension of a chaotic attractor of a nonautonomous nonlinear oscillator with variable control parameters is evaluated from experimental data. The dimension of a critical attractor shows good agreement with theoretical data. As the amplitude of the external action is varied, the chaotic attractor exhibits evolution such that the correlation dimension increases from a minimum value, determined by the properties of the critical attractor, to the nearest integer. © *2004 MAIK "Nauka/Interperiodica".*

Investigation into the dynamics of nonlinear systems on the modern level not only requires observation of the time series, phase portraits, and power spectra but also implies the evaluation of dimensional characteristics and calculation of the Lyapunov exponents and the system entropy. This study was aimed at the evaluation of the correlation dimension [1–9] of the attractor of a nonlinear nonautonomous oscillator and a change in this dimension depending on the control parameters for a particular case of the nonautonomous resonant circuit with a semiconductor diode.

The model system (Fig. 1a) is a series resonant circuit comprising a coil with the inductance L, a semiconductor diode D, and a resistor R. This resonator was driven by a harmonic oscillator via an amplifier with a sufficiently small output impedance. The linear (small-amplitude) resonance frequency of the circuit is 51 kHz. The time series of a current measured in resistor R was converted into a digital code with the aid of a 12-digit analog-to-digital converter (ADC) and fed into a personal computer. The ADC response time did not exceed 0.3 μs, which was much shorter than the period of oscillations in the circuit. Data stored in the computer were used to calculate the correlation dimension for a data array of 40000 points. The control parameters were the rms drive amplitude V and the drive frequency f.

Figure 1b shows the structure of the space of control parameters of the system studied, mapped as the drive amplitude V versus drive frequency f normalized to the linear resonance frequency f_r of the circuit.[1] Here, light regions correspond to periodic regimes, gray color indicates the regions of chaos, and digits indicate the oscillation period expressed in units of the drive signal period. Let the control parameter f be fixed in the vicin-

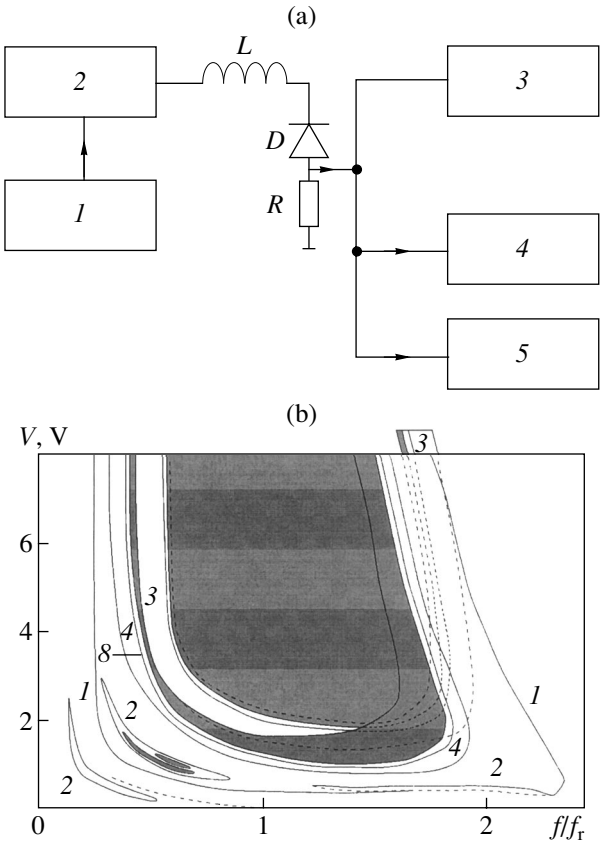

Fig. 1. Schematic diagrams showing (a) the experimental array (*1*, drive oscillator; *2*, amplifier; *3*, oscillograph; *4*, ADC; and *5*, spectrum analyzer) and (b) the space of control parameters (see the text for explanations).

[1] The dynamics of a resonant circuit with a p–n junction (semiconductor diode) has been rather exhaustively studied [10–15] and the plane of control parameters shows the standard phase diagram. Figure 1b is presented to indicate the region of control parameters for which the experimental data are obtained and processed.

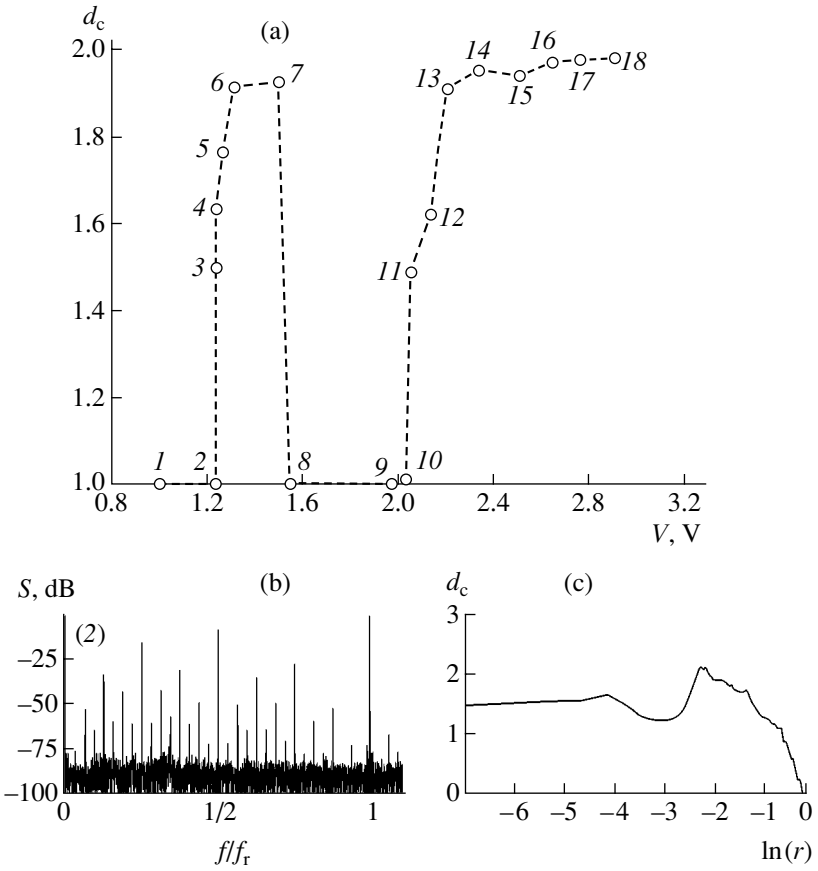

Fig. 2. Plots of (a) correlation dimension d_c of the attractor versus drive amplitude V and (b) oscillation power spectrum, and (c) plot of the d_c versus scale of observation at the boundary of the transition from order to chaos.

ity of the resonance. As the drive amplitude V is smoothly increased, the system exhibits a sequence of period doublings with the final transition to chaos. In the region of chaotic response, the phase diagram shows a sequence of merging bands, eventually forming a simply connected attractor. Further increase in the drive amplitude leads to the well-known sequence of cycles including period adding, transition to chaos, and crisis of chaotic attractor.

Figure 2a shows a plot of the correlation dimension of the chaotic attractor versus drive amplitude. For periodic regimes, the dimension is close to one and the power spectrum is discrete. In particular, $d_c = 1.01$ for the cycles of period 4 and period 8 (Fig. 2a, points *1* and *2*). At the boundary of the transition from order to chaos (point *3*), the estimated dimension is 1.48, in qualitative agreement with published data [16, 17]. In experiment, this boundary was determined using the power spectra, in which the harmonics multiple of $f/32$ were clearly distinguished, while the subharmonics of higher orders were smeared (Fig. 2b). Here, the dependence of the correlation dimension on the scale of observation exhibits a sloping region (Fig. 2c).

Since an increase in the drive amplitude V is accompanied by the appearance of "windows" corresponding to periodic regimes, the plot of the correlation dimension is nonmonotonic. For this reason, the dashed curve in Fig. 2a only reflects the tendency of d_c to increase (theoretically, this plot has a fractal structure). As can be seen from Fig. 2a, an increase in the parameter V leads to evolution of the system attractor, whereby the correlation dimension tends to two. The most pronounced changes in the chaotic attractor dimension are observed in the case of crisis. This is manifested by merging bands in the phase portrait and by smearing of the corresponding subharmonics in the power spectrum. Near the boundary of the transition to oscillations with period 3 (Fig. 2a, point *8*), the correlation dimension reaches the maximum value of 1.93. As the drive amplitude V increases further, the system exhibits the transition to a cycle of period 3 and, accordingly, the correlation dimension exhibits a sharp drop to $d_c = 1$.

Subsequent increase in the drive amplitude again leads to a sharp increase in the attractor dimension at the boundary of the transition from order to chaos (Fig. 2a, point *11*), where d_c tends to 2. The maximum value of 1.98 is reached at the boundary of the transition to a cycle of period 4 (Fig. 2a, point *18*).

Thus, the results of our analysis show that, as the drive amplitude increases, the chaotic attractor exhibits

evolution such that the correlation dimension increases from a minimum value, determined by the properties of the critical attractor, to the nearest integer.

Acknowledgments. This study was supported by the Russian Foundation for Basic Research (project no. 02-02-17578), the Program of Support for Young Scientists of the Russian Academy of Sciences (grant no. 23), and the US Civilian Research and Development Foundation for the Independent States of the Former Soviet Union (CRDF Award No. REG-006).

REFERENCES

1. P. Grassberger and I. Procaccia, Phys. Rev. Lett. **50**, 346 (1983).
2. G. Broggi, J. Opt. Soc. Am. B **5**, 1020 (1988).
3. P. S. Landa and M. G. Rozenblyum, Zh. Tekh. Fiz. **59** (11), 1 (1989) [Sov. Phys. Tech. Phys. **34**, 1229 (1989)].
4. H. D. I. Abarbanel and M. B. Kennel, Phys. Rev. E **47**, 3057 (1993).
5. M. Ding, C. Grebogi, E. Ott, *et al.*, Phys. Rev. Lett. **70**, 3872 (1993).
6. A. A. Kipchatov, Pis'ma Zh. Tekh. Fiz. **21** (15), 90 (1995) [Tech. Phys. Lett. **21**, 627 (1995)].
7. B. R. Hunt, E. Ott, and J. A. Yorke, Phys. Rev. E **54**, 4819 (1996).
8. R. Hegger, H. Kantz, and E. Olbrich, Phys. Rev. E **56**, 199 (1997).
9. S. A. Rakitin and E. P. Seleznev, in *Proceedings of the 5th International Workshop on Nonlinear Dynamics of Electronics Systems (NDES'97), Moscow, 1997*, pp. 376–380.
10. P. S. Linsay, Phys. Rev. Lett. **47**, 1349 (1981).
11. R. Buskirk and C. Jeffries, Phys. Rev. A **31**, 3332 (1985).
12. V. V. Astakhov, B. P. Bezruchko, and E. P. Seleznev, Radiotekh. Élektron. (Moscow) **32**, 2556 (1987).
13. A. A. Kipchatov, Izv. Vyssh. Uchebn. Zaved. Radiofiz. **33**, 182 (1990).
14. J. H. Baxter, M. F. Bocko, and D. H. Douglass, Phys. Rev. A **41**, 619 (1990).
15. B. P. Bezruchko, A. Yu. Zhalnin, M. D. Prokhorov, and E. P. Seleznev, Izv. Vyssh. Uchebn. Zaved., Prikl. Nelineĭnaya Din. **5** (2–3), 48 (1997).
16. T. S. Halsey, M. H. Jensen, L. P. Kadanoff, *et al.*, Phys. Rev. A **33**, 1141 (1986).
17. A. P. Kuznetsov and S. P. Kuznetsov, Izv. Vyssh. Uchebn. Zaved., Prikl. Nelineĭnaya Din. **1** (1–2), 15 (1993).

Translated by P. Pozdeev

Technical Physics Letters, Vol. 30, No. 3, 2004, pp. 211–213. Translated from Pis'ma v Zhurnal Tekhnicheskoĭ Fiziki, Vol. 30, No. 5, 2004, pp. 82–87.

Inhomogeneous Plastic Straining of Iron Based Amorphous Alloys

M. N. Vereshchagin, O. M. Ostrikov, and D. B. Zyukov

Gomel State Technical University, Gomel, Belarus

Received May 23, 2003; in final form, September 23, 2003

Abstract—Anisotropic plastic straining has been observed in iron based amorphous alloys. This phenomenon is explained proceeding from the notions about internal stresses in amorphous metal ribbons. © *2004 MAIK "Nauka/Interperiodica".*

Previously [1, 2], we have studied the formation of shear bands in the vicinity of indenter prints on the surface of amorphous metal alloys. This Letter reports on the new phenomenon of inhomogeneous plastic straining observed in isotropic amorphous media.

We have studied the samples of amorphous alloys of the following systems (wt %): $Fe_{81.4}$–$Cr_{4.0}$–$Mo_{6.0}$–$Ni_{5.2}$–$C_{1.0}$–$Mn_{2.1}$–$Al_{0.3}$; $Fe_{71.7}$–$Ni_{6.0}$–$Co_{2.4}$–$Cr_{7.5}$–$Mo_{7.9}$–$B_{4.0}$–$Si_{0.5}$; and Fe_{86}–$P_{9.8}$–$C_{1.0}$–$Si_{0.9}$–$Al_{1.7}$–$B_{0.6}$. The alloys in the form of amorphous ribbons were obtained by rapid quenching of the melt on the outer surface of a rotating copper disk [1, 2]. The cooling rate was 8×10^5 K/s. The thickness of ribbons varied within 50–80 μm.

The sample structure was studied by X-ray diffraction on a DRON-3 diffractometer using CuK_α radiation from an X-ray tube operating at a voltage of 30 kV and a current of 20 mA. The sample structure was also examined by optical microscopy (Neophot 21) and by scanning electron microscopy (CamScan-4).

The plastic straining of amorphous alloys was studied by the local deformation technique. According to this, the surface of an amorphous metal ribbon is deformed with a diamond pyramid (Vickers indenter) in a microhardness meter of the PMT-3 type [1, 2]. Then, the pattern of straining is examined in an optical microscope (or in more detail, in a scanning electron microscope). The results are evaluated in terms of the average number N_{st} of shear bands appearing at each face of the indenter. Indentation of the ribbon surface was performed at a load P varied from 0.25 to 1.50 N. The prints were oriented relative to the casting direction, as shown in Fig. 1. The measurements were performed on the side of the ribbon which was in contact with air during quenching. The analysis of straining was performed only for samples with approximately equal diameters of indenter marks.

The analysis of X-ray diffraction patterns showed that all the initial alloys are X-ray-amorphous. This was manifested by the absence of any peaks except a characteristic diffuse maximum corresponding to (011) reflection of α-Fe.

Figure 1 shows the typical pattern of straining observed at an indenter mark on the surface of an iron based amorphous alloy ribbon. For an indenter load of up to P = 1.5 N, the samples of $Fe_{81.4}$–$Cr_{4.0}$–$Mo_{6.0}$–$Ni_{5.2}$–$C_{1.0}$–$Mn_{2.1}$–$Al_{0.3}$, $Fe_{71.7}$–$Ni_{6.0}$–$Co_{2.4}$–$Cr_{7.5}$–$Mo_{7.9}$–$B_{4.0}$–$Si_{0.5}$, and Fe_{86}–$P_{9.8}$–$C_{1.0}$–$Si_{0.9}$–$Al_{1.7}$–$B_{0.6}$ alloys exhibit only shear bands in the form of half-rings. No shear bands were observed in the form of rays reported in [1, 2]. However, it was found that the number of bands was different at various faces of the indenter marks formed by normal indentation on the ribbon surface (see Fig. 1). The average number of shear bands at the analogous faces was retained from one mark to another to within the experimental uncertainty. These

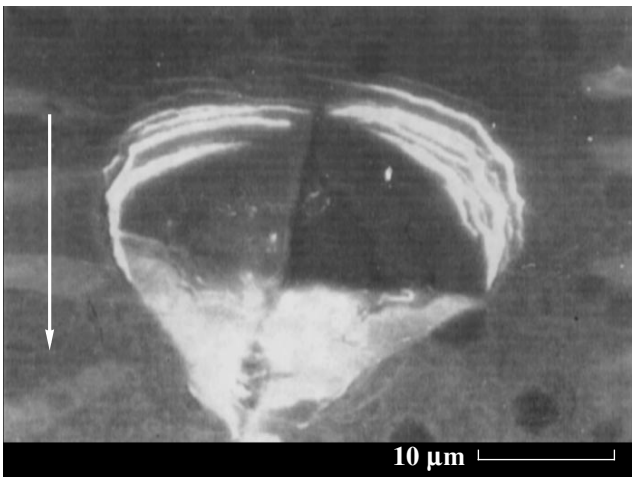

Fig. 1. Scanning electron micrograph showing shear bands at the mark of a Vickers pyramid indenter. The arrow indicates the direction of ribbon casting.

1063-7850/04/3003-0211$26.00 © 2004 MAIK "Nauka/Interperiodica"

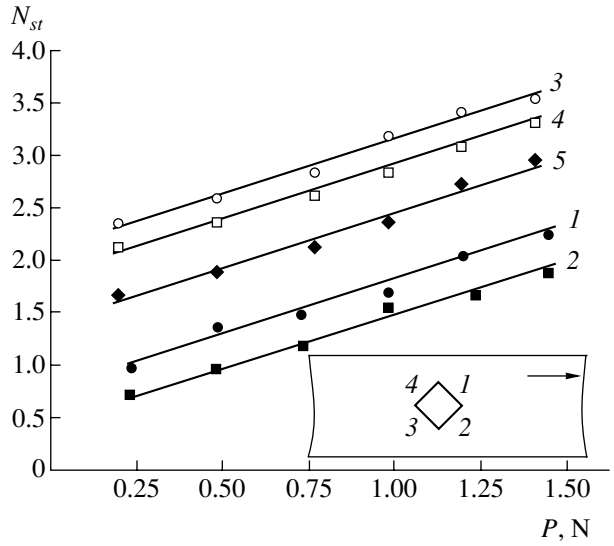

Fig. 2. Plots of the average number N_{st} of shear bands of the half-ring type versus indenter load P for the samples of a $Fe_{81.4}$–$Cr_{4.0}$–$Mo_{6.0}$–$Ni_{5.2}$–$C_{1.0}$–$Mn_{2.1}$–$Al_{0.3}$ alloy: (*1–4*) data for the regions at various faces of the indenter marks indicated in the inset (the arrow shows the ribbon casting direction); (*5*) average values.

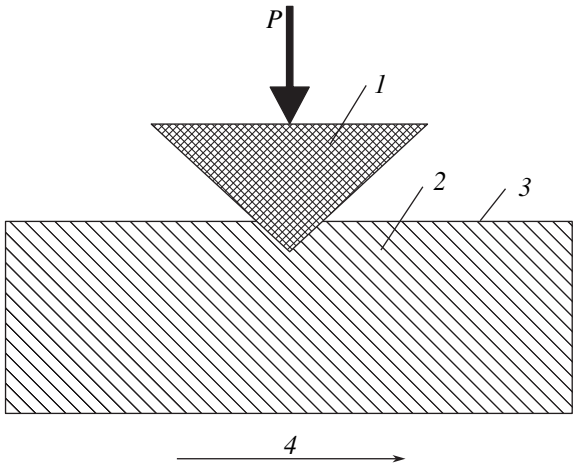

Fig. 3. A schematic diagram of the orientation of shear stresses in amorphous alloy ribbons: (*1*) indenter; (*2*) slip planes; (*3*) amorphous ribbon; (*4*) ribbon casting direction; (*P*) load on indenter.

results are presented in Fig. 2 for $Fe_{81.4}$–$Cr_{4.0}$–$Mo_{6.0}$–$Ni_{5.2}$–$C_{1.0}$–$Mn_{2.1}$–$Al_{0.3}$ alloy.

For the amorphous alloys studied, the plots of $N_{st} = f(P)$ are linear. At a fixed load on the indenter, the maximum number of shear bands was observed for the samples of $Fe_{81.4}$–$Cr_{4.0}$–$Mo_{6.0}$–$Ni_{5.2}$–$C_{1.0}$–$Mn_{2.1}$–$Al_{0.3}$, and the minimum, for Fe_{86}–$P_{9.8}$–$C_{1.0}$–$Si_{0.9}$–$Al_{1.7}$–$B_{0.6}$. This result indicates that most pronounced inhomogeneous plasticity is inherent in the former alloy, which is characterized by a minimum fraction of nonmetallic additives. In the latter alloy, this fraction is maximum. Therefore, the inhomogeneous plasticity of multicomponent iron based amorphous alloys is determined by metallic bonds, while the nonmetallic components favor an increase in the alloy brittleness.

The plots of $N_{st} = f(P)$ for the shear bands at each face of the Vickers indenter are also linear. The numbers of shear bands formed at faces 1 and 2 are smaller than those observed at faces 3 and 4 (Fig. 2). Note that this behavior is observed for the indenter marks with equal diagonals, which shows that the indenter was driven perpendicularly to the surface. Therefore, a factor determining the distribution of shear bands at the indenter faces was the direction of ribbon casting. In this context, we may suggest that somewhat different rates of cooling on the sides of ribbon contacting with the copper disk and air result in the development of internal stresses. The corresponding slip planes are oriented at an angle relative to the ribbon surface, as schematically depicted in Fig. 3. As a result, the stressed state induced by the indenter is such [3] that the direction of shear stress coincides with the direction of slip planes in the amorphous ribbon for some faces and not for the other ones. In the case under consideration, such coincidence is possible only for faces 3 and 4 (see the inset in Fig. 2). At these faces, the process of shear band formation in the form of half-rings is facilitated. Thus, the phenomenon of anisotropic plastic straining in isotropic amorphous alloys is explained by the presence of internal stresses influencing the character of inhomogeneous local plastic deformation.

If the temperatures on the two sides of an amorphous alloy ribbon during rapid quenching are T and T_0, the corresponding strain tensor has the following form:

$$u_{ik} = \frac{\alpha_{ik}}{3}(T - T_0), \tag{1}$$

where α_{ik} is a second-rank tensor symmetric with respect to the indices i, k. According to Prandtl approach [5–7] to the calculation of stresses in a thin plate compressed by uniformly distributed surface forces, the shear stresses in our samples can be calculated using the relation

$$\tau_{xy} = k(H/h), \tag{2}$$

where k is a material constant, H is the sample width, and h is the ribbon thickness.

Thus, using the local surface deformation technique, it was established that inhomogeneous plastic deformation in iron based amorphous alloys develops at different rates in various directions. This is explained by the internal stresses developed in ribbons during their fabrication.

REFERENCES

1. M. N. Vereshchagin, V. G. Shepelevich, O. M. Ostrikov, and S. N. Tsybrankova, Fiz. Met. Metalloved. **93** (5), 101 (2002).
2. M. N. Vereshchagin, V. G. Shepelevich, O. M. Ostrikov, and S. N. Tsybrankova, Kristallografiya **47**, 691 (2002) [Crystallogr. Rep. **47**, 635 (2002)].
3. K. Johnson, *Contact Mechanics* (Cambridge Univ. Press, Cambridge, 1987; Mir, Moscow, 1989).
4. L. D. Landau and E. M. Lifshitz, *Course of Theoretical Physics*, Vol. 7: *Theory of Elasticity* (Nauka, Moscow, 1965; Pergamon, New York, 1986).
5. L. M. Kachanov, *Foundations of the Theory of Plasticity* (Nauka, Moscow, 1969; North-Holland, Amsterdam, 1971).
6. V. V. Sokolovskiĭ, *Theory of Plasticity* (Vysshaya Shkola, Moscow, 1969) [in Russian].
7. V. S. Savenko, V. V. Uglov, O. M. Ostrikov, and A. P. Khodoskin, Fiz. Met. Metalloved. **85** (5), 96 (1998).

Translated by P. Pozdeev

Technical Physics Letters, Vol. 30, No. 3, 2004, pp. 214–216. Translated from Pis'ma v Zhurnal Tekhnicheskoĭ Fiziki, Vol. 30, No. 5, 2004, pp. 88–94.

The Antimicrobial Action of High-Power Electric Discharge in Water. Part 1. Shock Wave Initiation, Evolution, and Structure

K. V. Vilkov and Yu. A. Nagel'

Keldysh Research Center, Federal Unitary Enterprise, Moscow, Russia

e-mail: kerc@elnet.msk.ru

Received March 18, 2003; in final form, September 11, 2003

Abstract—We have studied the initiation, evolution, and structure of shock waves as the main antimicrobial factor of a high-power electric discharge in water. The shock wave structure is studied in a plane one-dimensional approximation using a system of generalized equations of hydrodynamics proposed by Alekseev. Possible mechanisms of the shock-wave-induced degradation of microorganisms are considered. © *2004 MAIK "Nauka/Interperiodica".*

Introduction. The idea of using pulsed electric discharge for water disinfection was originally formulated by Yutkin [1]. However, experimental values of the specific energy consumption for the pulsed discharge disinfection achieved in the 1960s–1970s were rather high (1–10 kWh/m^3, depending on the concentration of microbes), which delayed practical investigations [2]. Recent progress in the field of pulse electronics and the need for reagent-free water disinfection methods revived the interest in Yutkin's ideas. Some new results on the energy efficiency of using periodic pulsed discharges with a pulse energy of 1–20 J were reported in [3–6]. An important feature of such discharges is their multifactor action upon microbes in the region immediately adjacent to the discharge zone. The specific energy consumption has been reduced to 0.5–1.0 kWh/m^3.

In the case of a high-power electric discharge (with an energy of several kJ/pulse), the main antimicrobial factor is the discharge-induced shock wave. This makes possible the degradation of microbes under the action of a single discharge—in contrast to a low-power periodic pulsed discharge, whereby the disinfection is reached as a result of the damage accumulation in microbes. Although the use of high-power discharges increases the level of thermomechanical loads upon structural elements, the specific energy consumption may decrease because the number of discharges can be reduced to one, while the volume of water treated in a single cycle can be increased.

Shock wave initiation, evolution, and structure. The shock waves were studied in a plane one-dimensional approximation assuming instantaneous energy evolution at the cross section $x = 0$ of the half-space $x \geq 0$. The coordinate and time of initiation of a shock wave were determined using the relations [7]

$$t_z = \frac{2c}{(\gamma + 1)a}, \quad x_z = \frac{2c^2}{(\gamma + 1)a}, \tag{1}$$

where c is the sound velocity, γ is the power index in the equation of state, and a is the acceleration at $x = 0$, $t = 0$. Table 1 gives the values of parameters calculated using Eqs. (1) for a pulsed discharge (deposited energy density, 2.95 kJ/cm^2) in comparison to data for some alternative sources of shock waves with comparable values of a [7–9].

The shock wave front structure was calculated using a system of generalized equations of hydrodynamics, including the equations of mass and momentum con-

Table 1. The conditions of shock wave initiation in water by various methods

Parameter	Pulsed electric discharge	Electric explosion of wire	Explosion of condensed substance	Laser pulse action	Plate impact
a, m/s^2	1.6×10^8	10^9	3×10^9	1.2×10^{10}	2.2×10^{11}
t_z, μs	2.3	0.4	0.1	3.2×10^{-2}	1.7×10^{-3}
x_z, nm	3.5	0.6	0.2	4.7×10^{-2}	2.5×10^{-3}

1063-7850/04/3003-0214$26.00

servation [10] and the equation of state for water (in the Tate form):

$$\frac{d\rho v}{dx} - \frac{d}{dx}\tau\frac{d}{dx}[p + \rho v^2] = 0,$$
$$\frac{d(p + \rho v^2)}{dx} - \frac{d}{dx}\tau\frac{d}{dx}[3vp + \rho v^3] = 0, \qquad (2)$$
$$p = B\left[\left(\frac{\rho}{\rho_1}\right)^{\gamma} - 1\right].$$

Here, $B = 3.045 \times 10^8$ Pa, $\gamma = 7.15$, ρ_1 is the density of water under normal conditions, $\tau = r_0/c$, and $r_0 = 3.5 \times 10^{-10}$ m is the average spacing of water molecules. System (2) has to be solved with the boundary conditions representing a discontinuity relation between the values of density and velocity before and behind the shock wave front. Table 2 gives the shock wave front thicknesses $\delta = (\rho_2 - \rho_1)/(d\rho/dx)_{\max}$ calculated for various pressure jumps Δp in the shock wave.

The pattern of the shock wave evolution calculated assuming a = const is plotted in the figure in the dimensionless coordinates of $\tilde{x} = x/(c^2/a)$ versus $\tilde{t} = t/(c/a)$. The shock wave is initiated at a point with the coordinates $\tilde{x} = \tilde{t} = 0.24$. The scaling factors for various methods of the shock wave initiation are given in Table 3. For a pulsed discharge with a deposited energy density of 2.95, 17.7, and 35.4 kJ/cm^2, the maximum pressure jump in the shock waves (see profiles *A*, *B*, and *C* in the figure) is reached at the points with the coordinates (x_A = 3.4 mm, t_A = 3.2 μs), (x_B = 7.0 mm, t_B = 4.3 μs), and (x_C = 9.5 mm, t_C = 5.5 μs), respectively. Thus, despite lower values of a in comparison to those for the other sources, the pulsed discharge provides for quite acceptable spatial and temporal scales of the shock wave initiation and formation (Table 1).

The possible mechanisms of microbe degradation under the action of shock waves. One of the possible factors leading to the loss of microbes is the thermal and/or mechanical damage of the cell structure. For $\Delta p \geq 50$ MPa (Table 2), the shock wave front thickness is much smaller than the characteristic microbe size (1–10 μm). Therefore, the corresponding thermal and mechanical effects can be considered within the framework of a hydrodynamic approach.

The degree of heating as a result of the shock wave passage can be evaluated using the formula [11]

$$T/T_0 = (V/V_0)^{-\Gamma_0}, \qquad (3)$$

where V/V_0 is the change in the specific volume determined from the Tate equation and $\Gamma_0 = \beta/\rho k_m c_v$ is the Grüneisen constant (β is the volume coefficient of thermal expansion, k_m is the isothermal compression coefficient, and c_V is the specific heat capacity). The necessary data are presented in Table 4, where medium 1 is water and medium 2 is an organic fluid typical of microbial cells. According to the estimates obtained using formula (3), the heating of microbes to a temperature above 100°C is possible when the pressure jump at the shock wave front amounts to $\Delta p > 1.7 \times 10^3$ MPa (the temperature of water increases by $\Delta T \cong 10$ K).

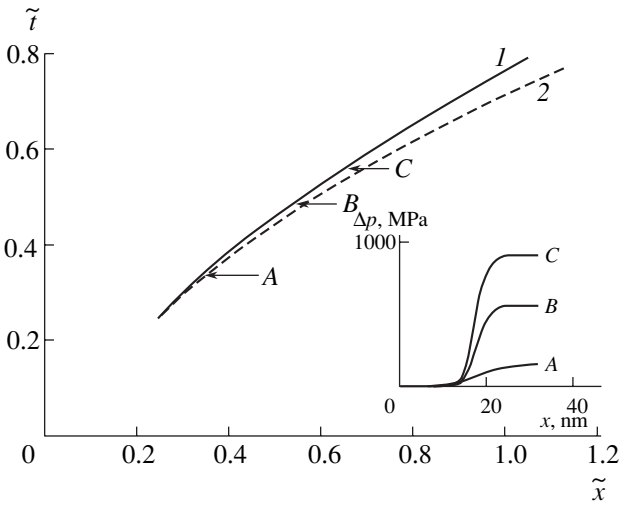

The initiation and evolution of discharge-induced shock waves in water: (*1*) shock wave trajectory; (*2*) envelope of the shock wave characteristics. The inset shows the pressure jump profiles for a deposited energy density of (*A*) 2.95, (*B*) 17.7, and (*C*) 35.4 kJ/cm^2.

For evaluating the mechanical effect, let us consider microbes as spherical species of diameter d and density ρ_0 streamlined by a medium of density ρ and use the condition of their breakage as a result of the Kelvin–Helmholtz instability [12],

$$\Delta p > \rho^{1/2} D\left(\frac{2\pi\sigma}{d}\frac{\rho}{\rho_0}\right)^{1/2}, \qquad (4)$$

where D is the shock wave velocity and σ is the surface tension at the interface. The thickness of a microbe cell wall possessing a polymer structure is typically within

Table 2. Shock wave front thicknesses for various pressure jumps in water

Δp, MPa	δ, nm	Δp, MPa	δ, nm
50	~75	1190	4.54
80	64.4	1670	4.16
100	53.1	2285	3.92
155	37.3	3055	3.74
295	8.46	4015	3.64
515	6.22	5200	3.57

Table 3. Scaling factors for the shock waves initiated in water by various methods

Parameter	Pulsed electric discharge	Electric explosion of wire	Explosion of condensed substance	Laser pulse action	Plate impact
c^2/a, mm	13.9	2.2	0.75	1.9×10^{-1}	10^{-2}
c/a, μs	9.3	1.5	0.5	1.3×10^{-1}	6.9×10^{-3}

Table 4. Parameters determining the shock-wave-induced heating of microbes in water

Medium	k_m, 1/Pa	β, 1/K	c_V, kJ/(kg K)	ρ, kg/m^3	B, Pa	1/γ
1	$(3.5–4.5) \times 10^{-10}$	0.182×10^{-3}	4.18	10^3	3.045×10^8	0.14
2	$(0.5–1.0) \times 10^{-9}$	~10^{-3}	1.0–3.0	7.5×10^2	$(0.7–0.9) \times 10^8$	0.08–0.1

Δ = 10–25 nm. Since the rupture stress σ_r for a liquid is approximately related to the surface tension as $\sigma_r \cong 2\sigma/r_0$ [13], formula (4) can be used for the estimation purposes by replacing σ by $\sigma_* = \sigma_1\Delta/r_0$ or $\sigma_* = \sigma_r\Delta$, where σ_1 and σ_r are the surface tension and rupture stress of the cell wall material. For the typical values of σ_r in polymers ~20 MPa [4], formula (4) yields the estimate $\Delta p > (0.6–1.35) \times 10^2$ MPa.

Conclusions. A high-power electric discharge in water leads to the initiation and formation of a shock wave in the immediate vicinity of the discharge axis: at a distance of 3–5 mm from this axis (for a deposited energy of ~3 kJ/cm^2). At a pressure jump above 50 MPa, the shock wave front thickness is much smaller than the characteristic microbe size and these species can be considered as macroscopic objects. We have considered two possible mechanisms of the shock-wave-induced degradation of microbes. Most likely, the loss of microbes is caused by their breakage as a result of the instability development in the course of streamlining. The necessary pressure jump is evaluated as exceeding $(0.6–1.35) \times 10^2$ MPa. This value can be considered as a necessary condition for microbe degradation upon a single electric discharge in water.

REFERENCES

1. L. A. Yutkin, *Electrohydraulic Effect* (Mashgiz, Moscow, 1955) [in Russian].
2. I. A. Sytin, *Electrohydraulic Action upon Microorganisms* (Zdorov'e, Kiev, 1982) [in Russian].
3. V. L. Goryachev, F. G. Rutberg, and V. N. Fedyukovich, Teplofiz. Vys. Temp. **34**, 757 (1996).
4. V. L. Goryachev, F. G. Rutberg, and V. N. Fedyukovich, Izv. Ross. Akad. Nauk, Énerg. **34**, 40 (1998).
5. A. V. Avchinnikov, A. E. Nedachin, Yu. A. Rakhmanin, *et al.*, Meditsinskaya Konsul'tatsiya, No. 1 (9), 9 (1996).
6. A. V. Avchinnikov, Vestn. Smolensk. Med. Akad., No. 3, 75 (2001).
7. F. A. Baum, L. P. Orlenko, K. P. Stanyukovich, V. P. Chelyshev, and B. I. Shekter, *Physics of Explosion* (Nauka, Moscow, 1975) [in Russian].
8. P. I. Tsarenko, A. R. Rizun, M. V. Zhirnov, *et al.*, *Hydrodynamic and Thermal Characteristics of High-Power Underwater Spark Discharge* (Naukova Dumka, Kiev, 1984) [in Russian].
9. V. A. Yanushkevich, Fiz. Khim. Obrab. Mater., No. 5, 9 (1975).
10. B. V. Alekseev and I. T. Grushin, *Transport Processes in Reactive Gases and Plasmas* (Énergoatomizdat, Moscow, 1994) [in Russian].
11. Ya. B. Zel'dovich and Yu. P. Raizer, *Physics of Shock Waves and High-Temperature Hydrodynamic Phenomena*, 2nd ed. (Nauka, Moscow, 1966; Academic Press, New York, 1967).
12. B. E. Gel'fand, S. A. Gubin, R. I. Nigmatulin, and E. I. Timofeev, Dokl. Akad. Nauk SSSR **233**, 292 (1977) [Sov. Phys. Dokl. **22**, 357 (1977)].
13. J. Frenkel (Ya. I. Frenkel'), *Kinetic Theory of Liquids* (Nauka, Leningrad, 1975; Clarendon Press, Oxford, 1946).
14. *Physical Quantities. Handbook*, Ed. by N. S. Grigor'ev and E. Z. Meĭlikhov (Énergoatomizdat, Moscow, 1991).

Translated by P. Pozdeev

Technical Physics Letters, Vol. 30, No. 3, 2004, pp. 217–219. Translated from Pis'ma v Zhurnal Tekhnicheskoĭ Fiziki, Vol. 30, No. 6, 2004, pp. 1–8.

External Signal Suppresses Automodulation in a Gyro-Backward-Wave Tube Oscillator

A. E. Hramov

State Scientific Center "College," Saratov State University, Saratov, Russia

e-mail: aeh@cas.ssu.runnet.ru

Received July 9, 2003; in final form, September 30, 2003

Abstract—Suppression of the automodulation of the output field in a gyro-backward-wave tube (gyro-BWT) by an external driving harmonic signal is demonstrated for the first time using the results of computer simulation. Parameters of the driving signal for which this phenomenon is possible have been determined. © *2004 MAIK "Nauka/Interperiodica".*

Gyro-backward-wave tubes (gyro-BWTs) characterized by a high output power (up to several dozen megawatts in a millimeter wavelength range) are among promising devices of modern microwave electronics [1]. Another advantage of gyro-BWTs is the possibility of readily controlling the microwave radiation frequency by changing the longitudinal velocity of electrons or by varying the static magnetic field [1, 2]. On the other hand, a significant disadvantage of gyro-BWTs is that an increase in the system length or in the electron beam current gives rise to automodulation of the output signal, whereby the generation spectrum becomes multifrequency [3, 4]. One possible method of solving this problem consists in using distributed power extraction by means of coupled waveguide systems [5, 6].

This Letter proposes an alternative approach to the suppression of automodulation in a gyro-BWT, whereby the distributed "helical electron beam–backward wave" autooscillatory system occurring in the regime of multifrequency oscillations is subjected to the action of an external harmonic signal of a relatively low power. Previously [7, 8], we have thoroughly studied the synchronization of autooscillations in the "helical electron beam–backward wave" system. This study addresses primarily the problem of expanding the region of single-frequency generation in a nonautonomous gyro-BWT.

The system of equations describing the interaction of a helical electron beam with the backward wave includes the equation of motion for electrons in a weakly relativistic helical beam [2, 9] and an equation describing excitation of the backward wave by the electron beam [10]. In a dimensionless form, these equations can be written as follows:

$$\frac{d\beta}{d\xi} - j\mu(1 - |\beta|^2)\beta = F, \qquad (1)$$

$$\frac{\partial F}{\partial \tau} - \frac{\partial F}{\partial \xi} = -\frac{1}{2\pi}\int_0^{2\pi} \beta d\theta_0. \qquad (2)$$

Here, $\beta = r\exp(j\theta)$ is the complex radius of electron trajectories in the ensemble possessing initially homogeneous phase distribution relative to the high-frequency (HF) field; F is the slowly varying complex dimensionless field amplitude in the beam cross section; ξ and τ are the dimensionless longitudinal coordinate and time, respectively; $\mu = (v_\parallel/c)/2\varepsilon$ is the parameter of nonisochronism characterizing the degree of inertia of the system; $v_\parallel$ is the longitudinal velocity of the helical electron beam; and ε is the interaction parameter [2, 3, 7]. Equation (1) has to be solved with the following initial conditions,

$$\beta(\xi = 0) = \exp(j\theta_0), \quad \theta_0 \in [0, 2\pi], \qquad (3)$$

which establish that the helical electron beam is not modulated at the system entrance. An external harmonic driving signal introduced at the collector end of the system is described by the expression

$$F(\xi = A) = F_{\text{inp}}\exp[j\Omega\tau], \qquad (4)$$

where A is the dimensionless length of the system, F_{inp} is the driving signal amplitude, and Ω is the detuning of the external signal frequency from the "cold" synchronism between the backward wave and helical beam. Simplifying assumptions underlying the above model and the expressions for dimensionless variables are considered in detail elsewhere [2, 3, 7].

The control parameters of the model are the system length A and the parameter μ of nonisochronism of the oscillating electrons. In the system with a constant beam current I_0, variation of the parameter A at a constant μ corresponds to a change in the system length l. At a constant length l, A is varied at the expense of current I_0 so that the product μA remains constant.

Let us consider the behavior of a gyro-BWT with the dimensionless length of the interaction space A = 3.0 and variable nonisochronism parameter μ. Self-

1063-7850/04/3003-0217$26.00

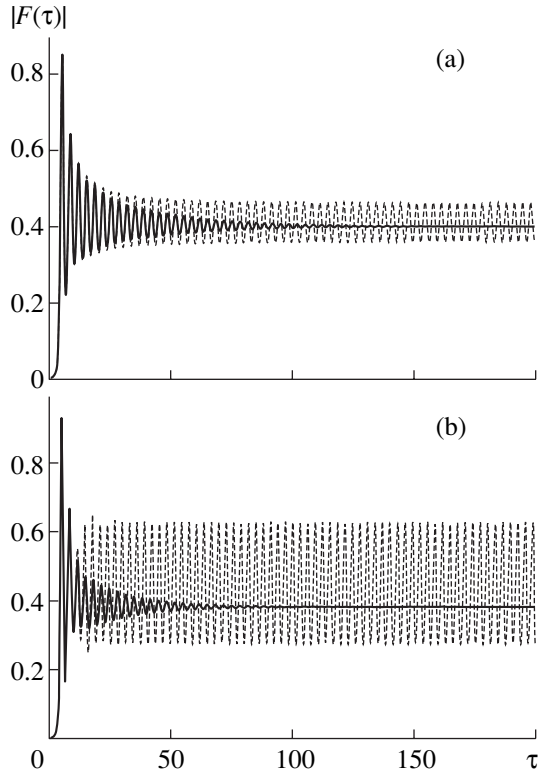

Fig. 1. Time series of the output signal amplitude $|F(\xi = 0, \tau)|$ in a gyro-BWT with a dimensionless length of $A = 3.0$ operating in an autonomous regime with automodulation (dashed curves) and in a nonautonomous regime with the automodulation suppressed by an external driving signal (solid curves): (a) $\mu - \mu_{aut} = 0.02$ ($P_{inp} = 0.004P_0$, $\Omega/\omega_0 = 1.0019$); (b) $\mu - \mu_{aut} = 0.80$ ($P_{inp} = 0.2P_0$, $\Omega/\omega_0 = 1.17$).

excitation of the gyro-BWT is observed for $\mu_{st} \approx 0.73$, whereby a stationary regime of single-frequency generation is established. For $\mu_{aut} \approx 3.78$, the gyro-BWT exhibits automodulation of the output field: the spectrum acquires a multifrequency character, which complicates with further increase in the parameter μ.

The results of numerical simulation showed that an external harmonic signal interacting with autooscillations in a gyro-BWT occurring in the regime of automodulation ($\mu > \mu_{aut}$) allows this modulation of the output signal to be suppressed, after which the system exhibits stationary generation at the frequency Ω of the driving signal (which is only slightly different from the frequency ω_0 of generation in the autonomous regime). The phenomenon of automodulation suppression is illustrated in Fig. 1 showing the time series of the output field amplitude $|F(\xi = 0, \tau)|$ of a gyro-BWT operating in an autonomous regime with automodulation (dashed curve) and in a regime with the automodulation suppressed by the external signal. The calculations were performed for the cases of control parameters slightly ($\mu - \mu_{aut} = 0.02$) and strongly ($\mu - \mu_{aut} = 0.80$) exceeding the level of the automodulation onset. As can be seen from Fig. 1, the action of an external signal with certain parameters (frequency Ω and power $|F_{inp}|^2$) on the gyro-BWT (nonautonomous regime) leads to the attainment (after a certain transient process) of a stationary generation regime characterized by a constant output field amplitude, $|F(\xi = 0, \tau)| = \text{const}$, and a frequency equal to that of the external action Ω (which is close to the autonomous generation frequency ω_0).

The suppression of automodulation in the output signal of a gyro-BWT is observed only in a certain region of parameters of the driving signal. Let us consider this question in more detail. Figure 2a shows the plane of the driving signal parameters (amplitude $|F_{inp}|$ versus normalized frequency Ω/ω_0) and indicates the boundaries of regions in which automodulation of the output field is suppressed and a stationary generation regime is attained for various values of the control parameters A and μ. As is seen, this effect take place for driving signal frequencies greater than that of the autonomous generation frequency ($\Omega > \omega_0$). An increase in the driving signal amplitude leads to expansion of the band of driving frequencies $\Delta\Omega$ featuring the suppression of automodulation of the output field.

As the difference $\mu - \mu_{aut}$ increases at a constant system length A, the stationary generation regime is attained at a higher amplitude $|F_{inp}|$ (and power) of the external driving signal. This is illustrated by Fig. 2b, showing a plot of the minimum driving signal power P_{inp} necessary to suppress automodulation of the output field versus the parameter of nonisochronism μ of oscillating electrons in the helical beam for a constant dimensionless length $A = 3.0$. In the vicinity of a threshold corresponding to the onset of automodulation ($\mu \gtrsim \mu_{aut}$), the driving signal power necessary for its suppression is quite small: $P_{inp} \ll P_0$, where P_0 is the power of generation in the autonomous regime. When the difference $\mu - \mu_{aut}$ increases up to ≈ 1.45, the necessary power level also slowly grows; however, there is a sharp increase in the driving signal power necessary to suppress automodulation of the output field for $\mu > 5.2$.

Figure 2a shows that an increase in the parameter of nonisochronism above the μ_{aut} level leads, besides a growth of the driving signal power necessary to suppress automodulation of the output field, to narrowing of the band of the driving signal frequencies corresponding to stationary generation regimes in the nonautonomous system (cf. the curves in Fig. 2a corresponding to $\mu = 3.8$ and 4.9 for a system with the length $A = 3.0$).

As the system length A increases, the parameter of nonisochronism corresponding to the onset of automodulation in the autonomous system grows as well. However, the suppression of automodulation and the regime of nonautonomous stationary generation are still observed. Figure 2a shows the regions of automodulation suppression constructed for $\mu = 3.0$ and two values of the dimensionless length, $A = 3.5$ and 3.8. As the

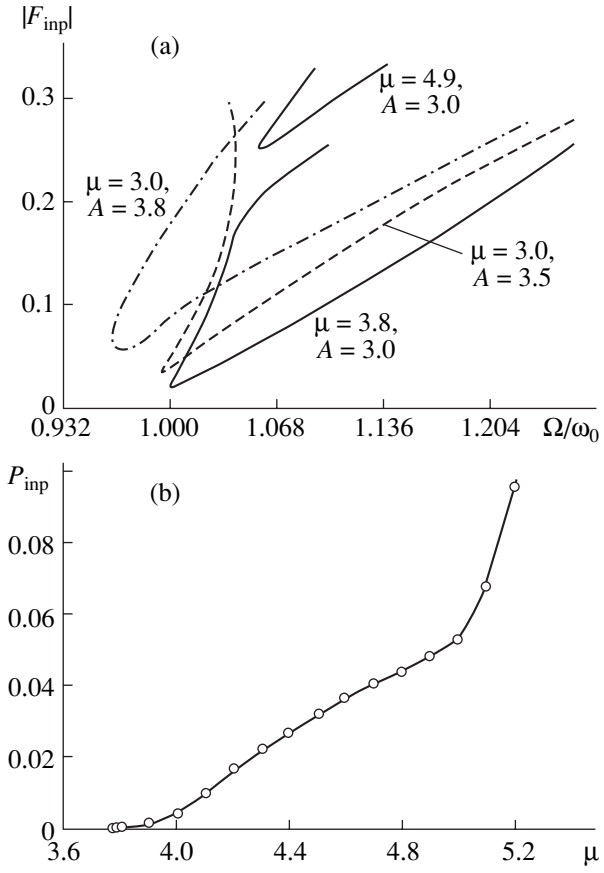

Fig. 2. A nonstationary theory of gyro-BWT illustrated by the results of numerical solution of Eqs. (1)–(4): (a) boundaries of the regions of the plane of the driving signal parameters (amplitude $|F_{inp}|$ versus normalized frequency Ω/ω_0) in which automodulation of the output field is suppressed and stationary generation is attained for various values of the control parameters A and μ; (b) a plot of the minimum driving signal power P_{inp} necessary to suppress automodulation of the output field versus the parameter of nonisochronism μ of oscillating electrons for a system with the dimensionless length $A = 3.0$.

system length increases, the region of nonautonomous stationary generation slightly shifts toward lower driving signal frequencies, while the shape of this region remains virtually unchanged.

Let us briefly consider the physical processes taking place in the system under consideration. The onset of automodulation of the output field is determined by the appearance of an additional distributed feedback in the system [10]: a helical electron beam bunched in a strong field arrives at the collector end of the system ($\xi = A$) in a rebunched state with a velocity of $v_\parallel$; a field excited by the bunched current propagates at a group velocity of v_g back to the system entrance ($\xi = 0$); bunched in a weak field, the beam now excites a strong field in which the helical electron beam is rebunched. As a result, the helical beam is rebunched in a strong HF field along the entire system length; breakage of the phase bunch of oscillating electrons in the helical beam is accompanied by jumps in the phase distribution of the HF field along the transmission line. The driving signal acting upon the system in the synchronization region can break the additional feedback. This is related to the fact that the external signal "forces" the system to acquire a certain phase distribution $\varphi_F(\xi)$ of the HF field in the interaction space. This distribution is characterized by the absence of sharp phase jumps in the space and corresponds to optimum phase relations between the current and field waves with respect to the regime of stationary generation in the gyro-BWT.

Thus, we have demonstrated the possibility of using an external driving signal for suppressing automodulation of the output field arising in a gyro-BWT as a result of an increase in the electron beam current. Conditions (primarily the driving signal parameters) for which this phenomenon is possible have been determined.

Acknowledgments. This study was supported by the Russian Foundation for Basic Research (project no. 02-02-16351).

REFERENCES

1. K. L. Felch, B. G. Danly, H. R. Jory, *et al.*, Proc. IEEE **87**, 752 (1999).
2. A. Yu. Dmitriev, A. E. Konevets, L. A. Pishchik, *et al.*, in *Proceedings of the 7th Winter School on Microwave Electronics and Radiophysics, Saratov, 1981* (Saratovsk. Gos. Univ., Saratov, 1981), Vol. 1, p. 61.
3. A. Yu. Dmitriev, D. I. Trubetskov, and A. P. Chetverikov, Izv. Vyssh. Uchebn. Zaved., Radiofiz. **34**, 595 (1991).
4. G. S. Nusinovich, A. N. Vlasov, and T. M. Antonsen, Phys. Rev. Lett. **87**, 218301 (2001).
5. A. A. Koronovskiĭ and A. E. Khramov, Pis'ma Zh. Tekh. Fiz. **29** (4), 63 (2003) [Tech. Phys. Lett. **29**, 160 (2003)].
6. A. A. Koronovskiĭ, D. I. Trubetskov, and A. E. Khramov, Zh. Tekh. Fiz. **73** (6), 110 (2003) [Tech. Phys. **48**, 768 (2003)].
7. A. A. Koronovskiĭ, D. I. Trubetskov, and A. E. Khramov, Izv. Vyssh. Uchebn. Zaved., Radiofiz. **45**, 773 (2002).
8. D. I. Trubetskov and A. E. Khramov, Izv. Ross. Akad. Nauk, Ser. Fiz. **66**, 1761 (2002).
9. V. K. Yulpatov, Vopr. Radioélektron., Ser. Élektronika, No. 12, 15 (1965).
10. D. I. Trubetskov and A. E. Khramov, *Lectures on Microwave Electronics for Physicists* (Fizmatlit, Moscow, 2003), Vol. 1.

Translated by P. Pozdeev

Technical Physics Letters, Vol. 30, No. 3, 2004, pp. 220–222. Translated from Pis'ma v Zhurnal Tekhnicheskoĭ Fiziki, Vol. 30, No. 6, 2004, pp. 9–15.

Thermodynamics of the Interaction between Impurity Atoms and a System of Quantum Dots

V. V. Svetukhin, S. V. Bulyarskii, and D. V. Sanchishchin*

Ul'yanovsk State University, Ul'yanovsk, Russia

** e-mail: dv_san@sv.uven.ru*

Received June 19, 2003; in final form, September 5, 2003

Abstract—Thermodynamics of the process of dissolution of impurity atoms in a system of quantum dots is analyzed based on minimization of the Gibbs free energy. Criteria for the effective introduction of single impurity atoms into quantum dots are formulated. © *2004 MAIK "Nauka/Interperiodica".*

In recent years, a new approach to obtaining semiconductors with controlled properties has been extensively developed based on the formation of nanodimensional clusters called quantum dots (QDs) [1]. Considerable prospects are offered by the possibility of introducing a single dopant (impurity) atom into a QD. This problem is of importance for optoelectronics and for the development of single-electron devices that can be used in quantum computers [2].

Let us consider thermodynamics of the dissolution of impurity atoms in a system of QDs. The analysis will be based on the method of minimization of the free Gibbs energy developed previously [3–5]. The model system comprises a semiconductor or dielectric matrix containing QDs of the same size with a given concentration of N_{QD}. These QDs are assumed to be stable (and retain their dimensions) in the temperature range studied. Then, impurity atoms capable of dissolving in QDs are introduced by any technological means into the crystal matrix.

Let us assume that the equilibrium occupation of QDs corresponds to a minimum of the Gibbs free energy of the system,

$$G = G_0 + \sum_{m=0} g_m N_m - kT \ln W, \tag{1}$$

where G_0 is the free energy of the crystal matrix with QDs (this quantity is considered as constant) and g_m is a change in the free energy upon the transfer of m impurity atoms from the matrix into QDs (the energies of impurity atoms are measured from the level corresponding to the energy of atoms in the crystal lattice). The last term in Eq. (1) is the configuration entropy of the system under consideration [5].

The number of microscopic states involved in a given macroscopic state is

$$W = \frac{C!}{C_1! \prod_{m=0} (m!)^{N_m} (N - C_1)!} \times \prod_{m=0} \left(\frac{\tilde{N}!}{(\tilde{N} - m)!} \right)^{N_m} \frac{N_{QD}!}{\prod_{m=0} N_m!}, \tag{2}$$

where C is the total impurity concentration in the crystal with QDs, C_1 is the impurity content in the crystal, N_m is the content of QDs with m impurity atoms, N is the number of sites for impurity atoms per unit volume of the crystal matrix, $\tilde{N}$ is the number of sites for impurity atoms in a QD, and N_{QD} is the total number of QDs per unit crystal volume. The first three products in the right-hand part of Eq. (2) determine the number of ways to arrange C atoms in the crystal matrix and QDs. The last product accounts for the statistical identity of QDs with the same number of impurity atoms.

The system under consideration is assumed to be closed and the free energy will be minimized taking into account conservation of the total numbers of impurity atoms and QDs:

$$\varphi_1 = C - C_1 - \sum_{m=0} m N_m = 0, \tag{3}$$

$$\varphi_2 = N_{QD} - \sum_{m=0} N_m = 0. \tag{4}$$

Using the method of Lagrange multipliers, we obtain

the relations

$$C_1 = (N - C_1)\exp\left\{\frac{\lambda_1}{kT}\right\} \approx N\exp\left\{\frac{\lambda_1}{kT}\right\}, \quad (5)$$

$$N_m = \frac{\tilde{N}!}{m!(\tilde{N}-m)!}\exp\left\{-\frac{g_m}{kT}\right\}\exp\left\{\frac{\lambda_1 m}{kT}\right\}\exp\left\{\frac{\lambda_2}{kT}\right\}. \quad (6)$$

In what follows, we use the approximation of $\tilde{N}!/(\tilde{N} - m)! \approx (\tilde{N})^m$.

The number of sites for an impurity atom in a QD is related to the impurity radius as $\tilde{N} = (R/a)^3$, where the parameter a is close to the QD lattice period and is related to the volume per QD lattice site as $v = 4\pi a^3/3$. Using Eqs. (4)–(6), we obtain an expression for the concentration of QDs containing m impurity atoms,

$$N_m = \frac{N_{\mathrm{QD}}}{Zm!}\left(\frac{R}{a}\right)^{3m}\left(\frac{C_1}{N}\right)^m \exp\left\{-\frac{g_m}{kT}\right\}, \quad (7)$$

where

$$Z = \sum_{m=0}\frac{1}{m!}\left(\frac{R}{a}\right)^{3m}\left(\frac{C_1}{N}\right)^m \exp\left\{-\frac{g_m}{kT}\right\}.$$

Assuming that the number of impurity atoms entering into QDs is much smaller than the number of impurity atoms contained in the matrix, we can use the approximation $C \approx C_1$. In the case when impurity atoms occurring in QDs are neutral, a change in the free energy upon the transfer of m atoms X from the matrix (crystal A) to QD (crystal B) can be written as

$$\begin{aligned} g_m &= gm = (h - sT)m \\ &= ((H_{\mathrm{X}}^{\mathrm{A}} - H_{\mathrm{X}}^{\mathrm{B}} + U_{\mathrm{S}}) - (S_{\mathrm{X}}^{\mathrm{A}} - S_{\mathrm{X}}^{\mathrm{B}})T)m, \end{aligned} \quad (8)$$

where $H_{\mathrm{X}}^{\mathrm{A}}$, $H_{\mathrm{X}}^{\mathrm{B}}$ ($S_{\mathrm{X}}^{\mathrm{A}}$, $S_{\mathrm{X}}^{\mathrm{B}}$) are increments in the enthalpy (vibrational entropy) on the passage of atom X from crystal X to crystal A and B, respectively [6]; U_{S} is the energy of interaction of an impurity atom with elastic stresses in a QD.

The change in the vibrational entropy of an impurity atom upon the transfer from crystal A (matrix) to crystal B (QD) can be estimated as [7]

$$S_{\mathrm{X}}^{\mathrm{A}} = 3k\ln\frac{T_{\mathrm{A}}\theta_{\mathrm{X}}}{T_{\mathrm{X}}\theta_{\mathrm{A}}}, \quad S_{\mathrm{X}}^{\mathrm{A}} - S_{\mathrm{X}}^{\mathrm{B}} = 3k\ln\frac{T_{\mathrm{A}}\theta_{\mathrm{B}}}{T_{\mathrm{B}}\theta_{\mathrm{A}}}, \quad (9)$$

where T_{A}, T_{B}, and T_{X} are the melting temperatures and θ_{A}, θ_{B}, and θ_{X} are the Debye temperatures for the crystals A, B, and X, respectively. From the standpoint of practice, it is of interest to consider the case when a single impurity atom resides in a QD. This situation corresponds to $N_1 > N_0$, $N_1 > N_2$. Under these conditions, we can use Eq. (7) and derive the following criterion for a single neutral impurity atom occurring in a QD:

$$1 < \left(\frac{R}{a}\right)^3\left(\frac{C}{N}\right)\exp\left\{-\frac{g}{kT}\right\} < 2. \quad (10)$$

For QDs of small size, condition (10) requires that g be negative (so that the process of impurity transfer from the matrix to a QD will be energetically favorable). Since the interval (10) is relatively narrow, it is rather difficult to realize a situation when only one neutral impurity atom will enter a QD.

However, the situation changes when impurity atoms occurring in QDs are charged. In this case, a QD accommodating one charged impurity atom can exhibit the effect of Coulomb blockade for each subsequent impurity atom. Assuming that the probability for the third impurity atom to enter a QD is small, we obtain

$$\begin{aligned} N_0 &= \frac{N_{\mathrm{QD}}}{Z_{\mathrm{C}}}; \quad N_1 = \frac{N_{\mathrm{QD}}}{Z_{\mathrm{C}}}\left(\frac{R}{a}\right)^3\left(\frac{C}{N}\right)\exp\left\{-\frac{g}{kT}\right\}; \\ N_2 &= \frac{N_{\mathrm{QD}}}{2Z_{\mathrm{C}}}\left(\frac{R}{a}\right)^6\left(\frac{C}{N}\right)^2\exp\left\{-\frac{2g + U_{\mathrm{C}}}{kT}\right\}, \end{aligned} \quad (11)$$

where

$$Z_{\mathrm{C}} = 1 + \left(\frac{R}{a}\right)^3\left(\frac{C}{N}\right)\exp\left\{-\frac{g}{kT}\right\} + \frac{1}{2}\left(\frac{R}{a}\right)^6\left(\frac{C}{N}\right)^2 \times \exp\left\{-\frac{2g + U_{\mathrm{C}}}{kT}\right\},$$

and U_{C} is the energy of Coulomb repulsion between two charged particles in a QD.

The Coulomb blockade of the second impurity atom entering into a QD becomes significant provided that

$$\frac{1}{2}\left(\frac{R}{a}\right)^3\left(\frac{C}{N}\right)\exp\left\{-\frac{g + U_{\mathrm{C}}}{kT}\right\} \ll 1. \quad (12)$$

If condition (12) is valid, the function of QD occupation by single impurity atoms is as follows:

$$f = \frac{N_1}{N_{\mathrm{QD}}} = \frac{\left(\frac{R}{a}\right)^3\left(\frac{C}{N}\right)\exp\left\{-\frac{g}{kT}\right\}}{1 + \left(\frac{R}{a}\right)^3\left(\frac{C}{N}\right)\exp\left\{-\frac{g}{kT}\right\}}. \quad (13)$$

Using this relation, we obtain another criterion, supplementary to (12), for the effective introduction of a sin-

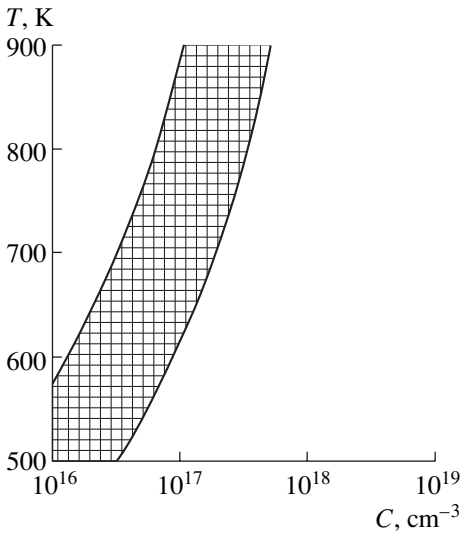

The region of T and C (cross-hatched) ensuring the validity of conditions (12) and (14) for $R/a = 10$.

gle impurity atom into a QD system:

$$\left(\frac{R}{a}\right)^3\left(\frac{C}{N}\right)\exp\left\{-\frac{g}{kT}\right\} \gg 1. \qquad (14)$$

In the last decade, considerable attention has been devoted to the problem of quantum computer and quantum calculations. However, despite extensive theoretical and experimental work, the quantum computer is still not realized. The most promising schemes of this device are based on solid structures, an example being offered by the solid state nuclear magnetic resonance quantum computer [8]. This approach employs a silicon based structure (spin-free silicon isotope ^{28}Si) containing a linear chain of germanium QDs, with an atom of stable isotope ^{31}P possessing a nuclear spin of $I = 1/2$ introduced into the center of each QD. These spins play the role of qubits.

In this context, we have obtained numerical estimates for the intervals of temperature T and the total impurity concentration C obeying conditions (12) and (14) for the system of silicon (matrix) and germanium (QD) doped with phosphorus. The calculations were performed for the following values of the enthalpy of dissolution of phosphorus in silicon and germanium [7]: $H_P^{Si} = 0.73$ eV; $H_P^{Ge} = 0.4$ eV. The change in the entropy upon the transfer of an impurity atom from silicon matrix to germanium QD can be evaluated using relation (9) as $S_P^{Si} - S_P^{Ge} = 0.32k$. The region of T and C ensuring the validity of inequalities (12) and (14) for $R/a = 10$ and $U_C(R) = e^2/(4\pi\varepsilon\varepsilon_0 R)$ is shown in the figure. The calculation was performed in the approximation of small elastic stresses in the QD volume.

Thus, we have demonstrated the possibility of controlling the process of impurity introduction into QDs and determined conditions for the effective doping of QDs with single impurity atoms.

Acknowledgments. This study was supported by the Russian Foundation for Basic Research (project no. 03-01-00206) and the Ministry of Education of the Russian Federation (project no. E02-3.4-537).

REFERENCES

1. A. A. Larionov, L. E. Fedichkin, and K. A. Valiev, Nanotechnology **12**, 536 (2001).
2. M. G. Mil'vidskiĭ and V. V. Chaldyshev, Fiz. Tekh. Poluprovodn. (St. Petersburg) **32**, 513 (1998) [Semiconductors **32**, 457 (1998)].
3. S. V. Bulyarskii and V. P. Oleinikov, Phys. Status Solidi B **141**, K7 (1987).
4. S. V. Bulyarskii and V. I. Fistul', *Thermodynamics and Kinetics of Interacting Defects in Semiconductors* (Nauka, Moscow, 1997).
5. S. V. Bulyarskii and V. V. Svetukhin, *Physics of Controlled Defect Formation in Semiconductors* (Ul'yanovsk. Gos. Univ., Ul'yanovsk, 2002).
6. R. A. Swalin, *Thermodynamics of Solids* (Wiley, New York, 1962; Metallurgiya, Moscow, 1968).
7. K. Weiser, J. Phys. Chem. Solids **7**, 118 (1958).
8. B. E. Kane, Nature **393**, 133 (1998).

Translated by P. Pozdeev

Technical Physics Letters, Vol. 30, No. 3, 2004, pp. 223–224. Translated from Pis'ma v Zhurnal Tekhnicheskoĭ Fiziki, Vol. 30, No. 6, 2004, pp. 16–19.

Optical Confinement of 10-μm Radiation by Silver Chloride Nanoparticles

O. P. Mikheeva and A. I. Sidorov

Institute of Laser Physics, St. Petersburg, Russia

Received July 23, 2003

Abstract—The results of experiments on the nonlinear optical confinement of microsecond pulses of CO_2 laser radiation in a composite material comprising a potassium iodide matrix containing dispersed silver chloride nanoparticles coated by an island film of metallic silver are presented. The energy threshold for the laser radiation confinement is 15 mJ/cm^2 and the dynamic range of confinement amounts to 10^3. © *2004 MAIK "Nauka/Interperiodica".*

Devices capable of nonlinear optical confinement (radiation limiters) are of importance as a means of protection of the human eye and photodetectors from radiation damage (see, e.g., [1]). In the middle IR range, the optical confinement effect can be achieved using silver halide nanoparticles obtained via melting and crystallization of an initial material under illumination with visible light [2–4]. This treatment leads to a partial photolysis of silver halide, with the formation of metal silver particles in the form of an island film on the surface of crystalline silver halide grains. [4] Nanoparticles comprising a dielectric core with a shell of metal island film exhibit plasmon resonances in the middle IR range, which lead to a local amplification of the electromagnetic wave field and to an increase in the effective optical nonlinearity of nanoparticles [4].

In the case of a nonlinear medium obtained by the aforementioned method, it is possible to control neither the content of nanoparticles possessing required optical properties nor the nonlinear optical characteristics of the medium. A more promising technology is offered by the introduction of a desired content of nanoparticles with nonlinear optical properties into a transparent medium possessing linear properties. Below, we describe a composite material comprising a transparent matrix of potassium iodide with dispersed silver chloride nanoparticles coated by an island film of metallic silver. We have studied the nonlinear optical properties of such nanoparticles in the region of 10.6 μm and determined the influence of their content on the characteristics of optical confinement of the composite material.

The samples were prepared as follows. The initial material was a mixture of silver chloride (AgCl) and potassium iodide (KI). The volume fraction of AgCl in KI was varied from 1 to 5%. The mixture was thermally treated—heated to the melting point of AgCl (460°C) and cooled—under illumination with visible light. Subsequent examination of the product in an electron microscope showed that AgCl nanoparticles formed as a result of this treatment have the shape of slightly elongated ellipsoids with an average size of 200–300 nm. The obtained powder was repeatedly triturated and used for pressing tablets with a diameter of 8 mm and a thickness of 1 mm. The linear transmission coefficient

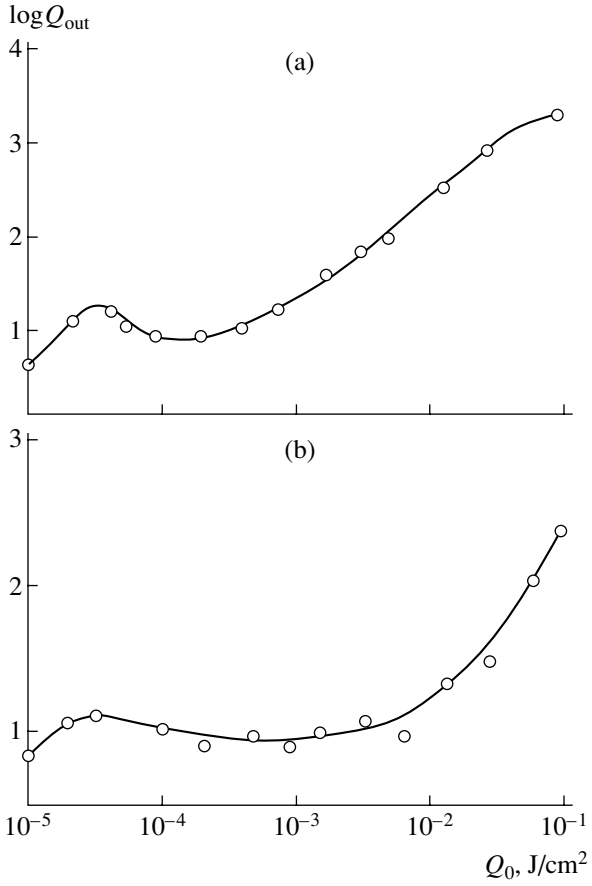

Pulsed laser radiation confinement (λ = 10.6 μm, τ = 1.5 μs) by a composite material comprising a KI matrix containing dispersed AgCl nanoparticles at a volume fraction of f = 1 (a) and 5% (b).

1063-7850/04/3003-0223$26.00 © 2004 MAIK "Nauka/Interperiodica"

of samples measured using low-intensity incident radiation at a wavelength of 10.6 μm was 60%.

The experiments on the optical confinement were performed using a pulsed TEA-CO_2 laser operating at a wavelength of λ = 10.6 μm and a pulse width of τ = 1.5 μs. Semilogarithmic plots of the output (Q_{out}) versus input (Q_0) radiation energy density for the samples with the AgCl volume fraction of f = 1 and 5% are presented in the figure. As can be seen, the energy threshold of confinement in the former case is 25 μJ/cm^2 and the dynamic range of confinement is about 50. As the content of AgCl nanoparticles grows to 5%, the confinement threshold decreases to 15 μJ/cm^2, while the dynamic range increases to 10^3. The radiation breakage threshold exceeds 3 J/cm^2.

The phenomenon of confinement is related to a spectral shift and an increase in amplitude of the plasmon resonance bands, which is caused by the piezooptical effect in the core of nanoparticles [4]. This process is accompanied by an increase in the absorption and scattering cross sections of the nanoparticles. A minimum in the confinement curves corresponds to coincidence of the plasmon resonance peak position with the incident radiation wavelength. The confinement ceases when the plasmon resonance band moves completely away from the radiation wavelength.

The decrease in the energy threshold with increasing content of AgCl nanoparticles is related to the fact that the extinction coefficient of the medium with nanoparticles increases with their content, while the transmitted radiation energy exhibits an exponential dependence on the extinction coefficient. For this reason, the optical nonlinearity is weakly pronounced in the initial stage (small Q_0) and more significantly influences the transmission in the presence of a greater amount of nanoparticles.

The increase in the dynamic range of optical confinement with increasing content of nanoparticles is explained by features in the dynamics of radiation pulses propagating through a thick optically nonlinear medium. At a greater content of nanoparticles, radiation exhibits multiple scattering in the medium and, hence, the layers of medium closer to the output exhibit optical nonlinearity under the conditions of a higher intensity of the incident radiation.

Thus, the proposed method of preparation of a composite medium with dispersed silver halide nanoparticles possessing nonlinear optical properties allows both the energy threshold and the dynamic range of confinement to be controlled.

REFERENCES

1. J. D. Swaleu and F. Kajzar, Nonlinear Opt. B **27** (1–4), 13 (2000).
2. O. P. Mikheeva and A. I. Sidorov, Pis'ma Zh. Tekh. Fiz. **27** (18), 50 (2001) [Tech. Phys. Lett. **27**, 779 (2001)].
3. I. V. Bagrov, A. P. Zhevlakov, O. P. Mikheeva, *et al.*, Pis'ma Zh. Tekh. Fiz. **28** (13), 40 (2002) [Tech. Phys. Lett. **28**, 552 (2002)].
4. A. I. Sidorov, Opt. Zh. **70** (2), 9 (2003).

Translated by P. Pozdeev

Technical Physics Letters, Vol. 30, No. 3, 2004, pp. 225–227. Translated from Pis'ma v Zhurnal Tekhnicheskoĭ Fiziki, Vol. 30, No. 6, 2004, pp. 20–24.

Stochastic Properties of a System of Point Vortices

V. Ya. Rudyak*, E. G. Bord, and D. F. Kranchev

Novosibirsk State Architecture-Building University, Novosibirsk, Russia

** e-mail: rudyak@ngasu.nsk.su*

Received August 7, 2003

Abstract—The dynamic and stochastic properties of a system of point vortices occurring at the vertices of a regular *N*-gon have been investigated. The time of reversibility of the phase trajectories was determined and their stability was studied. It is established that such a system exhibits stochastic properties only in the presence of a local instability, which is possible for $N \geq 8$. © *2004 MAIK "Nauka/Interperiodica"*.

A system of point vortices is one of the key models in classical hydrodynamics. Although the properties of this model have been thoroughly studied for more than a century, the results are rather few. It was shown (see [1, 2] and references therein) that even a system of only four point vortices in the general case is nonintegrable and exhibits stochastic properties. In the context of these investigations, the stochasticity of such four-vortex systems is related to nonintegrability of the corresponding system of the equations of motion. On the other hand, it is clear from the general considerations that stochastic properties of a dynamical system in the general case are independent of the integrability. It would therefore be important to study the dynamical and stochastic properties of the systems of point vortices and establish the conditions under which stochasticity arises. This was the aim of our study.

The dynamics of a system of *N* point vortices on a plane is described by the following system of equations:

$$\frac{d\mathbf{r}_i}{dt} = -\sum_{j \neq i}^{N} \frac{\Gamma_i \lfloor \mathbf{k} \times (\mathbf{r}_i - \mathbf{r}_j) \rfloor}{2\pi r_{ji}^2}, \qquad (1)$$

where $\mathbf{r}_i = x_i, y_i$ are the coordinates of the *i*th vortex, $\mathbf{k}$ is the unit vector perpendicular to the (x_i, y_i) plane, and $\mathbf{r}_{ij} = \mathbf{r}_i - \mathbf{r}_j$. A solution to Eqs. (1) can be constructed for some simple situations. In particular, the solution is known for a system comprising an arbitrary number *N* of vortices with equal intensities Γ occurring at the vertices of a regular polygon. This configuration rotates at a constant angular velocity $\Omega_N = 2\pi\Gamma(N-1)(8\pi^2R^2)$, where *R* is the radius of the circumscribed circle [3, 4]. Introducing the complex coordinate $z_n = x_n + iy_n$ of the vortex on the (x_i, y_i) plane, the corresponding solution for the coordinate of the *N*th vortex can be written as $z_n(t) = R\exp[2\pi i(n-1)/N + \Omega_N t]$.

This study is devoted to the dynamic and stochastic properties of the above configuration of vortices, the number of which was varied from 2 to 10^3. During computer simulation, the dynamic trajectories of the system permanently exhibit perturbations as a result of rounding errors and the use of particular schemes for integration of the equations of motion (1). For unstable solutions, even small errors rapidly become observable.

The equations of motion (1) are reversible with respect to time. This implies, in particular, that the phase trajectories of the system are invariant for the transformation of time reversal. The first problem to be considered in this Letter is determination of the reversibility time T_r of computer-simulated phase trajectories of the system. The T_r value was determined as the maximum time of motion along a given phase trajectory, for which it is possible to return to the ε vicinity of the initial position (in our calculations $\varepsilon = 10^{-4}$) upon time reversal.

As expected, the computer-simulated phase trajectories quite rapidly become irreversible. The reversibility time $T_r = t/T_N$ is inversely proportional to the number of vortices *N*: $T_r \sim 1/N$ (see table). This implies, in particular, that the main factor determining irreversibility is the interaction between vortices. The time of irreversibility significantly depends on the stability of the system. If the system is unstable, the initial perturbation tends to increase and the phase trajectories fail to be

Dependence of the reversibility time T_r on the number of vortices

N	7	8	10	20	40	60	80	100
T_r	3760	6.7012	3.6441	1.3363	1.3363	0.3901	0.2867	0.2259

1063-7850/04/3003-0225$26.00 © 2004 MAIK "Nauka/Interperiodica"

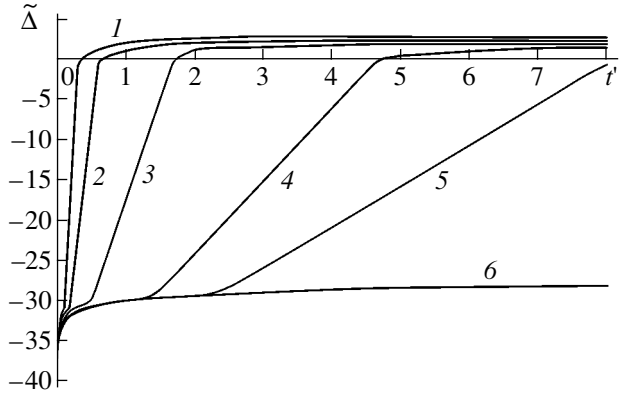

Fig. 1. Evolution of the solution perturbation with time for $N = 100$ (*1*), 50 (*2*), 20 (*3*), 10 (*4*), 8 (*5*), and 7 (*6*).

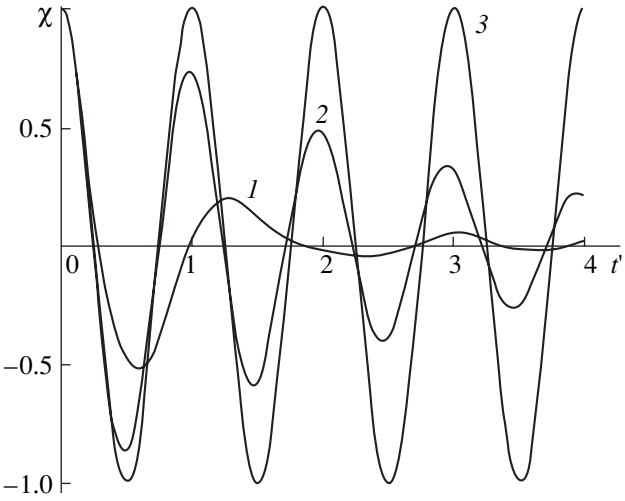

Fig. 2. Autocorrelation functions of the coordinates of point vortices for $N = 100$ (*1*), 10 (*2*), and 7 (*3*).

reversible quite rapidly (see table). The systems under consideration are stable for $N \le 7$ [5], which implies that T_r for $N > 7$ is much shorter than that for $N \le 7$.

The appearance of dynamic chaos is possible in the presence of local instability in the system [6]. The character of stability of trajectories for the given vortex system in the configuration space was determined by studying evolution of the function

$$\Delta(t) = \frac{1}{NlR}\sum_{\alpha=1}^{1}\left\{\sum_{i=1}^{N}[\mathbf{r}_i(t) - \mathbf{r}_i^{c\alpha}(t)]^2\right\}^{1/2}, \qquad (2)$$

where $\mathbf{r}_i$ is the exact solution for the ith vortex and $\mathbf{r}_i^{c\alpha}$ is a numerical solution obtained on the αth step. Thus, the functions Δ were calculated by averaging over an ensemble obtained by variation of the integration step (typically, $l = 7$–10).

Figure 1 shows the typical time variation of the function $\tilde{\Delta} = \ln\Delta$ for systems with various numbers of vortices $N = 100$ (curve *1*), 50 (*2*), 20 (*3*), 10 (*4*), 8 (*5*), and 7 (*6*). The current time t' is measured in the units of T_N. For the first four systems, the curves can be divided into four characteristic regions. The first region, where the function $\tilde{\Delta}$ obeys a power law, is followed by an exponential portion and a transient nonlinear portion corresponding to the development of perturbations, after which function (2) attains a certain almost constant level.

The presence of the exponential portion in the development of perturbations shows that systems with the number of vortices up to $N = 8$ exhibit local instability. The instability increments are proportional to the vortex circulation Δ and inversely proportional to the square of radius R. Exponential expansion of the trajectories takes place until a certain time t_n, which virtually coincides with the reversibility time of the given system (see table). On the other hand, the function $\tilde{\Delta}$ for $N = 7$ first slightly increases and then remains virtually constant. This implies that the given system is stable according to Lyapunov, in good agreement with the stability observed for the given flow in the case of $N \le 7$ [5].

The presence of local instability is evidence of the possible development of dynamic chaos in a system. However, this also requires that the system feature mixing, which is defined as the damping of correlations of two dynamic variables (see, e.g., [6]).

The typical behavior of a normalized autocorrelation function of the vortex coordinates, $\chi(t, 0) = \chi_{xx}(t, 0)/\chi_{xx}(0, 0)$, where

$$\chi_{xx}(t, 0) = \frac{1}{Nl}j = 1\sum_{j=1}^{l-1}\left\{\sum_{i=1}^{N}[x_i(j\Delta t)x_i(j\Delta t + t)]\right\},$$

and l is the number of realizations, is presented in Fig. 2 for systems with $N = 100$ (curve *1*), 10 (*2*), and 7 (*3*). The correlation functions are decaying in the systems with $N \ge 8$, the relaxation time being on the order of the inverse increment of the local instability. However, the decay is not exactly exponential and exhibits a quasiperiodic character related to specific features of the problem under consideration. The period of decaying maxima of the autocorrelation function is on the order of T_N. For a stable vortex configuration with $N = 7$, the correlation function is periodic and exhibits no decay.

Thus, the systems under consideration with the number of vortices $N \ge 8$ actually exhibit dynamic chaos. It should be noted that the obtained characteristics are inherent in the initial Hamiltonian system and do not depend on the computer realization of calcula-

tions. This is confirmed, in particular, by the results of calculations with controlled perturbations. For a small value of the perturbation amplitude, $A \le 10^{-6}$, the instability increments virtually coincide with those for uncontrolled perturbations at any N. However, the increments of finite perturbations are functions of the amplitude.

Acknowledgments. This study was supported by the Russian Foundation for Basic Research (project no. 01-01-00045) and by the Presidential Program of Support of Leading Scientific Schools (project no. NSh-964.2003.1).

REFERENCES

1. H. Aref, Annu. Rev. Fluid Mech. **15**, 345 (1983).
2. W. M. Oliva, Ann. Inst. Henri Poincaré **55**, 707 (1991).
3. Lord Kelvin (W. Thomson), *Floating Magnets (Illustrating Vortex Systems)*, in *The Collected Works* (1978), Vol. 4, pp. 135–140.
4. J. J. Thompson, *A Treatise on the Motion of Vortex Rings* (Macmillan, New York, 1883), p. 94.
5. T. H. Havelock, Philos. Mag. **11**, 617 (1931).
6. G. M. Zaslavskiĭ, *Stochasticity of Dynamical Systems* (Nauka, Moscow, 1984) [in Russian].

Translated by P. Pozdeev

Technical Physics Letters, Vol. 30, No. 3, 2004, pp. 228–230. Translated from Pis'ma v Zhurnal Tekhnicheskoĭ Fiziki, Vol. 30, No. 6, 2004, pp. 25–30.

Evaluating Mechanical Stresses in Thin-Film Structures with Ferroelectric PZT Films

I. P. Pronin[a], E. Yu. Kaptelov[a], N. G. Khosina[b], and V. P. Afanas'ev[a]

[a] *Ioffe Physicotechnical Institute, Russian Academy of Sciences, St. Petersburg, 194021 Russia*

[b] *St. Petersburg State Electrotechnical University, St. Petersburg, Russia*

e-mail: petrovich@mail.ioffe.ru

Received July 31, 2003

Abstract—A model of mechanical stresses acting upon a ferroelectric film in a thin-film capacitor structure of the Si–SiO_2–Pt–PZT–Pt type is proposed. An analysis of this model showed that, in most cases, thin PZT films with thicknesses within 100–200 nm (used in the elements of NVFRAM devices) are subjected to tensile stresses. It is suggested that replacing tensile stresses by compressive stresses in PZT films would increase the stability of operation of memory devices. © *2004 MAIK "Nauka/Interperiodica".*

In the last decade, thin ferroelectric films of the $Pb(Zr_{1-x}Ti_x)O_3$ (PZT) system have found increasing use in microelectronics for the creation nonvolatile memory (NVFRAM) devices with high-density data recording [1–3]. In order to develop a large-scale production of such devices, it is necessary to solve the problem of degradation of their physical parameters. This degradation is usually related to the structural disorder (foreign phase inclusions, diffusion-induced flaws, electric defects, etc.) and crystal imperfection (growth orientation, texturing, grain size and its distribution) of the ferroelectric layer [4–6].

In selecting the optimum composition of a ferroelectric film, its orientation, and the relative thicknesses of layers (PZT, electrodes, and others), the influence of mechanical stresses is usually ignored. However, these stresses can reach a significant level [7] and may strongly influence the degradation of thin-film ferroelectric capacitors [8]. Unfortunately, experimental data on the role of mechanical stresses in thin polycrystalline PZT layers are almost absent. The aim of this study was to estimate the compressive and tensile stresses in thin (100- to 200-nm-thick) PZT films in a multilayer thin-film system of the SiO_2–Pt–PZT–Pt type formed on a silicon substrate.

For the analysis, we assumed that mechanical stresses mostly arise due to the difference in the temperature coefficients of linear expansion of the film and substrate [7–9]. This implies that we will consider ferroelectric layers possessing a fine-grained structure, which are most frequently obtained by depositing PZT onto silicon substrates. In this case, no mechanical stresses are developed at a temperature of deposition or crystallization and the possible deformations related to the crystal lattice mismatch exhibit relaxation at the grain boundaries and, hence, can be considered as insignificant.

Under these conditions, mechanical stresses can be determined using the well-known formula [10]

$$\sigma = \frac{E_f}{1-\nu_f}\int_{T_{anneal}}^{T_0}(\alpha_f - \alpha_s)dT, \qquad (1)$$

where α_f and α_s are the linear expansion coefficients of the film and substrate, respectively; E_f is the Young modulus; ν_f is the Poisson ratio; T_{anneal} is the film crystallization temperature; and T_0 is the temperature of measurements used in the calculations of mechanical stresses. In calculations, we used published data on the temperature coefficients of linear expansion for bulk polycrystalline PZT of various compositions [11]. In this way, we calculated mechanical stresses for a simplified Si–PZT system with the ferroelectric film thickness significantly greater than the total thickness of the lower electrode, SiO_2 film, and other layers in the multilayer structure. This provided for a satisfactory description of the experimental temperature dependences $\sigma(T)$ [9] for PZT films with various Zr/Ti ratios [8] (Fig. 1a). As can be seen in Fig. 1a, the character of mechanical action of the silicon substrate ($\alpha = 2.8 \times 10^{-6}$ K^{-1}) on the ferroelectric layer strongly depends on the PZT film composition. As the content of Zr in the solid solution increases, the character of mechanical stresses changes from compressive to tensile.

A different situation is observed in multilayer thin-film structures of the Si–SiO_2–Pt–PZT–Pt type for NVFRAM devices, where the thickness of textured ferroelectric films (100–200 nm) is comparable with the thicknesses of electrodes (usually made of platinum) and SiO_2 layers. In these structures, the Pt and SiO_2 layers significantly influence the sign and magnitude of mechanical stresses in PZT and, hence, the polarization orientation and the domain structure in this layer. Rela-

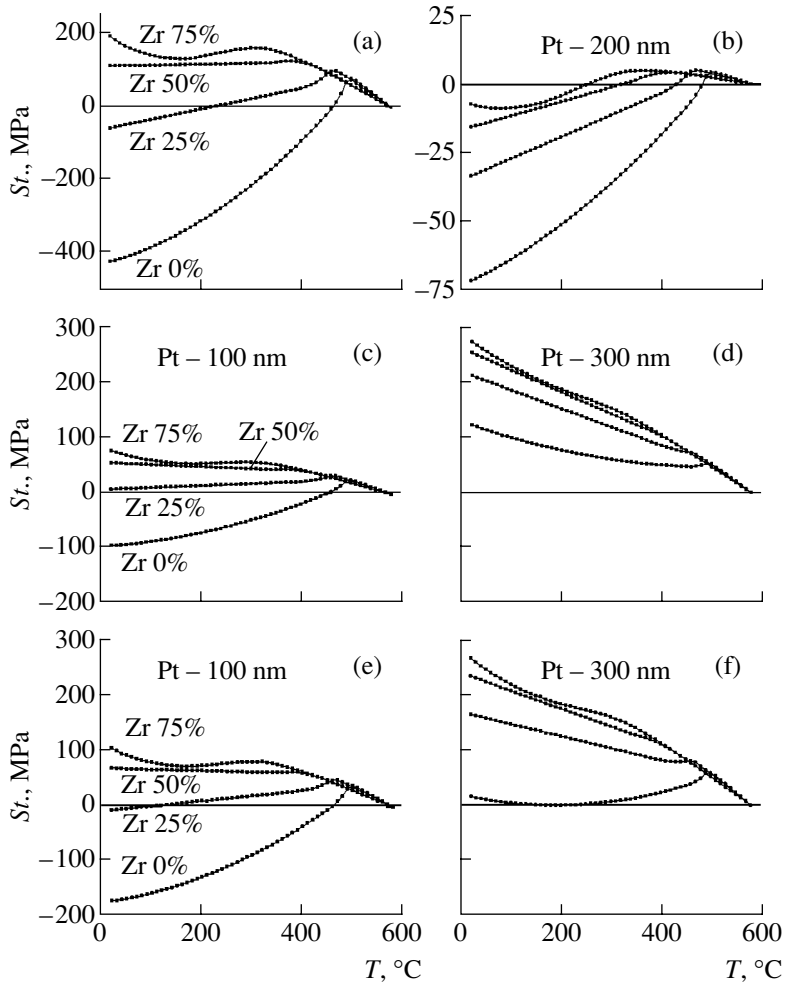

Fig. 1. The results of calculations of the mechanical stresses acting upon thin $Pb(Zr_{1-x}Ti_x)O_3$ (PZT) films in (a) Si–PZT and (b) Si–SiO_2–Pt–PZT–Pt structures with SiO_2 layer thicknesses of (b) 1000 nm and (c–f) 300 nm.

tively low (in comparison to PZT) values of α for SiO_2 ($\alpha = 0.55 \times 10^{-6}$ K^{-1}) lead to an additional compression of the ferroelectric film from the side of SiO_2. On the contrary, Pt electrodes possessing one order of magnitude greater ($\alpha = 10 \times 10^{-6}$ K^{-1}) temperature coefficients of linear expansion produce a tensile action. The resulting additional action upon the PZT layer will be determined by the competition of the effects of SiO_2 and Pt films, being dependent on their relative thicknesses.

Iijima *et al.* [12] showed that compressive stresses acting upon a ⟨100⟩-oriented film of lead titanate produce reorientation of the spontaneous polarization toward the direction normal to the substrate, in which only a 180° domain structure can exist. This mutual orientation of the film and the domain structure is most favorable for memory devices because application of an electric pulse of relatively small amplitude (the coercive field for switching 180° domains is usually lower than that for 90° domains) will switch the maximum possible charge and the hysteresis loop will acquire a shape close to rectangular. An analogous situation is observed in tetragonal PZT films occurring in a compressed state. In addition, we may expect that the degradation characteristics, such as fatigue and aging, of these films with a 180° domain structure will be also on a minimum level. In this case, the optimum PZT compositions are determined by a minimum level of coercive fields, which is typical of solid solutions in the phase diagram region adjacent to the morphotropic phase boundary [13].

From the practical standpoint, most interesting are the rhombohedral PZT films (with a high Zr content), in which the spontaneous polarization is oriented in the ⟨111⟩ direction. This is related to the fact that PZT layers grown on silicon substrates usually repeat the ⟨111⟩ orientation of the lower Pt electrode. As a result, the spontaneous polarization of such films in the compressed state will also be oriented perpendicularly to the substrate. The formation of such films under the conditions of compressive stresses is problematic because the deposits in most cases are subjected to tensile stresses (see Fig. 1a).

In order to calculate the temperature dependences of mechanical stresses acting upon thin (100- to 200-nm-thick) ferroelectric layers in multilayer thin-film structures of the Si–SiO_2–Pt–PZT–Pt type, the temperature coefficient of linear expansion α_{fm} of the SiO_2–Pt–PZT–Pt system with allowance of the component layer thicknesses was expressed as follows:

$$\alpha_{fm} = \frac{\alpha_{PZT}d_{PZT} + \alpha_{Pt}d_{Pt} + \alpha_{SiO_2}d_{SiO_2}}{d_{PZT} + d_{Pt} + d_{SiO_2}}. \quad (2)$$

Analogous expressions were used to calculate the Young moduli and the Poisson ratios to be substituted into Eq. (1).

The calculations were performed for a SiO_2 layer thickness of 300 nm, the total thickness of Pt electrodes varied from 100 to 300 nm, and a PZT layer thickness of 200 nm (Figs. 1c and 1d) and 100 nm (Figs. 1e and 1f). The temperature of formation of the perovskite phase in PZT films was taken equal to 580°C [12]. As can be seen from Fig. 1, the ferroelectric films of both tetragonal and rhombohedral PZT compositions (except for those close to lead titanate) for all standard thicknesses of layers in the structure under consideration occur under the action of tensile stresses, which is undesirable for memory devices. A decrease in the ferroelectric layer thickness and an increase in the thickness of electrodes leads to a growth of tensile stresses.

A way out of this situation can be provided by using thicker layers of silicon dioxide. For example, the results of calculations for a 1000-nm-thick SiO_2 layer (with 200 nm Pt and 100 nm PZT layers) show (Fig. 1b) that PZT films (including rhombohedral compositions) occur in a compressed state. For verification of these theoretical results, it would be expedient to perform experiments with PZT films of various compositions and thicknesses formed on silicon substrates with "thick" SiO_2 layers and compare the stabilities of such thin-film structures.

An analysis of the proposed model and the obtained estimates of the influence of mechanical stresses on the properties of PZT films indicate that it is actually possible to form structures with only 180° domains at the expense of increasing the SiO_2 layer thickness. This would allow PZT films to be obtained possessing rectangular hysteresis loops, minimum switching fields, and increased stability with respect to fatigue and aging. Such films can be successfully used in the elements for NVFRAM devices.

Acknowledgments. This study was supported by the Russian Foundation for Basic Research (project no. 01-02-17799) and the Ministry of Education of the Russian Federation (project no. E02-3.4-489).

REFERENCES

1. J. F. Scott and C. A. Paz de Araujo, Science **246**, 1400 (1989).
2. J. F. Scott, Ferroelectr. Rev. **1**, 1 (1998).
3. S.-H. Kim, C. Y. Koo, S.-M. Ha, *et al.*, Integr. Ferroelectr. **48**, 139 (2002).
4. R. Ramesh, W. K. Chan, B. Wilkens, *et al.*, Integr. Ferroelectr. **1**, 1 (1992).
5. O. Auciello, Integr. Ferroelectr. **15**, 211 (1997).
6. I. P. Pronin, E. Yu. Kaptelov, E. A. Tarakanov, *et al.*, Integr. Ferroelectr. **49**, 285 (2002).
7. G. A. C. M. Spierings, G. J. M. Dormans, W. G. J. Moors, *et al.*, J. Appl. Phys. **78**, 1926 (1995).
8. I. P. Pronin, A. V. Gol'tsev, E. Yu. Kaptelov, and V. P. Afanas'ev, Fiz. Tverd. Tela (St. Petersburg) **45**, 1685 (2003) [Phys. Solid State **45**, 1768 (2003)].
9. R. Bruchhaus, D. Pitzer, M. Schreiter, *et al.*, J. Electroceram. **3**, 151 (1999).
10. J. A. Thornton and D. W. Hoffman, Thin Solid Films **171**, 5 (1989).
11. B. G. Shirane, K. Suzuki, and A. Takeda, J. Phys. Soc. Jpn. **7**, 12 (1952).
12. K. Iijima, Y. Tomita, R. Takayama, *et al.*, J. Appl. Phys. **60**, 361 (1986).
13. Z.-J. Wang, I. Karibe, L. J. Yan, *et al.*, Jpn. J. Appl. Phys. **41**, 6658 (2002).

Translated by P. Pozdeev

Technical Physics Letters, Vol. 30, No. 3, 2004, pp. 231–233. Translated from Pis'ma v Zhurnal Tekhnicheskoĭ Fiziki, Vol. 30, No. 6, 2004, pp. 31–37.

Experimental Study of the Wave Flow of a Liquid Film on a Heated Surface

D. V. Zaĭtsev*, E. A. Chinnov, O. A. Kabov, and I. V. Marchuk

Institute of Thermophysics, Siberian Division, Russian Academy of Sciences, Novosibirsk, Russia

** e-mail: zaitsev@itp.nsc.ru*

Received August 25, 2003

Abstract—The wave flow of a water film over the surface of a vertical plate with a 150 × 150-mm heater has been experimentally studied. The action of heat flux on the wave flow of the liquid film is manifested by the formation of periodic flowing rivulets separated by thin film regions. The thickness of the film between rivulets was measured using a fiber optical reflection probe. As the heat flux grows, the average film thickness h continuously decreases. However, when the thickness reaches $h \approx 0.5h_0$, where h_0 is the value given by the Nusselt formula for a laminar liquid film, the film exhibits spontaneous rupture. It was found that, as the local flow rate decreases, the wave amplitude in the region between rivulets drops more rapidly than expected according to the laws of "cold hydrodynamics." *© 2004 MAIK "Nauka/Interperiodica".*

In recent decades, the wave flow of liquid films has been extensively studied by experimental and theoretical methods [1]. However, most of these investigations were restricted to isothermal conditions, while characteristics of the wave flow of liquid films in the presence of significant thermocapillary effects remained almost unstudied. A few theoretical papers devoted to these problems have been published very recently [2, 3].

This Letter reports on the results of an experimental investigation of the flow of a water film over the surface of a vertical plate with a 150 × 150-mm heater situated 120 mm downstream from the flow entrance section. The Reynolds number of the flow was $\mathrm{Re} = \Gamma/\mu = 22$, where Γ is the specific mass flow rate and μ is the dynamic viscosity of the liquid. The initial temperature of the liquid was $T_0 = 24$°C. It was found that, as the heat flux q supplied from the heater increases, the flow rate distribution in the transverse direction (across the flow) becomes inhomogeneous: rivulets following with a certain wavelength are formed, which are separated by smooth thinned film regions. Further increase in the heat flux leads to the appearance of dry spots between rivulets. The rivulets limit expansion of the dry spots over the heater in the transverse direction.

The liquid film thickness was measured using a fiber optical reflection probe situated above the free surface of the film, over a thinned film region between rivulets near the lower edge of the heated area. The probe comprised two optical fibers, one of which emitted the probing radiation beam toward the liquid film and the other detected radiation reflected from the film surface. The method is based on the dependence of the reflected light intensity on the distance from the reflecting surface to the detector. The probing beam spot size on the film surface was 0.25–0.45 mm. The probe design and the method of thickness measurements are described in more detail elsewhere [4].

For $q = 0$, the wave pattern in the probed region displays a sequence of solitary two-dimensional waves propagating over the residual layer as described in [1]. The results of observations using a video camera showed that the average wavelength is $\lambda = 22$ mm. This value remained almost unchanged when the heat flux was increased. The table presents the results of our measurements for $q = 0$ in comparison to the data [1] reported for two-dimensional waves excited by flow rate pulsations. The characteristics of excited waves are determined by the flow rate and the frequency of induced oscillations, while being independent of the amplitude of these oscillations. As can be seen from the table, the natural waves possess somewhat lower amplitudes than the excited ones, although there is satisfactory general agreement between the results obtained in this study and the data reported in [1].

Wave flow characteristics measured under isothermal conditions in this study in comparison to the published data

Experimental conditions	Phase velocity of waves c, cm/s	Wave amplitude h_{max}, mm	Residual layer thickness h_{res}, mm
This study ($q = 0$)	24.2	0.263	1.141
Water flow with $\mathrm{Re} = 22$, $\lambda = 22$ mm, $T_0 = 20$°C [1]	27.0	0.298	0.133

1063-7850/04/3003-0231$26.00 © 2004 MAIK "Nauka/Interperiodica"

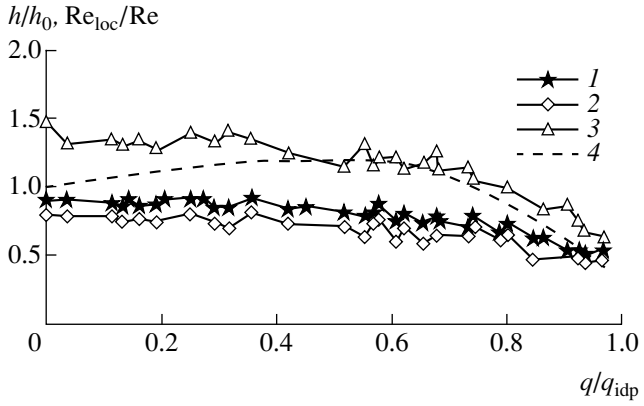

Fig. 1. Plots of the (*1*) average film thickness, (*2*) residual layer thickness, (*3*) amplitude of large waves, and (*4*) local Reynolds number versus dimensionless heat flux.

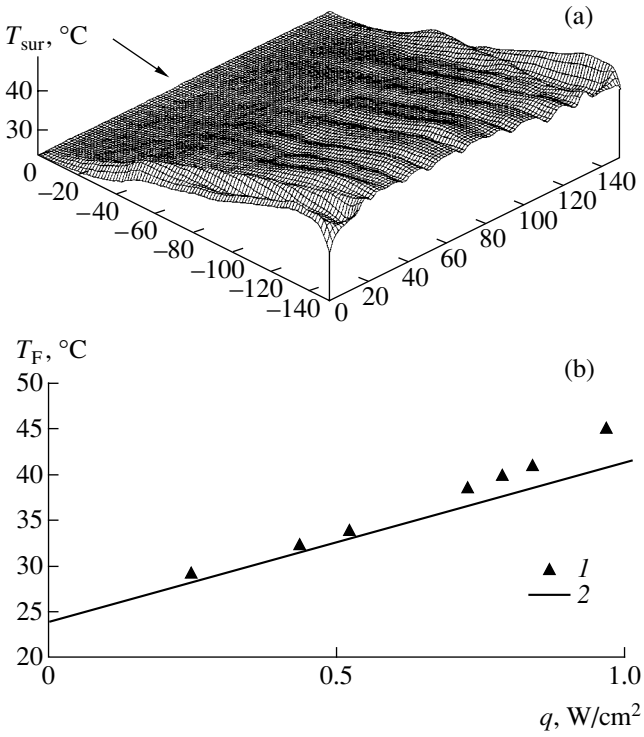

Fig. 2. (a) Temperature distribution over the liquid film surface in the heated region for $q = 0.97$ W/cm^2 (arrow indicates the flow direction); (b) mass-average temperature of the film (*1*) measured with a thermocouple and IR scanner and (*2*) calculated from the condition of thermal balance as a function of the heat flux.

Figure 1 presents data on the amplitude of large waves, average film thickness, and residual layer thickness as functions of the dimensionless heat flux q/q_{idp}, where $q_{\mathrm{idp}} = 0.99$ W/cm^2 is the heat flux for which a dry spot appears in the probed area. Each point in Fig. 1 was obtained by averaging data over a time period of 2–5 s. The average film thickness observed for $q = 0$ is approximately 10% lower than the value given by the Nusselt formula for a laminar liquid film, $h_0 = (3\mu\Gamma/\rho^2 g)^{1.3} = 0.178$ mm (ρ is the density of the liquid). This result agrees with the data reported in [1], where it was shown that a decrease in the film thickness compared to that predicted by the Nusselt formula takes place for strongly nonlinear waves of the type of a train of solitons separated by a residual layer. It was established that such a decrease may reach 10–12% for the waves with dimensionless numbers $k = 2\pi h_0/\lambda < 0.1$. In our case, $k = 0.05$.

As can be seen from Fig. 1, all three parameters of the wave flow initially remain virtually constant and start to decrease beginning with $q = 0.4 - 0.5q_{\mathrm{idp}}$, which is related to the onset of rivulet formation. The wave flow is retained until the very moment of liquid film rupture, but the wave amplitude decreases by a factor of 3–4. As the heat flux grows, the average film thickness h continuously decreases. However, when the thickness reaches $h \approx 0.5h_0$, the film spontaneously ruptures. Therefore, the process of thermocapillary rupture of the film involves two stages: (i) local thinning under the action of thermocapillary forces and (ii) spontaneous rupture at the site of maximum thinning upon reaching a certain critical thickness (apparently, corresponding to the film rupture under isothermal conditions).

Recently [4], we have measured the film thickness between rivulets in "regular structures" formed upon local heating of a flowing liquid film (heated area, 6.7×68 mm; Re = 2). It is interesting to note that, despite the fact that Reynolds number of the flow was significantly lower than the value used in this study, the liquid film thickness immediately before rupture was also reduced approximately to half of the initial value. It should be noted that the experiments [4] were performed with a 10% aqueous ethanol solution.

In Fig. 1, the dashed curve shows variation of the local Reynolds number at the point of observation, which was calculated taking into account the change in the local average thickness of the liquid film and the temperature dependence of its properties: $\mathrm{Re_{loc}/Re} = (h_{\mathrm{loc}}/h_{q=0})^3(\nu_{q=0}/\nu_{\mathrm{loc}})^2$, where $\nu = \mu/\rho$ is the kinematic viscosity of the liquid. The mass-average temperature of the film at the site of measurements for relatively small heat fluxes ($q < 0.5$ W/cm^2) was determined from the condition of thermal balance. For $q > 0.5$ W/cm^2 (i.e., when rivulets are formed in the liquid film and the local flow rate exhibits variations), the mass-average temperature of the film was determined based on the results of temperature measurements on the surface of the film and the heated substrate. The former temperature was measured using an IR scanner.

Figure 2a shows a two-dimensional thermogram of the film surface in the heated region for $q = 0.97$ W/cm^2. As can be seen, the temperature profile near the downstream edge of the heated area is inhomogeneous. The

temperature of the heated substrate surface was measured using a thermocouple. The mass-average temperature of the film was calculated as the arithmetic mean between the surface temperatures of the film and the substrate. The difference between these temperatures did not exceed 1 K, so that the error of determination of the mass-average temperature was within 0.5 K. Figure 2b shows a plot of the mass-average temperature versus heat flux, which was calculated from the condition of thermal balance. In the interval of $q < 0.5$ W/cm^2, the film thickness is almost constant (see Fig. 1) and the difference between calculated and experimentally measured temperatures does not exceed 1 K. For $q > 0.5$ W/cm^2, this difference begins to increase and reaches 5 K by the moment of film rupture ($q = 0.99$ W/cm^2). For an average temperature gradient in the flow direction, calculation using the thermal balance condition for $q \approx q_{idp}$ yields 0.12 K/mm; according to thermocouple readings, the average gradient at this moment is 0.13 K/mm.

Figure 3 compares data on the wave amplitude plotted in Fig. 1c to a generalized equation obtained in [1] for the amplitude of waves excited under isothermal flow conditions. As can be seen, experimental points for the natural waves (including those for $q = 0$) lie approximately 25% below those for the induced waves. Apparently, artificially excited waves can acquire somewhat higher amplitudes. The exponent at Re_{loc} (0.59) for the natural waves in the heated film is somewhat greater than that (0.46) for the induced waves. Therefore, when the local flow rate decreases under the conditions of increased heat flux, the drop of the wave amplitude in the region between rivulets is more pronounced than that expected according to the laws of "cold hydrodynamics." This is in disagreement with the theory [2] according to which the wave amplitude in a liquid film moving over a heated surface with nonnegative temperature gradient in the flow direction (in our case, the temperature gradient is positive) must increase as the heat flux increases. This discrepancy is probably related to the fact that the problem considered in [2] was two-dimensional, while the film flow in our case possesses a three-dimensional character.

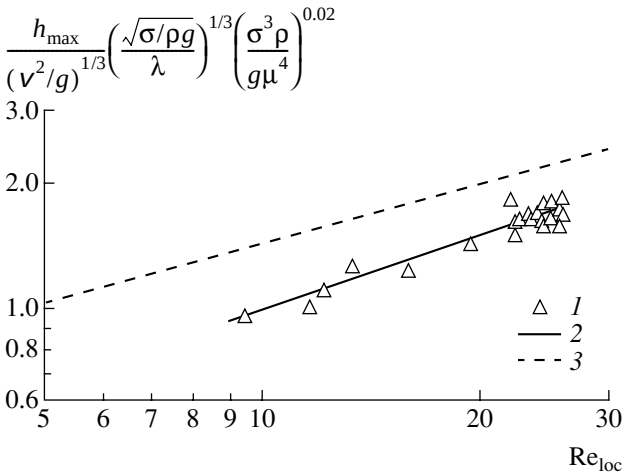

Fig. 3. Comparative data on the amplitude of waves arising in a heated film (this study) and excited under isothermal conditions (reported in [1]): (*1*, *2*) experimental data obtained in this study and their generalization $y = 0.25x^{0.59}$, respectively; (*3*) generalization $y = 0.49x^{0.46}$ [1] (σ is the surface tension of the liquid).

Acknowledgments. This study was supported by the Russian Foundation for Basic Research, project no. 02-02-16478.

REFERENCES

1. S. V. Alekseenko, V. E. Nakoryakov, and B. G. Pokusaev, *Wave Flow of Liquid Films* (Begell House, New York, 1994).
2. S. Miladinova, S. Slavtchev, G. Lebon, *et al.*, J. Fluid Mech. **453**, 153 (2001).
3. B. Scheid, A. Oron, P. Colinet, *et al.*, Phys. Fluids **14**, 4130 (2002).
4. D. V. Zaitsev, O. A. Kabov, and A. R. Evseev, Exp. Fluids **34**, 748 (2003).

Translated by P. Pozdeev

Technical Physics Letters, Vol. 30, No. 3, 2004, pp. 234–236. Translated from Pis'ma v Zhurnal Tekhnicheskoĭ Fiziki, Vol. 30, No. 6, 2004, pp. 38–44.

Studying the Bulk Dynamic Strength of a Quartz Glass by Laser-Induced Breakdown

N. F. Morozov, B. A. Zimin, B. N. Semenov, Yu. V. Sud'enkov, A. I. Suslikov, G. A. Baranov, A. A. Belyaev, and G. V. Tsvetkov

St. Petersburg State University, St. Petersburg, Russia

Efremov Institute of Electrophysical Equipment, St. Petersburg, Russia

Received August 25, 2003

Abstract—Methods and results of the investigation of pulsed pressures excited in the bulk of a quartz glass by focused nanosecond laser pulses ($\lambda = 1.06$ μm, $\tau_{0.5} \approx 12.5$ ns) are described. The experiments were performed in a wide range of laser power densities, which allowed the generation of pulsed pressures to be studied for both thermomechanical effect and optical damage in the bulk of glass. We have measured displacement of the free sample surface (laser interferometry), determined optical damage thresholds, and performed fractographic analysis of the fracture zones. The results revealed nonlinear thermomechanical response and allowed us to estimate the change in the optical absorption and temperature of the material near the optical damage threshold. Quantitative data are obtained on the relative efficiency of pulsed pressure production during the thermomechanical effect and optical damage. Data on the dynamic strength of a quartz glass are obtained for the first time in the absence of a damaged surface layer. Using the proposed method, it is possible to determine the energy consumption for the fracture of brittle materials. High sensitivity of the method of laser-induced breakdown allows this technique to be used for studying the influence of microstructure on the mechanical and optical properties of transparent media. © *2004 MAIK "Nauka/Interperiodica".*

Data on the dynamic strength of inorganic glasses are very restricted and rather contradictory [1–3]. Moreover, virtually no such information is available for short loading times on the order of 10^{-7} s and below. This situation is explained to a considerable extent by the significant difference between the bulk and surface strength of glasses, which hinders dynamic testing by traditional methods of impact loading. At the same time, it is known that, during the laser-induced breakdown in transparent dielectrics taking place under the action of high-power nanosecond and subnanosecond laser pulses, the laser plasma generates an intense pulse of pressure inducing mechanical fracture in the bulk of the material surrounding the laser-induced breakdown channel [4, 5]. Numerous investigations of the radiation strength of glasses provided for a quite clear physical pattern of this phenomenon, but the existing theoretical models do not allow the thermodynamic parameters of laser plasmas to be calculated with sufficient accuracy, which hinders evaluation of the pressures developed in the surrounding medium.

In order to obtain information about the thresholds of both radiation strength and dynamic strength of bulk transparent media (in particular, glasses), we have developed a method of pressure determination during the optical damage in the bulk of transparent materials.

The experiments were performed using a laser operating at a wavelength of 1.06 μm in a Q-switched regime with a pulse duration of $\tau_{0.5} \approx 12.5$ ns. We have studied the samples of fused quartz in the form of polished parallelepipeds with the dimensions $50 \times 20 \times 20$ mm. One face was coated by aluminum and served as a mirror in the laser Michelson interferometer with a stabilized working point and photoelectric band count [6]. The laser radiation beam was focused inside the sample by means of a short-focus lens ($f = 27$ mm) through the face perpendicular to the mirror, so that the focal plane coincided with the measuring beam of the interferometer.

The interferometer signal was due to a shift of the sample surface under the action of the acoustic pulse generated by a laser pulse at the focus point,

$$\frac{i(t)}{i_0} = \cos^2\frac{2\pi u(t)}{\lambda}, \qquad (1)$$

where $i(t)$ is the output current of the interferometer photodetector, $u(t)$ is the sample surface displacement, and $\lambda = 0.6328$ μm is the working wavelength of the laser interferometer.

The input and output laser radiation, as well as the emission from plasma in the laser-induced breakdown region, were monitored using vacuum photodiodes (FEK-09) whose response was also used for synchronization of the measuring tract. The radiation energy could be varied within 120 mJ and was measured by a calorimeter (IMO-2N). Each subsequent irradiation of the sample was performed at a new site with increasing laser energy. Using this approach, it was possible to determine the optical damage threshold with sufficient precision and to analyze the character and extent of radiation damage in comparison to the laser radiation

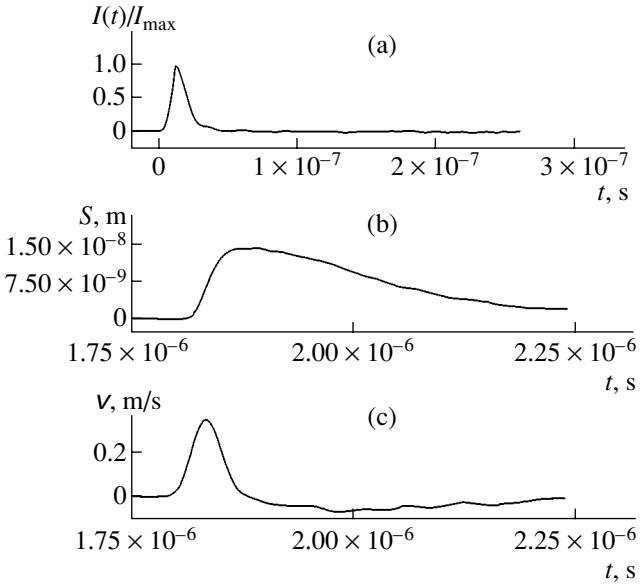

Fig. 1. (a) Laser radiation pulse shape $I(t)$, (b) the sample surface displacement under the action of a laser-induced acoustic pulse emerging at the surface, and (c) the velocity of the free surface displacement.

energy and the sample surface displacement. The character of the sample fracture was studied and the dimensions in two mutually perpendicular planes were measured with the aid of an optical microscope. Based on these data, the volume of the laser-induced breakdown channel and the fracture zone dimensions were determined for various laser energies.

Figure 1 presents (a) the laser radiation pulse shape, (b) the sample surface displacement under the action of an acoustic pulse emerging at the surface, and (c) the velocity of the free surface displacement. Using data on the displacement $u(t)$ and the velocity $v(t)$, adopting the elastic approximation, and assuming spherical symmetry of the problem, it is possible to calculate the mechanical energy liberated for both the thermal mechanism of the pulsed laser action upon the transparent medium and for the laser-induced breakdown.

The change in the mechanical energy during the elastic wave propagation can be described as

$$\frac{dW}{dt} = -\int_s e_n ds, \quad e_n = -\left(\frac{\partial v}{\partial t}\sigma_n\right). \tag{2}$$

The normal component of the power flux density of elastic waves in the far field zone can be rewritten as

$$e_n = \frac{\lambda + 2\mu}{c_l} v_n^2, \tag{3}$$

where λ and μ are the Lamé coefficients, c_l is the longitudinal velocity of sound, and v_n is the velocity of particles. Using relations (2) and (3), we obtain an expression for the total elastic energy transferred by the elastic wave,

$$W = \int_{t,s}\int e_n ds dt = 4\pi R^2 \frac{\lambda + 2\mu}{c_l}\int_0^\tau v(t)^2 dt, \tag{4}$$

where τ is the stress pulse duration and R is the distance from the point of laser radiation focusing to the sample surface.

The results of processing of the experimental data are presented in Fig. 2, which shows (a, b) the mechanical energy $W(E)$ transferred by the elastic wave, (c) the laser-induced breakdown channel volume $V(E)$, and (d) the volume density of mechanical energy $W_v(E) = W/V$ as functions of the laser radiation energy E.

The plot of $W(E)$ in Fig. 2b exhibits a jump at the laser radiation energy corresponding to the optical

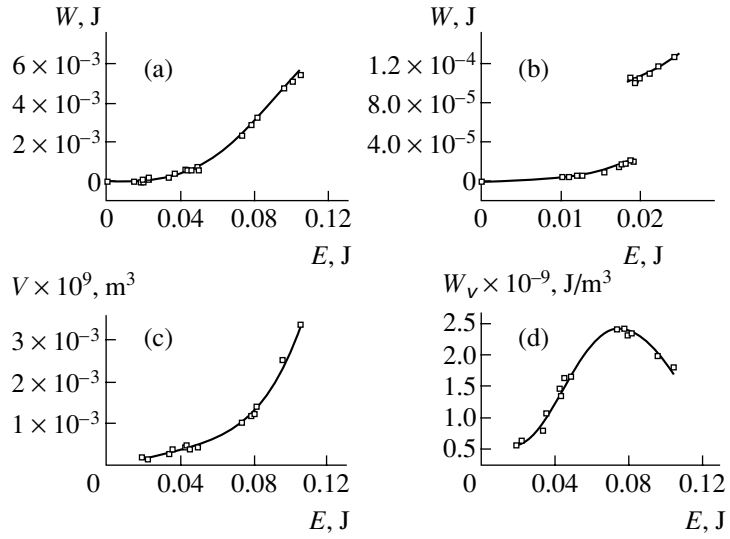

Fig. 2. Plots of (a, b) the mechanical energy $W(E)$ transferred by the elastic wave, (c) the laser-induced breakdown channel volume $V(E)$, and (d) the volume density of mechanical energy $W_v(E) = W/V$ as functions of the laser radiation energy E.

damage ($E_{o.d.} \cong 0.020 \pm 0.0015$ J). This behavior of $W(E)$ reflects a change in the mechanism of pressure pulse generation. The thermal mechanism changes for a more effective explosive mechanism related to the appearance of the laser-induced breakdown plasma. It should also be noted that, for laser radiation energies close to the threshold, $E \sim 0.75E_{o.d.} - E_{o.d}$, the character of the thermomechanical effect significantly deviates from a linear thermoeleastic behavior.

Assuming that the energy of elastic waves is equal to the change in the internal energy in the region of deposition of the laser radiation power, it is possible to obtain quite correct estimates of the optical absorption, temperature, and pressure in the focal region within the framework of a nondissipative thermal mechanism. The main errors of such estimates can be related to the uncertainty of determination of the focal region volume. We believe that these errors will not be very large if we assume the focal region volume to be approximately equal to that of the laser-induced breakdown channel at a radiation energy equal to the optical damage threshold ($E = E_{o.d.}$).

Prior to the laser-induced breakdown, the optical absorption coefficient ($n = W/E$) varies from 0.04 to 0.12% when E increases from 0.01 to 0.019 J. For the same radiation energies, the temperature increment averaged over the focal region volume is $\Delta T \cong 13$–80 K. Evaluating pressures from the Mie–Grüneisen equation of state ($\Delta P \cong \gamma W/V$, $\gamma \cong 0.8$ for quartz glass) using the experimental data for $E \cong 0.01$–0.019 J, we obtain $\Delta P \cong 21.5$–128 MPa. Under the conditions of laser-induced breakdown ($E > 0.02$ J), we can probably obtain only a lower estimate for the optical absorption with allowance of the influence of the material fracture and the related energy consumption. In the interval of laser radiation energies $E \cong 0.02$–0.11 J, the change in the optical absorption amounts to $n \sim 0.55$–5.5% and is mostly due to the radiation absorption by the laser-induced plasma.

Simple estimates of the temperatures and pressures in the region of the laser-induced breakdown can hardly be correct. Nevertheless, for a threshold laser radiation energy ($E_{o.d.} \cong 0.02$ J) at which only separate and small brittle cracks are formed together with the laser-induced breakdown channel, we may use pressure estimates for evaluating the bulk dynamic strength of transparent materials. For quartz glass, this estimate yields a dynamic strength of $P \cong 480$ MPa, in good agreement with the cleavage strength of a K8 glass ($\sigma \cong 450$ MPa) [8].

It should be noted that variation of the volume energy density $W_v(E)$ of the elastic wave exhibits a strongly nonlinear character (Fig. 2d), which is related to different rates of variation of the $W(E)$ and $V(E)$ functions (Figs. 2a and 2c) especially pronounced for $E > 0.08$ J. Apparently, the slower growth of the elastic energy is explained by increasing energy consumed for the brittle fracture of surrounding material, which determines the character of the $W_v(E)$ curve. By measuring the volume of the zone of fracture around the laser-induced breakdown channel, it is possible to evaluate this energy and, probably, to check for the validity of the Griffith criterion for the fracture of brittle materials in the submicrosecond interval of loading times.

In conclusion, it should be noted that an analysis of the experimental data in terms of the known solutions for a spherical cavity expanding in an unbounded medium [7, 9] will provide for refined estimates of the dynamic strength and allow the pressures and temperatures to be calculated for the laser-induced breakdown in transparent materials. Note also that experiments on the samples of two-phase glasses with different structures determined by thermal treatment regimes showed the high sensitivity of the proposed method, which allows it to be used in investigations of the influence of microstructure on the dynamic strength of brittle materials.

To summarize, the proposed method based on the laser-induced breakdown allows one to (i) determine both dynamic strength and radiation strength of the bulk transparent materials (which is especially important for inorganic glasses), (ii) obtain quantitative data on the thermodynamic parameters of a laser-induced breakdown plasma in transparent media, and (iii) study the dynamics of variation of the optical absorption of transparent media in the course of laser action.

Acknowledgments. This study was supported by the Federal Program "Universities of Russia" and by the Russian Foundation for Basic Research (project no. 01-01-00233).

REFERENCES

1. V. P. Pukh, *Strength and Fracture of Glasses* (Nauka, Leningrad, 1973) [in Russian].
2. G. V. Stepanov, *Elastic–Plastic Deformation and Fracture of Materials under Pulsed Loads* (Naukova Dumka, Kiev, 1991) [in Russian].
3. G. I. Kanel', S. V. Razorenov, A. V. Utkin, and V. E. Fortov, *Shock Wave Phenomena in Condensed Media* (Yanus-K, Moscow, 1996) [in Russian].
4. J. F. Ready, *Effects of High Power Laser Radiation* (Academic Press, New York, 1971; Mir, Moscow, 1974).
5. Yu. P. Raizer, *Laser-Induced Discharge Phenomena* (Nauka, Moscow, 1974; Consultants Bureau, New York, 1977).
6. Yu. V. Sud'enkov and V. I. Yurevich, Izv. Ross. Akad. Nauk **57** (12), 160 (1993).
7. V. A. Babeshko, E. V. Glushkov, and Zh. F. Zinchenko, *Dynamics of Inhomogeneous Linear Elastic Media* (Nauka, Moscow, 1989) [in Russian].
8. Yu. V. Sud'enkov, Pis'ma Zh. Tekh. Fiz. **27** (11), 30 (2001) [Tech. Phys. Lett. **27**, 454 (2001)].
9. V. S. Nikiforovskiĭ and E. I. Shemyakin, *The Dynamical Fracture of Solids* (Nauka, Novosibirsk, 1979) [in Russian].

Translated by P. Pozdeev

Technical Physics Letters, Vol. 30, No. 3, 2004, pp. 237–239. Translated from Pis'ma v Zhurnal Tekhnicheskoĭ Fiziki, Vol. 30, No. 6, 2004, pp. 45–51.

Peculiarities of the Mechanical Response of Heterogeneous Materials with Highly Deformable Interfaces

S. G. Psakhie, E. V. Shilko, and S. V. Astafurov*

Institute of Strength Physics and Materials Science, Siberian Division, Russian Academy of Sciences, Tomsk, 634055 Russia

** e-mail: astaf@usgroups.com*

Received August 26, 2003

Abstract—Peculiarities of the deformation and fracture of heterogeneous materials with a large fraction of interfacial regions (interfacial materials) under the action of complex alternating loads have been studied by computer-aided simulation. The dependence of the character of fracture, deformability, dissipation of the applied energy, and strain distribution in the material bulk on the frequency of cyclic loading was determined. High-frequency vibrations at a frequency much greater than that of the natural oscillations may significantly increase the deformability of interfacial materials. © *2004 MAIK "Nauka/Interperiodica".*

It is well known that many modern advanced materials, including nanostructural ones, have complex inner structures characterized by a considerable part of interfaces. The structure of such materials, frequently referred to as interfacial [1–3], can be represented by a set of elements (blocks) separated by interlayers possessing properties significantly different from those of the blocks. In many cases (in particular, for nanostructural materials), the interlayers consist of a strongly deformed material with a high density of defects. It should be noted that a "looser" structure of these layers decreases the resistance to shear and significantly influences the macroscopic properties of interfacial materials.

Peculiarities in the behavior of interfacial materials under complex loading conditions are of interest from the standpoint of both basic science and applications. This study was aimed at a theoretical investigation of the response and fracture of interfacial materials under the action of alternating loads.

The computer-aided simulation was performed using a new method of discrete mechanics—the method of movable cellular automata [4, 5]. This technique has been successfully used for many years in theoretical investigations of the response and fracture of complex heterogeneous media such as sintered composites, mountain masses, loose grounds, and coal beds [6–9].

We have studied a two-dimensional sample with the structure depicted in Fig. 1 (linear dimensions, 0.03×0.01 m). The left-hand edge was fixed in an immobile clamp. The mobile right-hand edge was loaded via a moving element. The sample had a composite internal structure comprising high-strength blocks separated by "plastic" interlayers. The elastic properties of blocks and interlayers were close to those for titanium [10]. The cellular automata of structural elements were characterized by a linear response function corresponding to that of a brittle but high-strength material (e.g., nanodimensional grains with a strength approaching the theoretical limit). For the automata of interlayers, the response function exhibited a long irreversible region reflecting its specific properties. An effective decrease in the resistance to shear in the region of interfaces was achieved by introducing breaks of the inter-automata bonds (Fig. 1). It should be noted that such a representation of interfacial materials, albeit idealized, provides for a qualitatively correct modeling of the main structural features. The dimensions of blocks and the thickness of interlayers are determined by the type of material modeled.

This study is devoted to the response of a preliminarily loaded sample subjected to alternating cyclic action. The preliminary straining was modeled by

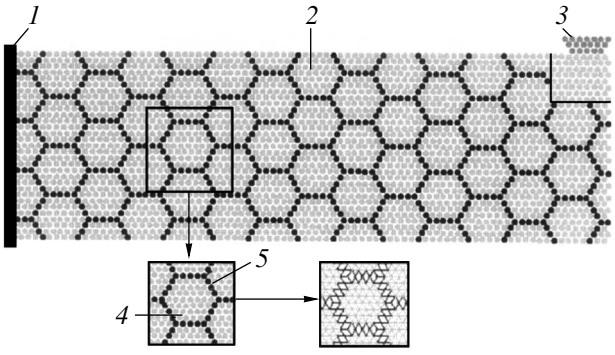

Fig. 1. Schematic diagram illustrating the geometry, mechanical features, and structure of the sample: (*1*) immobile clamp; (*2*) sample; (*3*) loading element; (*4*) structural block; (*5*) interlayer.

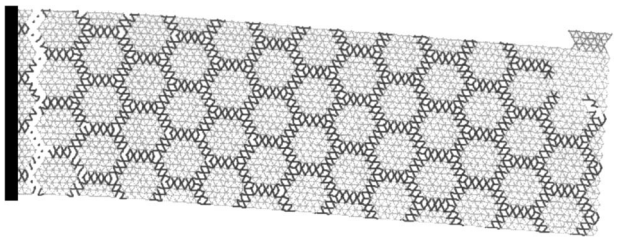

Fig. 2. The system of inter-automata bonds after opening of the main crack.

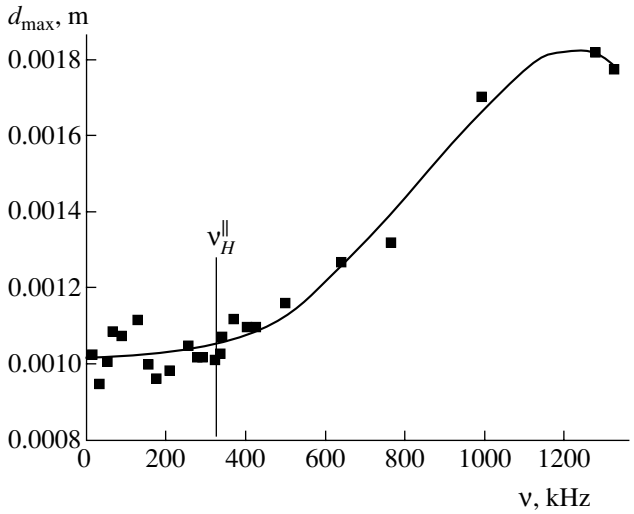

Fig. 3. A plot of the maximum displacement of the loading element versus frequency of vibrations.

applying a constant force $F_0 = 35$ N directed downward. The force was selected so as to provide that, by the time (t_0) of settling equilibrium, a considerable fraction of interlayers would reach the yield point. The vertical displacement of the loading element amounted to $d_0 = 0.82$ mm, which corresponded to a sample bending angle of $\gamma = 1.6°$.

The cyclic action on the sample was modeled by driving the loading element at a periodically varying velocity directed along the vertical axis. The total load applied to the sample can be presented as

$$\begin{cases} F_0 + V_A \sin\left(\dfrac{2\pi t}{T}\right), & (k \times T) < t < (k + 0.5) \times T, \\ F_0, & (k + 0.5) \times T < t < (k + 1) \times T, \end{cases}$$

where V_A is the amplitude of velocity variations, t is the current time, T is the period, and k is the cycle number. Thus, the velocity of displacement was set only within the first half-period. During the second half-period, only the constant force F_0 was applied. The calculations were performed for $V_A = 0.5$ m/s, which corresponded to rather weak periodic impacts (the amplitude of the loading element shift did not exceed 20 μm). Such a loading can be realized, for example, by using ultrasound.

The numerical experiment consisted in varying the frequency of vibrations $\nu = 1/T$ and studying the influence of this parameter on the features of material straining and the value of the maximum sample bending up to its fracture. In this loading mode, important parameters of the sample behavior include four natural frequencies related to the propagation of longitudinal and transverse elastic waves along the sample length L and height H. The values of these frequencies fall within the interval from $\nu_L^{\perp} = V_{\perp}/2L \approx 70$ kHz and $\nu_H^{\parallel} = V_{\parallel}/2H \approx 330$ kHz, where $V_{\parallel}$ and $V_{\perp}$ are the longitudinal and transverse sound velocities in the sample material.

The results of calculations performed in the interval of vibration frequencies from $0.2\nu_L^{\perp}$ to $4\nu_H^{\parallel}$ showed that the sample fracture proceeds, irrespective of the frequency, by the formation and accumulation of damage in the vicinity of the clamp (Fig. 2). It is important to note that the damages appear and develop so as to form the main crack only at the interfaces between blocks.

A thorough analysis of the results of simulation showed that the loading frequency significantly influences the character and distribution of plastic deformations in the sample and, hence, the maximum sample bending d_{max}. By the maximum bending we imply the vertical displacement of the loading element at the moment of opening (t_c) of the main crack. Figure 3 shows the plots of d_{max} versus cyclic loading frequency ν exhibiting two characteristic regions. In the first region (corresponding to the interval $\nu \le \nu_H^{\parallel}$), d_{max} varies about an average value of ~1.03 mm ($\gamma \approx 2°$), virtually not increasing. In the second region ($\nu > \nu_H^{\parallel}$), the maximum displacement of the loading element exhibits an almost twofold increase. Note that, as the frequency of vibrations is increased further ($\nu \gg \nu_H^{\parallel}$), d_{max} ceases to grow and oscillates about a new average value of ~1.7 mm ($\gamma \approx 3.2°$). This behavior was taken into account in constructing the interpolation.

Figure 4 presents a layer-by-layer distribution of the "reduced" normal deformations (d_1) in the interlayer material along the sample. The curves are constructed for the moment of time corresponding to opening of the main crack. Here, the term "reduced" deformation refers to the difference between the total (elastic + irreversible) deformation at the moment of break (t_c) and the value at the beginning of vibrational loading (t_0). As can be readily seen from Fig. 4, the increase in deformability of the material with increasing frequency ν is related primarily to the fact that increasing volume of the material is involved in the process of straining.

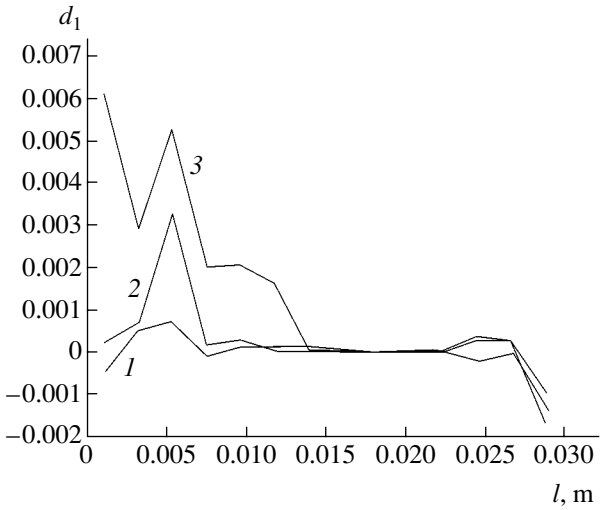

Fig. 4. Distributions of the "reduced" normal deformations in interlayers along the sample loaded at ν = 30 (*1*), 260 (*2*), and 1300 kHz (*3*).

Note that the main distinctive feature of the high-frequency curves ($\nu > \nu_H^{\parallel}$) is related to the involvement of the second quarter of the sample (extending from 0.0075 to 0.0015 m) into the process of intense straining. The accumulation of plastic deformation in this region (Fig. 4, curve *3*) leads to smearing of the stress concentrator in the vicinity of the clamp, thus elongating the lifetime and increasing the maximum bending of the sample.

Thus, the results of our numerical experiments show the possibility of increasing the deformability of interfacial materials under the conditions of high-frequency cyclic loading. Although the characteristic dimensions of the structural elements of our sample are several orders of magnitude greater than the grain size of real nanostructural materials, the proposed model is sufficiently general for establishing characteristic features in the behavior of interfacial materials.

Acknowledgments. This study was supported by the Russian Science Support Foundation, the Presidential Grant for Young Scientists (project no. MK-2573.2003.05), the Presidential Program of Support for Leading Scientific Schools in Russia (Scientific School of Academician V.E. Panin, project no. NSh-2324.2003.1), and jointly by the Ministry of Education of the Russian Federation and the US Civilian Research and Development Foundation for the Independent States of the Former Soviet Union (CRDF) within the framework of the BRHE Program (project no. TO-016-02).

REFERENCES

1. V. A. Raghunathan, P. Richetti, and D. Roux, Langmuir **12**, 3789 (1996).
2. L. Jin, C. Bower, and O. Zhou, Appl. Phys. Lett. **73**, 1197 (1998).
3. S. Ochiai, M. Hojo, K. Schulte, and B. Fiedler, Composites, Part A **32**, 749 (2001).
4. S. G. Psakhie, Ya. Horie, S. Yu. Korostelev, *et al.*, Izv. Vyssh. Uchebn. Zaved. Fiz., No. 11, 58 (1995).
5. S. Psakhie, Y. Horie, G. Ostermeyer, *et al.*, Theor. Appl. Fract. Mech. **37**, 311 (2001).
6. S. G. Psakhie, E. V. Shil'ko, A. I. Dmitriev, *et al.*, Pis'ma Zh. Tekh. Fiz. **22** (12), 69 (1996) [Tech. Phys. Lett. **22**, 511 (1996)].
7. S. G. Psakhie, D. D. Moiseenko, A. I. Dmitriev, *et al.*, Pis'ma Zh. Tekh. Fiz. **24** (4), 71 (1998) [Tech. Phys. Lett. **24**, 154 (1998)].
8. S. G. Psakhie, S. Zavshek, J. Jezershek, *et al.*, Comput. Mater. Sci. **19** (1–4), 69 (2000).
9. V. V. Ruzhich, S. G. Psakhie, S. A. Bornyakov, *et al.*, Fiz. Mezomekh. **6**, 41 (2003).
10. A. V. Bobylev, *A Handbook of Mechanical and Technological Properties of Metals* (Metallurgiya, Moscow, 1980) [in Russian].

Translated by P. Pozdeev

Technical Physics Letters, Vol. 30, No. 3, 2004, pp. 240–243. Translated from Pis'ma v Zhurnal Tekhnicheskoĭ Fiziki, Vol. 30, No. 6, 2004, pp. 52–61.

Dissipative Losses of Mechanical Energy and Heating of the Probe in Dynamic Contact with the Sample Surface in a Scanning Microscope

G. V. Dedkov* and E. G. Dedkova

Kabardino-Balkarian State University, Nalchik, Kabardino-Balkaria, Russia

** e-mail: gv.dedkov@mail.ru*

Received September 3, 2003

Abstract—Dissipative losses of mechanical energy and the rate of heating of the scanning microscope probe in dynamic contact with the sample surface have been theoretically estimated for a small temperature difference between the probe and the sample. Time variation of the temperature and the power of nanoprobe heating (cooling) caused by the near-zone fluctuational electromagnetic field have been calculated. Averaged over the period of nanoprobe oscillations, this thermal power significantly exceeds the power of mechanical losses even for small local variations of the sample surface temperature. For this reason, heating of the probe can stimulate its additional damping. This may account for the discrepancy between theoretical and experimental values of dissipative forces. © *2004 MAIK "Nauka/Interperiodica".*

The kinetics of heat exchange in the contact of a probe apex with the sample surface in a scanning probe microscope (SPM) is among the most important factors in scanning probe microscopy. The knowledge of this process is necessary for the development of this method and the correct interpretation of data obtained using various SPM techniques, especially with a view to development of the thermal probe microscopy of surfaces [1, 2] and the dissipative force microscopy [3–5]. Unfortunately, theoretical interpretation of the observed dissipative losses of the SPM oscillator operating in a contactless dynamic mode with constant amplitude (excluding the phenomenon of adhesion hysteresis [3, 4]) is still among unresolved problems. It is commonly accepted that, under these conditions, the main role is played by the fluctuational electromagnetic interaction of the probe with the surface. However, our theoretical estimates [6, 7] showed that calculated dissipative losses of the mechanical energy of a cantilever turn out to be 3–11 orders of magnitude lower than the values observed for silicon–mica and aluminum–gold contacts.

Recently [8], we paid attention to one important peculiarity of the fluctuational electromagnetic interaction. Even for a small temperature difference ($\Delta T \ll 1$ K) between a particle and a surface at a short distance from each other, there is an intense heat flux between them caused by the tunneling of "nonradiative" photons belonging to modes of the fluctuational electromagnetic field. The ratio of the dissipated mechanical power (averaged over the oscillation period) to the rate of heat exchange is on the order of f^2/f_W^2, where f and f_W are the probe oscillation frequency and the Wien frequency. Room-temperature Wien frequency is $f_W = kT/h = 3.9 \times 10^{13}$ Hz, and the typical probe frequency is $f = 3 \times 10^5$ Hz, which yields $f^2/f_W^2 \sim 10^{-16}$. Therefore, in the typical SPM situation, a contribution to the heat flux independent of the probe velocity and proportional to ΔT prevails over the dynamic contribution independent of ΔT. Since local variations of the sample surface temperature on a level of 1–100 mK are quite probable even under general isothermal conditions, the resulting heat flux may initiate additional mechanisms of dissipative losses, for example, by activating processes of the electronic and atomic exchange, rearrangement of the electronic and atomic structures, phonon excitation, and/or by inducing changes in the internal damping of the cantilever. Note that such mechanisms can be operative irrespective of the sign of ΔT.

The aim of this study was to calculate the dissipative losses of mechanical energy and the rate of heating (cooling) of the scanning microscope probe and to determine the kinetics of thermal equilibrium settling in the dynamic contact of the probe with the sample surface. If the heat flux initiates dissipation of the mechanical energy and variation of the SPM oscillator quality factor, the results of experimental measurements can provide for the development of a contactless thermocouple capable of determining the local temperature field at the sample surface in a dynamic mode with an accuracy of ~1 mK and a spatial resolution of ~1 nm.

In order to obtain theoretical estimates within the framework of the theory developed in [6, 7], it is necessary to know the properties of materials in contact described in terms of the dielectric response functions

$$\Delta_{1,2}(\omega) = (\varepsilon_{1,2}(\omega) - 1)/(\varepsilon_{1,2}(\omega) + q_{1,2}), \qquad (1)$$

where the subscripts 1 and 2 refer to the probe and sample surface, respectively; $q_1 = 2$; $q_2 = 1$; and $\varepsilon_{1,2}(\omega)$ is the dynamic permittivity of the corresponding material. With allowance of the spatial dispersion, $\Delta_2(\omega)$ has to be replaced by

$$\Delta_2(\omega, \mathbf{q}) = \frac{\pi - qI_0}{\pi + qI_0}, \quad I_0 = \int_{-\infty}^{+\infty} \frac{dk_z}{(k_z^2 + q^2)\varepsilon(\omega, \mathbf{k})}, \quad (2)$$

where $\mathbf{k} = (\mathbf{q}, k_z)$, $\mathbf{q}$ is the two-dimensional wavevector in the sample surface plane, and k_z is the wavevector component normal to the surface.

For the sake of simplicity, the dielectric function $\varepsilon(\omega, \mathbf{k})$ is assumed to be same for both probe and sample materials and expressed as [6, 7]

$$\varepsilon(\omega, \mathbf{k}) = 1 + \frac{\omega_P^2}{V_F^2 k^2 [1 - i\pi\omega\theta(2k_F - k)/2kV_F]/3 - \omega(\omega + i\gamma)}, \quad (3)$$

where $\theta(x)$ is the Heaviside unit step function; V_F and k_F are the Fermi velocity and wavevector, respectively; ω_P is the plasma frequency; $\gamma = \omega_P^2/4\pi\sigma$ is the plasmon mode damping factor; and σ is the dc conductivity. Formula (3) takes into account the spatial dispersion of plasmons, the damping due to electron–hole excitations (described by the term with $\theta(x)$ in the denominator), and the decay of collective (plasmon) modes. It can be readily checked that, in the low-frequency approximation with neglect of spatial dispersion, formula (3) simplifies to

$$\varepsilon(\omega) = 1 + 4\pi\sigma i/\omega. \quad (4)$$

Restricting the consideration to a nonrelativistic case [6, 7], using formulas (1)–(4), and denoting the probe and sample temperatures as $T + \Delta T$ and T, respectively, we obtain the following expressions for the heat flux from the probe to sample surface and for the dissipative force at the probe (modeled by a spherical particle of radius R):

$$\dot{Q} = -\frac{9\zeta(4)}{2\pi^3}\frac{R^3}{z_0^3}\frac{\hbar}{\sigma^2}\left(\frac{k_B T}{\hbar}\right)^4 \frac{\Delta T}{T} F_1(\lambda/z_0, k_{TF}z_0) + \frac{3\zeta(2)R^3\hbar V^2}{128\pi^3 z_0^5 \sigma^2}\left(\frac{k_B T}{\hbar}\right)^2 F_2(\lambda/z_0, k_{TF}z_0), \quad (5)$$

$$F_1(x, y) = \int_0^\infty z^2 e^{-z} dz \frac{1 + \left(\frac{\pi^2}{3}\right)xz}{\left(1 + \frac{0.75}{y^2}z^2\right)^2} \times \left[1 + 0.404xz - 2.094xz\ln\left(\frac{z}{2y}\right)\right], \quad (6)$$

$$F_2(x, y) = \int_0^\infty z^4 e^{-z} dz \frac{1 + \left(\frac{\pi^2}{3}\right)xz}{\left(1 + \frac{0.75}{y^2}z^2\right)^2} \times \left[1 + 0.404xz - 2.094xz\ln\left(\frac{z}{2y}\right)\right], \quad (7)$$

$$F_d = -\frac{3\chi\zeta(2)}{256\pi^3}\frac{\hbar R^3 V}{\sigma^2 z_0^5}\left(\frac{k_B T_2}{\hbar}\right)^2 F_2(\lambda/z_0, k_{TF}z_0). \quad (8)$$

Here, $\lambda = V_F\sigma/\omega_P^2$, $\zeta(n)$ is the Euler zeta function, V is the particle velocity, z_0 is the distance from the probe apex to the surface, and χ is a numerical coefficient on the order of unity, which depends on the direction of motion ($\chi = 1$ for particle movements parallel to the surface and $\chi \approx 2$–4 for normal displacements).

With neglect of spatial dispersion ($x = 0$, $y \longrightarrow \infty$), formulas (6) and (7) yield $F_1(0, \infty) = 2$ and $F_2(0, \infty) = 24$. Adopting harmonic approximation for the cantilever oscillations in experiment [3, 4], we have

$$z(t) = A\cos(2\pi ft), \quad V = \dot{z}(t) = -2A\pi f\sin(2\pi ft), \quad (9)$$

where A and f are the amplitude and frequency of oscillations. The dissipated mechanical power $\bar{P}$ and the heat flux $d\bar{Q}/dt$ (both averaged over the oscillation period) are as follows:

$$\bar{P} = f\int_0^{1/f} |F_d(z(t), \dot{z}(t), d)\dot{z}(t)|dt, \quad (10)$$

$$\frac{d\bar{Q}}{dt} = f\int_0^{1/f} \dot{Q}(z(t), \dot{z}(t), d)dt. \quad (11)$$

Consider the nanoprobe with a parabolic cross section and the curvature radius R made of a material with a dielectric function of type (4). Substituting expressions (5), (8), and (9) into Eqs. (10) and (11), integrating over the probe volume, and averaging over the oscillation period, we obtain

$$\bar{P}(A, d) = -\frac{9\zeta(2)\hbar R}{32\pi}\frac{A^2 f^2}{(d^2 - A^2)^{3/2}}\left(\frac{k_B T}{\hbar\sigma}\right)^2, \quad (12)$$

$$\frac{d\bar{Q}}{dt} = \frac{27\hbar R}{4\pi^3(d^2 - A^2)^{1/2}}\left(\frac{k_B T}{\hbar\sigma}\right)^2 \times \left(-\zeta(4)\frac{\Delta T}{T}(k_B T/\hbar)^2 + \frac{\pi^2 A^2\zeta(2)}{48(d^2 - A^2)}f^2\right), \quad (13)$$

where d is the initial distance from the probe apex to the sample surface ($d < A$). For determining the mechanical

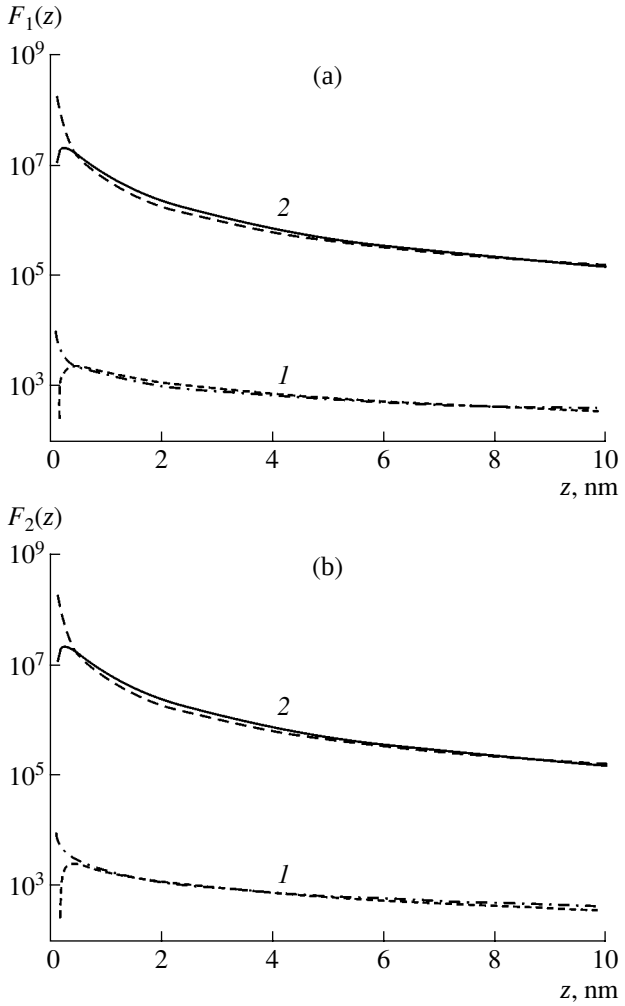

Fig. 1. The plots of (a) $F_1(x, y)$ and (b) $F_2(x, y)$ versus distance z calculated for the aluminum–aluminum contact with spatial dispersion taken into account for the sample only (curves *1*) or for both sample and probe (curves *2*). Dashed and dot-dashed curves represent the analytical approximations $5 \times 10^6/z^{1.5}$ and $1600/z^{0.6}$ (a) and $1.1 \times 10^8/z^{1.1}$ and $6 \times 10^4/z^{0.5}$ (b), respectively.

energy loss (heat income) per oscillation period, the right-hand parts of formulas (12) and (3) have to be divided by the frequency f.

A comparison of the $\bar{P}$ value to the dynamic contribution in $d\bar{Q}/dt$ proportional to f^2 shows that these quantities are almost identical (differing by a coefficient of 1/2). For the experimental conditions studied in [4] (aluminum probe in dynamic contact with Au(111) surface), formulas (12) and (13) yield for $d - A = z_{min} = 0.5$ nm an estimate of $\bar{P} = 4.2 \times 10^{-30}$ W. This value is 17 orders of magnitude lower than that following from experimental data [4]. At the same time, a velocity-independent contribution to the heat flux (described by the first term in (13)) is many orders of magnitude greater (even for a small temperature difference ΔT: $d\bar{Q}/dt = 2.4 \times 10^{-16}\Delta T$ W). Note that both $\bar{P}$ and $d\bar{Q}/dt$ strongly depend on the conductivity: for poor conductors ($\sigma \sim 10^{10}$ s^{-1}), the estimates may increase by ~14 orders of magnitude in comparison to normal metals ($\sigma \sim 10^{17}$ s^{-1}). However, the calculations for normal metals have to be performed with dielectric functions of the more general type (3) taking into account spatial dispersion. In this case, $\bar{P}$ and $d\bar{Q}/dt$ were calculated numerically, since formulas (5) and (8) have to be integrated over the probe volume prior to substitution into (12) and (13).

Despite simplifications, some general conclusions can be derived from the results of calculations according to formulas (6) and (7). Figures 1a and 1b show the plots of $F_1(x, y)$ and $F_2(x, y)$ versus distance z calculated for the aluminum–aluminum contact with spatial dispersion taken into account for the sample only (curves *1*) or for both sample and probe (curves *2*). As can be seen, making allowance for spatial dispersion increases both dissipative forces and the heat flux by 3–8 orders of magnitude. For the conditions studied in [4], the numerical calculation yields $\bar{P} = 5.7 \times 10^{-24}$ W and $d\bar{Q}/dt = 2.2 \times 10^{-9}\Delta T$ W (with total account of spatial dispersion). Accordingly, the heat supplied to the probe per oscillation period amounts to $\Delta\bar{Q} = 5.1 \times 10^4 \Delta T$ eV. For comparison, note that the mechanical energy of a cantilever with a stiffness of 40 N/m and an oscillation amplitude of 20 nm is 5×10^4 eV, while the mechanical energy losses due to internal damping of the cantilever amount to 1–30 eV per period. Thus, the presence of such a considerable heat flux between probe and sample implies the need for a more detailed investigation of the kinetics of thermal equilibrium settling in this dynamic contact.

Let us solve a simplified problem by considering the probe as a semi-infinte rod with a lumped heat flux $\dot{Q} = -\alpha\Delta T$ supplied to the probe end (facing the sample surface). For definiteness, let the sample surface temperature be higher than that of the probe, so that $\Delta T < 0$. This approximation is justified, since the heat flux rapidly decays with the distance from the surface, while the vertical size of the region of maximum heating (a few nanometers) is significantly smaller compared to the SPM needle height (1–10 μm). In addition, the heating power can be replaced by a value averaged over the oscillation period, because the time of thermal equilibrium settling is significantly greater than the oscillation period. Under these conditions, the temperature profile along the probe is described by the heat conductivity equation with a boundary condition of the third kind:

$$\begin{cases} \dfrac{\partial T}{\partial t} = a^2 \dfrac{\partial^2 T}{\partial z^2}, \\ \left.\dfrac{\partial T}{\partial z}\right|_{z \to 0} = h(T(0, t) - T_0 - \Delta T), \quad T(z, 0) = T_0, \\ 0 < t < \infty, \quad 0 < z < \infty, \end{cases} \tag{14}$$

where a^2 is the thermal diffusivity, h is the parameter of heat exchange with the surface, and T_0 is the initial temperature of the probe. The general solution to Eq. (14) can be conveniently written in the following form:

$$f(z,t) \equiv (T(z,t) - T_0)/\Delta T$$
$$= \mathrm{erfc}\left(\frac{z}{2a\sqrt{t}}\right) - \exp(zh + a^2h^2t)\,\mathrm{erfc}\left(\frac{z}{2a\sqrt{t}} + ah\sqrt{t}\right), \quad (15)$$

where erfc(x) is the complementary error function. Expression (15) shows that the kinetics of probe heating is determined by the dimensionless parameters $\beta = ah\sqrt{t}$ and $\gamma = z/2a\sqrt{t}$. At the probe apex ($z = 0$), the time variation of the temperature is described by a simpler formula

$$f(0,t) = 1 - \exp(\beta^2)\,\mathrm{erfc}(\beta). \quad (16)$$

According to the above considerations, the coefficient α in the expression for the total heat flux to the probe ($\bar{\dot{Q}} = -\alpha\Delta T$) can reach ~$10^{-9}$ W/K. Let $d - A = z_0$ be the minimum distance from the probe apex to the surface. Since $\bar{\dot{Q}}$ rapidly decreases with increasing z_0, the effective area of the heated surface of a parabolic probe can be estimated as $\Delta S = \pi\rho^2 = 2\pi RH_{\mathrm{eff}}$, where $H_{\mathrm{eff}} \approx 10z_0$. Then, $\Delta S \approx 20\pi Rz_0$ and, accordingly,

$$h = \frac{\alpha}{a^2C_P\rho\Delta S} \approx \frac{\alpha}{20\pi Rz_0a^2C_P\rho}. \quad (17)$$

For $z_0 = 0.5$ nm, $R = 35$ nm, $\alpha = 10^{-9}$ W/K and the parameters of aluminum ($C_P = 858$ J/(kg K), $\rho = 2700$ kg/m^3, $a^2 = 10^{-4}$ m^2/s), formula (17) yields $h = 3.9 \times 10^3$ m^{-1}.

Figure 2 shows the plots of $f(z, t)$ versus time for various cross sections of the probe. As can be seen, leveling of the probe and sample surface temperatures proceeds rather slowly: thermal equilibrium is not attained even for $\beta = 2$–5, and the probe apex remains significantly heated over the entire period of close dynamic contact with the sample (i.e., during the whole time of signal accumulation at a given point of the scan). For example, $f(0.2) = 0.75$ and, hence, the heating power still amounts to 25% of the initial value. The corresponding time of heating is $t_0 = \beta^2/a^2h^2 = 0.0026$ s (if a and h refer to aluminum). This estimate confirms the above conclusion that the time of thermal equilibrium settling is significantly greater than the period of mechanical oscillations of the probe (3×10^{-6} s).

Since the time required for attaining thermal equilibrium between probe and surface at a fixed scanning point depends on the heating rate and on h ($t \sim h^{-2}$), the equilibrium is settled more rapidly at a higher rate of heat exchange. When the system approaches equilibrium, mechanisms of the "thermoinduced" friction become less effective and the SPM oscillator damping decreases. Therefore, the kinetics of attaining thermal equilibrium can be determined by monitoring the quality factor of the oscillator in contact with the sample surface.

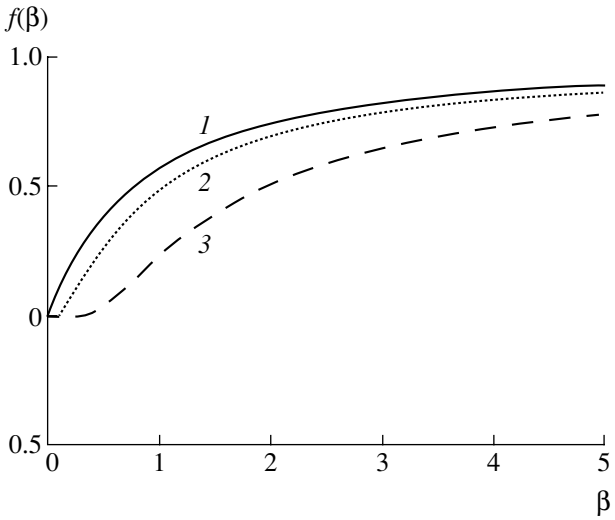

Fig. 2. Time variation of the temperature in various cross sections of the probe: $\beta = ah\sqrt{t}$; $\gamma = zh/2 = 0$ (*1*), 0.1 (*2*), and 0.5 (*3*).

REFERENCES

1. A. Majumdar, J. P. Carrejo, and J. Lai, Appl. Phys. Lett. **62**, 2501 (1993).
2. J. B. Xu, K. Lauger, K. Dransfeld, and I. H. Wilson, Rev. Sci. Instrum. **65**, 2262 (1994).
3. B. Gotsmann, C. Seidel, B. Anczykowski, and H. Fuchs, Phys. Rev. B **60**, 11051 (1999).
4. B. Gotsmann and H. Fuchs, Phys. Rev. Lett. **86**, 2597 (2001).
5. B. Gotsmann and H. Fuchs, Appl. Surf. Sci. **188**, 355 (2002).
6. G. V. Dedkov and A. A. Kyasov, Fiz. Tverd. Tela (St. Petersburg) **44**, 1729 (2002) [Phys. Solid State **44**, 1779 (2002)].
7. G. V. Dedkov and A. A. Kyasov, Phys. Low-Dimens. Semicond. Struct. **1**–**2**, 1 (2003).
8. G. V. Dedkov and E. G. Dedkova, in *Proceedings of the Scanning Probe Microscopy Conference, Nizhni Novgorod, 2003,* p. 255.

Translated by P. Pozdeev

Technical Physics Letters, Vol. 30, No. 3, 2004, pp. 244–246. Translated from Pis'ma v Zhurnal Tekhnicheskoĭ Fiziki, Vol. 30, No. 6, 2004, pp. 62–66.

An Analog of the Vavilov–Cherenkov Radiation Generated by a Moving Macroscopic Source

F. F. Valiev

Fock Institute of Physics, St. Petersburg State University, St. Petersburg, Russia

e-mail: valiev@hiex.phys.spbu.ru

Received September 11, 2003

Abstract—The pulses of current formed when a pulse of gamma quanta travels over an extended absorbing region have been numerically simulated. Features of the electromagnetic field generated by these pulses are considered. © *2004 MAIK "Nauka/Interperiodica".*

In recent years, much attention has been devoted to the electromagnetic fields of radiators moving with velocities equal to or greater than the speed of light in vacuum [1, 2]. Such a source can be obtained, for example, by directing a pulse of hard electromagnetic radiation onto a cylindrical rod with the length greater than the diameter. If the plane front of this radiation is perpendicular to the cylinder axis, the pulse of current generated in the rod will move at a velocity equal to the speed of light c. In all other cases (nonorthogonal incidence), the pulse will propagate at a supraluminal velocity. Although all electrons move with velocities certainly below that of light, the propagation of a region with nonzero current density along the rod can be represented as the motion of an effective charge at a supraluminal velocity.

In order to describe the distribution of secondary electromagnetic waves formed by such a current pulse, it is necessary to solve two problems: first, to determine the shape of the current pulse generated by a short pulse of the primary hard radiation; second, to solve the problem of electrodynamics with the initial conditions corresponding to the current pulse obtained. Both these problems encounter insufficiently studied aspects. In particular, the formation of current pulses by the primary hard radiation beam was previously studied for the most part phenomenologically. For example, Karzas and Letter [3] studied the electromagnetic fields generated by nuclear explosions.

In this study, the shape of the current pulse propagating at a supraluminal velocity was determined by considering microscopic motions of separate electrons. Then, using an approach proposed by Manankova [4] (based on the incomplete separation of variables [5] and the Riemann formula), the electromagnetic field of current pulses traveling over a given segment at a supraluminal velocity $v > c$ was calculated.

The first problem was solved taking into account optical absorption, Compton scattering, and the secondary effects accompanying the interaction of delta electrons with matter, which lead to the formation of ions and electrons. The shape of the current pulse was calculated using a numerical method described previously [6]. This algorithm allows the time evolution of the distribution of electrons in the phase space to be studied. The formation of electrons with energies above 10 keV was simulated using the program package GEANT [7].

The numerical experiment was performed according to the following scheme. An absorbing region (cell) bounded by a cylindrical surface and two edge planes perpendicular to the cylinder axis of symmetry (z axis of the cylindrical coordinate system ρ, z, φ) was irradiated by gamma quanta possessing a momentum of 60 keV/s. The cylinder was made of carbon and had a wall thickness of 10^{-4} m, a length of $l = 50$ m, and a diameter of 0.2 m. This cell was filled with air at a pressure of 1 bar and placed in vacuum. The photons were simultaneously emitted in the direction of the z axis from a plane making an angle of $\theta = \arctan(0.1)$ with the z axis. Numerical calculations gave the distribution $N(\rho)$ of electrons passing through a fixed cross section $z = z_0 > 0$. This distribution characterized the transverse localization of current. For the given experimental parameters, the distribution function $N(\rho)$ had a half-width of $\Delta R < 10$ cm. This value obeys the condition $l \gg \Delta R$ necessary for applicability of the linear current model used in simplified electrodynamic calculations.

Figure 1 shows the shape of the current pulse in the cross section of the absorbing region at $z_0 = 30$ m. The pulse duration ΔT on a 0.1 amplitude level does not exceed 0.2 ns (or 6 cm in ct units). This ΔT value gives an estimate of the longitudinal localization of current (along the z axis). Calculations yield the current pulse

shapes in various cross sections of the cylinder. The pulse propagation velocity in the z axis direction is $v = c/\cos\theta$. The shape of the running pulse was approximated by the function

$$J(z, \tau) = A[1 - \exp(-\alpha_1(\beta\tau - z))]\exp(-\alpha_2(\beta\tau - z)),$$
$$\alpha_i > 0, \quad i = 1, 2, \tag{1}$$

where $\tau = ct$ is the temporal variable, $\beta = v/c$, A is a constant factor, and $\alpha_i > 0$ ($i = 1, 2$) are the coefficients determined by least squares.

The vector of magnetic induction was calculated within the framework of a simplified model of linear current using a general solution of the system of Maxwell equations for a current pulse moving along a straight line. This solution for initial zero conditions was obtained in [2], where the electric field and magnetic induction vector components were expressed via a single scalar function $V(\rho, z, \tau)$. The edge effects were ignored because the necessary condition $l \gg \Delta T$ was fulfilled.

A nonzero component of the current density vector can be written as

$$j_z = \frac{\delta(\rho)}{2\pi\rho}h(\beta\tau - z)h(z)h(l - z)J(z, \tau), \quad \tau > 0,$$
$$j_z = 0, \quad \tau < 0, \tag{2}$$

where $h(z)$ is the Heaviside function and $\delta(\rho)$ is the Dirac delta function. For an axially symmetric source, components of the electric field (**E**) and magnetic induction (**B**) vectors can be expressed via the Bromwich–Borgnis potential u. This allows the problem to be formulated as

$$\left(\frac{\partial^2}{\partial\tau^2} - \frac{1}{\rho}\frac{\partial}{\partial\rho}\left(\rho\frac{\partial}{\partial\rho}\right) - \frac{\partial^2}{\partial z^2}\right)V = \frac{4\pi}{c}j_z,$$
$$j_z = V = 0, \quad \tau < 0, \tag{3}$$

where $V = \partial u/\partial\tau$. A nonzero component of the magnetic induction vector is related to the solution of this equation as $B_\varphi = -\partial V/\partial\rho$. A solution of Eq. (3) in the space–time representation is given by the expression

$$V(\rho, z, \tau)$$
$$= \frac{1}{c}\int_{z-\tau}^{z+\tau} h(\beta\tau - z')h(z')h(l - z')\frac{1}{\sqrt{\rho^2 + (z - z')^2}}$$
$$\times\left(\int_0^{-z'+\tau-z} d\tau' J(z', \tau')\delta(\tau' - \tau + \sqrt{\rho^2 + (z - z')^2}) \right.$$
$$\left. + \int_0^{-z'+\tau+z} d\tau' J(z', \tau')\delta(\tau' - \tau + \sqrt{\rho^2 + (z - z')^2})\right)dz'. \tag{4}$$

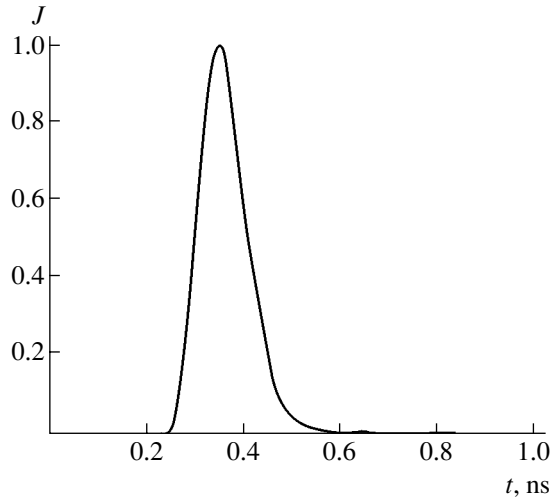

Fig. 1. The normalized current pulse profile in the cross section of the absorbing region at $z_0 = 30$ m.

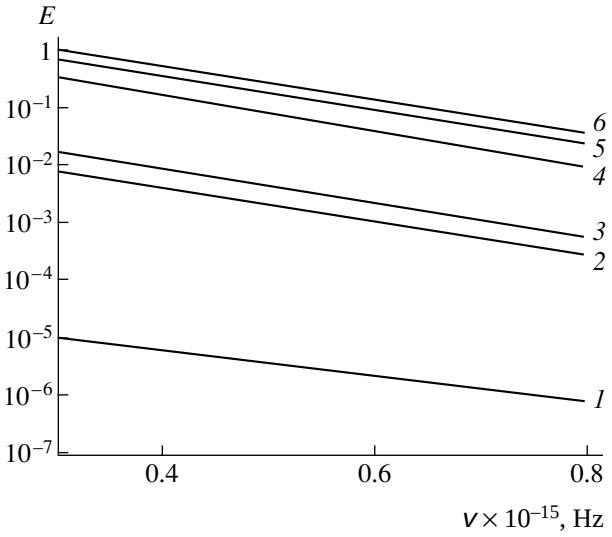

Fig. 2. The energy spectra of electromagnetic pulses observed at various angles $\theta = 6.4°$ (*1*), 0.3° (*2*), 3° (*3*), 5.5° (*4*), 5.8° (*5*), and $\arccos(c/v) = \arctan(0.1) \approx 5.71°$ (*6*) in the far zone ($Z = 50$ km) in the optical frequency range (3×10^{14}–8×10^{14} Hz) for $v/c \cong 1.005$.

The field of a model source moving with the velocity $v > c$ was numerically calculated using formula (4). The expansion of $B_\varphi(\rho, z, \varphi, \tau)$ in the Fourier integrals allowed the spectral energy densities of the electromagnetic field $E(v)$ in the far field zone to be obtained for various observation angles. Figure 2 shows the spectra of radiation at the angles $\theta = 0.3°$, 3°, 5.5°, $\arccos(c/v) = \arctan(0.1) \approx 5.71°$, 5.8°, and 6.4° in the far field zone ($Z = 50$ km) in the optical frequency range for $v/c \cong 1.005$.

To summarize, the main results are as follows. The shape of a current pulse propagating at a velocity

exceeding the speed of light in vacuum ($v/c \cong 1.005$) was determined and the radiation spectra observed at various angles in the optical frequency range were calculated. In the visible range, the radiation intensity is maximum at an angle $\theta \cong \arccos(c/v)$ relative to the direction of the current pulse propagation. Therefore, the angular dependence in the case under consideration is close to that of the Vavilov–Cherenkov radiation.

REFERENCES

1. E. Recami, Found. Phys. **31**, 1119 (2001).
2. V. V. Borisov and A. B. Utkin, J. Phys. D **28**, 614 (1995).
3. W. J. Karzas and R. Latter, Phys. Rev. **137** (5), B1369 (1965).
4. A. V. Manankova, Izv. Vyssh. Uchebn. Zaved. Radiofiz. **15**, 211 (1972).
5. V. I. Smirnov, *A Course of Higher Mathematics* (Nauka, Moscow, 1951; Addison-Wesley, Reading, 1964), Vol. 4.
6. F. F. Valiev, Zh. Tekh. Fiz. **71** (12), 92 (2001) [Tech. Phys. **46**, 1579 (2001)].
7. *GEANT User's Guide*, CERN DD/EE83-1.

Translated by P. Pozdeev

Technical Physics Letters, Vol. 30, No. 3, 2004, pp. 247–249. Translated from Pis'ma v Zhurnal Tekhnicheskoĭ Fiziki, Vol. 30, No. 6, 2004, pp. 67–72.

Features of the Mechanoluminescence of Thin Metal Films Excited by Long and Short Laser Pulses

A. F. Banishev*, V. Ya. Panchenko, and A. V. Shishkov

Institute for Problems of Laser and Information Technologies, Russian Academy of Sciences, Shatura, Russia

** e-mail: banishev@laser.nictl.msk.su*

Received September 5, 2003

Abstract—We have studied the strain-induced luminescence from thin fine-grained films of various metals under the action of short (subnanosecond) and long (millisecond) laser pulses. The possible mechanism of luminescence excitation is considered, according to which the emission is due to the interaction between grain boundary dislocations and impurities occurring in the intergranular region. *© 2004 MAIK "Nauka/Interperiodica".*

The phenomenon of strain-induced luminescence or mechanoluminescence (ML) has been studied predominantly by Abramova *et al.* [1–3] and Molotskiĭ [4]. Unfortunately, there are only a few papers devoted to elucidation of the mechanism of this emission. However, the ability of materials to produce luminescence during plastic straining is of considerable basic and applied value, for example, from the standpoint of investigation into the process of generation of structural defects and their interactions in the course of plastic deformation and fracture.

Previously [1–4], ML was treated as the emission of light quanta at the moment when a mobile dislocation escapes from the bulk of material to its surface. However, when the sample thickness is decreased to a micron and submicron level, the number of mobile (weakly trapped) dislocations in the bulk has to drop (dislocations emerge at the surface). For example, it is known [5] that there are virtually no dislocations in the volume of whiskers and thin films. Therefore, one might expect ML to be hindered in the case of thin films. The tendency of the threshold stress σ_{th} (a minimum stress for which the ML signal from a given sample is detected) to decrease with the sample thickness was in fact observed [6] in agreement with the notions about mobile dislocations involved in the excitation of ML in metals.

This Letter presents the results of experimental investigation of the ML from thin fine-grained films of various metals excited by pulsed thermal straining under the action of short (subnanosecond) and long (millisecond) laser pulses.

Each sample was mounted in a special holder immediately in front of a photomultiplier window. The ML was excited by a laser operating in two regimes with the output pulse parameters $\tau_{las.} \approx 1.4$ ms, $E_{max} \approx 3.5$ J (long pulses) and $\tau_{las.} \approx 0.3$ μs, $E_{max} \approx 1$ mJ (short pulses). The laser beam was focused on the sample surface in a spot with the diameter $2r_0 = 1.2$–2 mm. The emission was collected from the sample side opposite to that exposed to the laser action. The ML was measured by a photomultiplier sensitive in a wavelength range from 400 to 800 nm, spaced by 8–10 mm from the rear side of the sample. The output signal of the photomultiplier was fed to a digital oscillograph and a personal computer. The experiments were performed with 1- to 2-μm-thick fine-grained films of molybdenum, titanium, aluminum, and copper prepared by vacuum deposition onto glass substrates. The finest grain structure was observed for molybdenum, while aluminum and copper films were characterized by the maximum grain size.

Figure 1 shows the topographs of the surface of copper and molybdenum films studied in an atomic-force microscope (AFM). As can be seen, the films possess a fine-grained structure with a grain size of $d \approx 50$–150 nm for molybdenum and 150–250 nm for copper.

Figure 2 shows the oscillograms of ML signals from a molybdenum film excited by short and long laser pulses at an output power density $I_{las.}$ above the ML excitation threshold $I_{las.th}$ (defined as the minimum power of laser pulses for which an ML signal from a given film is detected). As can be seen, emission excited by a short laser pulse continues for a long time after termination of the laser action (i.e., the light is emitted from a cool metal surface). In the case of long pulses, ML starts and terminates during the laser action. The

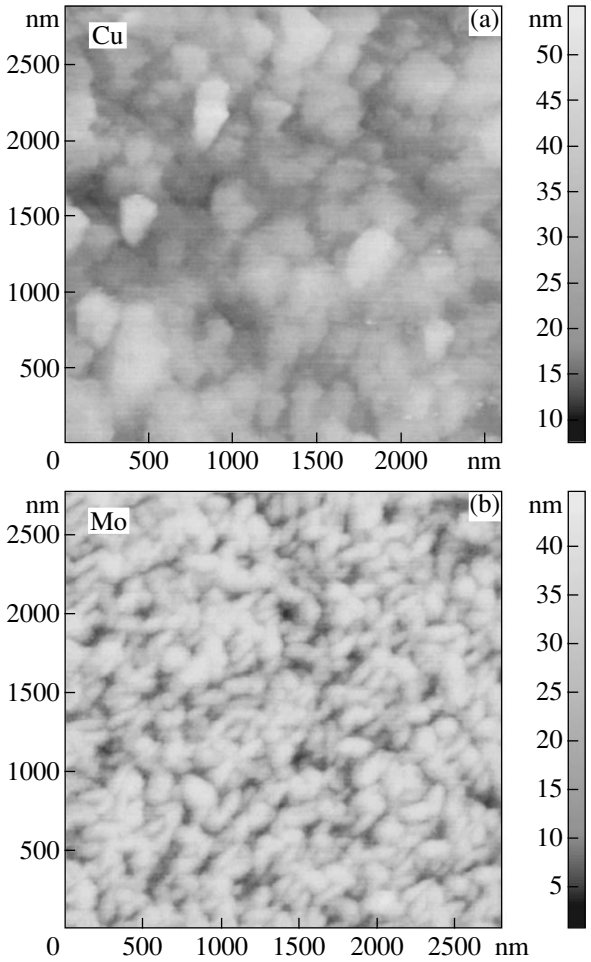

Fig. 1. AFM topographs of the surface of (a) copper and (b) molybdenum films.

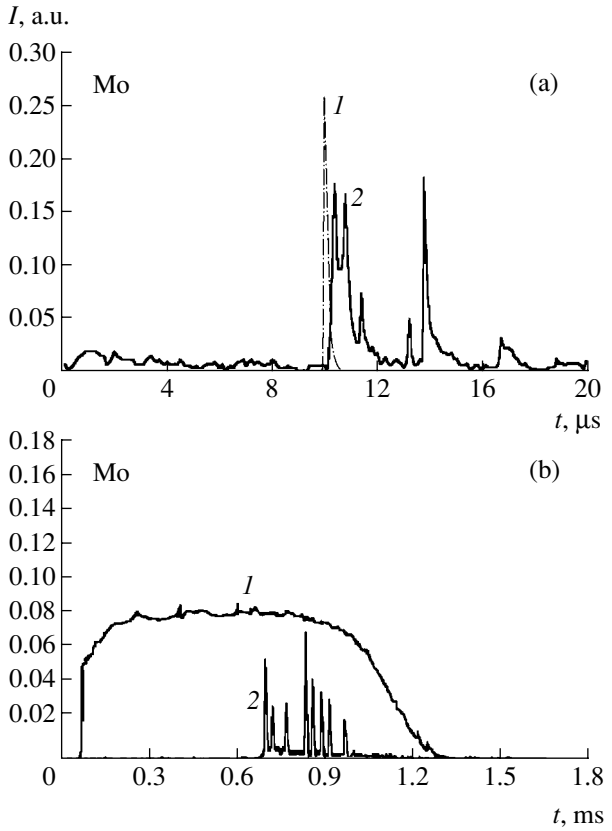

Fig. 2. Oscillograms of the ML signal from a 1-μm-thick molybdenum film excited by (a) short ($\tau_{las.} \approx 0.3$ μs) and (b) long (~1.4 ms) laser pulses: (*1*) laser pulse; (*2*) ML spikes.

intensity and duration of ML depend on the laser power density: the growth of $I_{las.}$ leads to an increase in both number and density of spikes in the ML signal.

A comparison of the ML signals excited by long and short laser pulses leads to the conclusion that the characteristic time of structural changes (relaxation of laser-induced internal stresses) during which the ML is excited is much longer than the duration of short laser pulses (~0.3 μs) and is comparable to or greater than the duration of long pulses (~1.4 ms). As is known, such long processes of relaxation of the laser-induced internal stresses are characteristic of the dislocation recovery. These results also show evidence in favor of the dislocation mechanism of ML excitation in metals.

However, the films studied in our experiments possess a rather small grain size (Fig. 1). As is known, metals with the grain size $d < 100$ nm exhibit certain peculiarities related to the fine-grained structure. In particular, the plastic straining in such materials proceeds predominantly by the mechanism of grain boundary sliding involving grain boundary dislocations [7–11]. The fact that all films studied in our experiments (possessing different energy band structures) exhibit ML in the visible spectral range under the action of plastic straining indicates that this phenomenon is virtually independent of the metal band structure (the metal type determines only the excitation threshold).

Recently [6], we suggested that the ML of fine-grained metals under the action of plastic straining is related to the interaction between grain boundary dislocations and impurities occurring in the intergranular region. On the whole, the results of this investigation of the ML of fine-grained films of various metals agree with this mechanism of ML excitation in fine-grained materials.

Acknowledgments. This study was supported by the Russian Foundation for Basic Research, project no. 02-02-17028.

REFERENCES

1. K. B. Abramova and I. P. Shcherbakov, Zh. Tekh. Fiz. **64** (9), 75 (1994) [Tech. Phys. **39**, 901 (1994)].

2. K. B. Abramova, I. P. Shcherbakov, I. Ya. Pukhonto, and A. M. Kondyrev, Zh. Tekh. Fiz. **66** (5), 190 (1996) [Tech. Phys. **41**, 511 (1996)].

3. K. B. Abramova, A. I. Rusakov, A. A. Semenov, and I. P. Shcherbakov, Fiz. Tverd. Tela (St. Petersburg) **40**, 957 (1998) [Phys. Solid State **40**, 877 (1998)].

4. M. I. Molotskiĭ, Fiz. Met. Metalloved. **55**, 43 (1983).

5. Yu. F. Komnik, *Physics of Metal Films* (Atomizdat, Moscow, 1979) [in Russian].

6. A. F. Banishev, V. Ya. Panchenko, and A. V. Shishkov, Zh. Tekh. Fiz. **73** (5), 90 (2003) [Tech. Phys. **48**, 612 (2003)].

7. O. A. Kaĭbyshev and R. Z. Valiev, *Grain Boundaries and Properties of Metals* (Metallurgiya, Moscow, 1987).

8. R. A. Andrievskiĭ and A. M. Glezer, Fiz. Met. Metalloved. **88**, 50 (1999).

9. R. A. Andrievskiĭ and A. M. Glezer, Fiz. Met. Metalloved. **89**, 91 (2000).

10. V. A. Pozdnyakov and A. M. Glezer, Fiz. Tverd. Tela (St. Petersburg) **44**, 705 (2002) [Phys. Solid State **44**, 732 (2002)].

11. V. A. Pozdnyakov and A. M. Glezer, Dokl. Akad. Nauk **384**, 177 (2002) [Dokl. Phys. **47**, 363 (2002)].

Translated by P. Pozdeev

Technical Physics Letters, Vol. 30, No. 3, 2004, pp. 250–252. Translated from Pis'ma v Zhurnal Tekhnicheskoĭ Fiziki, Vol. 30, No. 6, 2004, pp. 73–78.

Photosensitivity of the Semiconductor–Turpentine Heterocontact

S. I. Drapak and Z. D. Kovalyuk

Frantsevich Institute for Problems of Materials Science (Chernivtsy Department), National Academy of Sciences of Ukraine, Chernivtsy, Ukraine

e-mail: chimsp@unicom.cv.ua

Received September 22, 2003

Abstract—A heterocontact between a layered semiconductor (*p*-type indium monoselenide) and the natural organic compound turpentine has been created and studied for the first time. The electrical properties of this system are analogous to those of the metal–dielectric–semiconductor heterostructures, turpentine behaving like a *p*-type material. The heterojunction possesses a significant photosensitivity in the near infrared spectral range.

Organic compounds find increasing use in various technologies, including photoelectronics [1]. This stimulates the investigation into physical properties of synthetic and natural substances [2]. A special direction of research is devoted to the contacts between semiconductors and biological media [3, 4].

Below we present the results of the first investigation of a heterojunction between *p*-InSe and turpentine. Turpentine is a resinous substance (oleoresin) discharged from cut conifer trees and offers a valuable source of various technical products and biologically active compounds. In particular, turpentine is used in the production of some lacquers and is a raw material for obtaining camphor and immersion oil for optical microscopy. Natural turpentine is also used for obtaining rosin (a mixture of resin acids with the composition $C_{19}H_{29}OOH$) and technical turpentine (a mixture of terpenic unsaturated hydrocarbons with the general formula $C_{10}H_{16}$).

The samples were prepared using *p*-InSe:Cd substrates with a charge carrier density of $p \approx 10^{14}$ cm^{-3} at $T = 300$ K according to the Hall measurements. The choice of this semiconductor was determined by a number of factors, the main of which are (i) the possibility of obtaining plates with atomically smooth surface and low density of dangling bonds by cleavage of an InSe ingot in air and (ii) the ability of this semiconductor to form rectifying barriers in contacts with various materials possessing both lower (In_2O3) and higher (Au) electron work function [5].

The turpentine films were prepared by spraying an ethanol solution of turpentine onto freshly cleaved semiconductor substrates at room temperature. The thicknesses of propolis films varied from 10 to 30 μm and their specific conductivities were on the order of 10^{-10}–10^{-11} Ω^{-1} cm^{-1}. The electric contacts on both semiconductor and turpentine surfaces were obtained by depositing silver, which is known to provide for the best ohmic contacts with *p*-InSe [6].

Measurements of the stationary current–voltage (*J*–*V*) characteristics of the samples prepared as described above showed that the *p*-InSe–turpentine heterojunctions exhibit a clearly pronounced rectification effect: for a bias voltage of 1.5–2 V, the forward current exceeds the reverse current by about two orders of magnitude. The forward direction always corresponded to the bias voltage source minus on *p*-InSe, which indicate that turpentine in contact with InSe behaves as a *p*-type material.

Figure 1a (curves *1* and *2*) shows the typical *J*–*V* curve of the *p*-InSe–turpentine junction. Note that a

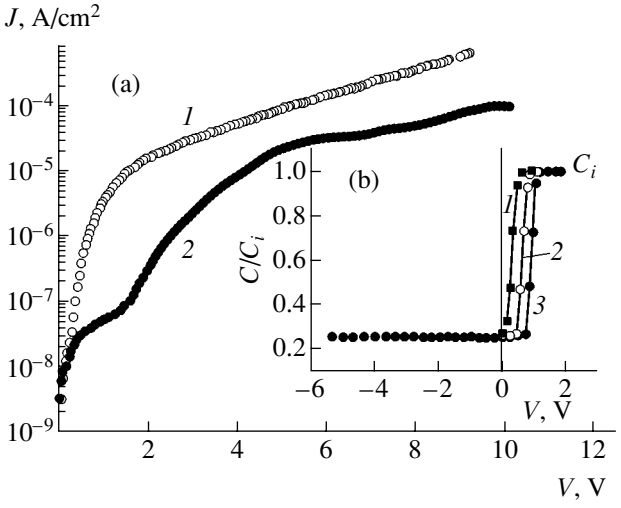

Fig. 1. Turpentine–*p*-InSe heterocontact (T = 295°C): (a) forward (*1*) and reverse (*2*) branches of the stationary current–voltage characteristic; (b) capacitance–voltage characteristics measured at various frequencies f = 10 (*1*), 20 (*2*), and 30 kHz (*3*).

1063-7850/04/3003-0250$26.00 © 2004 MAIK "Nauka/Interperiodica"

sharp increase in the current density observed on the reverse branch for $|V| \approx 1.75$–4.5 V is characteristic of the structures with a dielectric layer at the interface [7], while the appearance of "steps" on increasing the reverse bias voltage (Fig. 1a, curve *2*) is usually attributed to the resonance tunneling of charge carriers from the bulk of the base material (turpentine) via two sequential tunneling-transparent barriers in (i) a depleted part of the space charge region and (ii) the dielectric layer with intermediate participation of a quantum well formed by the conduction band of the base material [8].

The electrical parameters of the sample structures showed no signs of degradation after the moment of preparation (over six months). This stability may be evidence of the absence of irreversible chemical reactions both at the turpentine–semiconductor interface and in the turpentine layer. There are published data on the reversible chemical processes in turpentine, including those under illumination [9].

The capacitance–voltage (C–V) characteristics of the semiconductor–turpentine heterojunctions measured in a frequency range of f = 10–50 kHz were typical of the high-frequency C–V curves of heterostructures of the metal–dielectric–semiconductor type [7]. The absence of changes of the absolute value of capacitance C_i in the regime of accumulation of the majority carriers (Fig. 1b, curves *1–3*) upon a twofold or even more pronounced variation of the turpentine film thickness suggests that the biological medium exhibits separation in the course of polymerization with the formation of a less high-ohmic layer situated closer to the surface and a more high-ohmic transition layer (from the standpoint of electrochemistry, the Gouy–Chapman and Helmholtz layers). The latter layer is responsible for the observed behavior of C–V curves. The frequency dependence of the C–V characteristics of the *p*-InSe–turpentine heterojunction can be related both to the inertial character of current transfer in high-ohmic organic compounds [10] and to the influence of a large serial resistance of the heterostructure [11]. In the latter case, the contact potential difference determined from the C–V curve using the method described in [11] amounted to $\varphi_0 = 0.32 \pm 0.02$ eV, in good agreement with the saturation photo emf (V_{oc} = 0.27–0.32 V).

Under illumination with natural light, *p*-InSe–turpentine heterojunctions exhibit photo emf and the semiconductor acquires a negative charge, which is consistent with the forward current direction in the J–V characteristics. The photo emf direction depends neither on the wavelength nor on the position of the light spot on the sample surface. The magnitude of the photoresponse is greater when the heterostructure is illuminated from the side of the turpentine film.

Figure 2 (curves *1* and *2*) shows the typical spectra of the relative quantum efficiency $\eta(h\nu)$ determined as the ratio of the photocurrent to the number of photons incident onto a *p*-InSe–turpentine heterostructure. For comparison, we also present the analogous $\eta(h\nu)$ curves of the heterojunctions between *p*-InSe and the organic compounds representing the main turpentine components: technical turpentine and rosin (curves *3* and *4*, respectively). These curves are qualitatively similar to the spectra of photosensitivity of a number of heterojunctions between semiconductors and biological media (proteins, green leaves, etc.), for which the long-wavelength boundaries of the relative quantum efficiency spectra are determined by the semiconductor bandgap width [3]. Therefore, the observed spectra can be interpreted in a similar manner. Characteristic features of the $\eta(h\nu)$ curves of the *p*-InSe–turpentine heterostructure are a shift of the photosensitivity peak toward longer wavelengths relative to the semiconductor bandgap width (E_g = 1.2 eV at T = 300 K) and virtually identical spectra of photosensitivity observed for a sample illuminated from the semiconductor and turpentine sides. It should be noted that the optical absorption spectrum of turpentine measured at T = 300 K showed that the material is transparent in the wavelength range studied (~90% transmission for a ~30-μm-thick film). An analogous behavior was previously observed for a heterocontact of the same semiconductor with propolis, another natural organic compound [4].

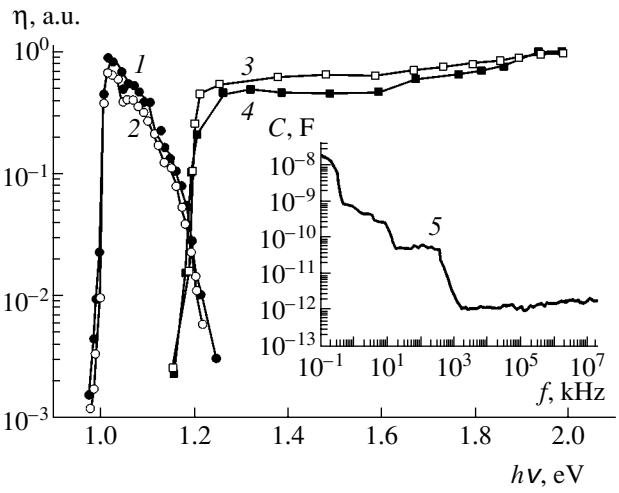

Fig. 2. The relative quantum efficiency spectra of photoconversion in the heterojunctions of *p*-InSe with (*1, 2*) natural turpentine, (*3*) technical turpentine and (*4*) rosin illuminated from the side of (*1, 3, 4*) organic layer and (*2*) semiconductor; (*5*) frequency dependence of the capacitance of a symmetric Ag–turpentine–Ag structure.

The appearance of photosensitivity beyond the fundamental absorption edge of a semiconductor crystal is possible in the presence of defects, for example, caused by the radiation damage [12]. However, the intensity of a photoconductivity signal in such cases is significantly lower as compared to that observed for the *p*-InSe–turpentine heterostructure. Probably, we observe an impurity photosensitivity of turpentine under the action of a space charge region occurring completely in this biological medium. The presence of several plateaus in the

frequency dependence of capacitance of a symmetric Ag–turpentine–Ag structure (Fig. 2, curve *5*) shows evidence of the presence of several deep levels in turpentine. However, verification of this assumption requires additional investigation.

Thus, we have demonstrated the principal possibility of using turpentine as a base material for photosensors operating in the near infrared range.

REFERENCES

1. T. A. Yourre, L. I. Rudaya, N. V. Klimova, and V. V. Shamanin, Fiz. Tekh. Poluprovodn. (St. Petersburg) **37** (7), 73 (2003) [Semiconductors **37**, 807 (2003)].
2. V. P. Grishchuk, S. A. Davidenko, I. D. Zholner, *et al.*, Pis'ma Zh. Tekh. Fiz. **28** (21), 36 (2002) [Tech. Phys. Lett. **28**, 896 (2002)].
3. V. Yu. Rud', Yu. V. Rud', and V. Kh. Shpunt, Pis'ma Zh. Tekh. Fiz. **25** (8), 76 (1999) [Tech. Phys. Lett. **25**, 328 (1999)].
4. S. I. Drapak, V. B. Orletskiĭ, Z. D. Kovalyuk, and V. V. Netyaga, Pis'ma Zh. Tekh. Fiz. **29** (20), 69 (2003) [Tech. Phys. Lett. **29**, 867 (2003)].
5. A. Segura, M. C. Martinez-Tomas, B. Mari, *et al.*, J. Appl. Phys. A **44**, 249 (1987).
6. S. I. Drapak, V. B. Orletskiĭ, Z. D. Kovalyuk, *et al.*, Pis'ma Zh. Tekh. Fiz. **29** (11), 86 (2003) [Tech. Phys. Lett. **29**, 480 (2003)].
7. S. Sze, *Physics of Semiconductor Devices* (Wiley, New York, 1981; Mir, Moscow, 1984), Vol. 2.
8. G. G. Kareva, M. I. Veksler, I. V. Grekhov, and A. F. Shulekin, Fiz. Tekh. Poluprovodn. (St. Petersburg) **36**, 953 (2002) [Semiconductors **36**, 889 (2002)].
9. V. A. Raldugin, V. V. Grishko, Yu. V. Gatilov, *et al.*, Sib. Khim. Zh., No. 5, 66 (1992).
10. G. Ferrari, D. Natali, M. Sampietro, *et al.*, Org. Electron. **3**, 33 (2002).
11. A. A. Lebedev, Jr., A. A. Lebedev, and D. V. Davydov, Fiz. Tekh. Poluprovodn. (St. Petersburg) **34**, 113 (2000) [Semiconductors **34**, 115 (2000)].
12. V. S. Vavilov, *Effects of Radiation on Semiconductors* (Fizmatgiz, Moscow, 1963; Consultants Bureau, New York, 1965).

Translated by P. Pozdeev

Technical Physics Letters, Vol. 30, No. 3, 2004, pp. 253–255. Translated from Pis'ma v Zhurnal Tekhnicheskoĭ Fiziki, Vol. 30, No. 6, 2004, pp. 79–86.

The Time of Synchronization of Oscillations in Two Coupled Identical Subsystems

A. A. Koronovskiĭ*, A. E. Hramov, and I. A. Khromova**

State Scientific Center "College," Saratov State University, Saratov, Russia

*e-mail: * alkor@cas.ssu.runnet.ru; ** aeh@cas.ssu.runnet.ru*

Received August 6, 2003

Abstract—The mechanism of synchronization of oscillations in two identical coupled flow systems has been studied. The time (past the coupling onset) during which a synchronous oscillation regime is established depends on the oscillation phase difference between the subsystems. Variation of the coupling parameter leads to a change in the character of dependence of the synchronization time on the phase difference. Several types of synchronization processes are revealed, which are realized for various values of the coupling parameter.

In recent years, the problem of synchronization of nonlinear dynamical systems, in particular, the synchronization of chaotic oscillations, has received much attention. The original papers by Pecora and Carroll [1, 2] inspired extensive research in this direction and the number of publications still rapidly increases. This interest is related to the fact that the phenomenon of synchronization is involved in a large number of problems possessing both basic and applied significance. Examples include secret data transmission [3–6] and numerous problems in biology [7, 8], chemistry [9], ecology [10], astronomy [11], etc.

Besides the investigations aimed at determining the values of control parameters providing for the synchronization, establishing the conditions of synchronism breakage [12], and confirming weak coupling between several subsystems [13], the attention of researchers has also been drawn to determining the time of settling synchronous oscillations [14, 15]. The interest in this problem has both theoretical and practical aspects. For example, in the case of secret data transmission using chaotic synchronization techniques, the knowledge of the time interval during which the synchronization takes place allows the useful information to be correctly extracted [4]. It was demonstrated for two identical coupled van der Pol oscillators (representing the simplest model systems) [14, 15] that the dependence of the time of complete synchronization on the coupling parameter obeys a power law; the results were illustrated by numerical estimates.

This study was aimed at establishing how strongly (if at all) the time of complete synchronization settling [16] in two identical coupled systems depends on the initial phase difference. Previously [17], we have demonstrated for two autooscillatory dynamical systems (van der Pol oscillator and distributed active medium of the "helical electron beam–backward electromagnetic wave" type) under external periodic action that the time of synchronism settling at a frequency of the external driving signal significantly depends on the phase difference between natural oscillations and the driving signal.

Let us consider, following [14, 15], a system of two van der Pol oscillators with unidirectional coupling,

$$\begin{aligned} \ddot{x} + d(1-x^2)\dot{x} + x &= 0, \\ \ddot{u} + d(1-u^2)\dot{u} + u &= K(u-x)\delta(t-t_0), \end{aligned} \tag{1}$$

where x and u are the dynamic variables characterizing the states of the first (driving) and second (driven) oscillator, respectively; $d = 0.3$ is the nonlinearity parameter; K is the coupling parameter; $\delta(\xi)$ is the Heaviside function; and t_0 is the moment of switching on the unidirectional coupling, before which the two systems evolved independently (the time t_0 is selected sufficiently large for the transient processes in both systems to cease and the imaging points in the phase space to attain their limiting cycles).

The system of equations (1) was numerically solved using the fourth-order Runge–Kutta method with a time step of $h = 0.001$. The period of time T_s to complete synchronization was determined as

$$T_s = t_s - t_0, \tag{2}$$

where t_s is the moment of time corresponding to the onset of complete synchronism. A criterion for the complete synchronization was selected in the following form:

$$\sqrt{(x-u)^2 + (\dot{x}-\dot{u})^2} \le 10^{-3}. \tag{3}$$

Figure 1 shows the characteristic plots of the period of time T_s, for which complete synchronism is settled in system (1) after switching on the coupling between two autooscillators, versus the initial phase $\varphi_x(t_0)$ of

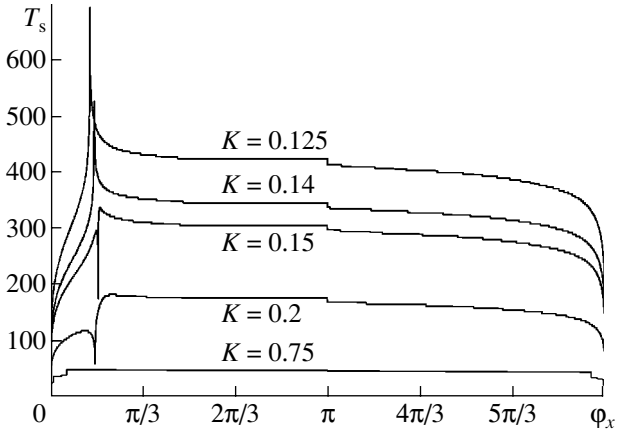

Fig. 1. Plots of the period of time T_s, for which complete synchronism is settled in system (1) after switching on the coupling between two autooscillators, versus the initial phase $\varphi_x(t_0)$ of oscillations of the first (driving) oscillator for various values of the coupling parameter K.

oscillations of the first (driving) oscillator. The moment of switching on the unidirectional coupling is chosen so that the phase $\varphi_u(t_0)$ of oscillations of the second (driven) oscillator would be zero. In fact, we study the dependence of the time to complete synchronization versus the initial phase difference $\varphi_x(t_0)$–$\varphi_u(t_0)$ between the driving and driven oscillations at the moment of coupling onset. The results of our investigations showed that a change in the initial phase $\varphi_u(t_0)$ of the driven oscillator leads to a shift of the T_s versus $\varphi_x(t_0)$ curve along the phase axis in the absence of any qualitative changes in the character of this dependence.

As can be seen from Fig. 1, the time to complete synchronization depends on the initial phase difference between driving and driven oscillators. Obviously, should the initial phase difference $\varphi_x(t_0)$–$\varphi_u(t_0)$ between the driving and driven oscillations be zero at the moment of coupling onset, the oscillations are synchronous from the very beginning and the time to synchronization is zero (Fig. 1).

For a nonzero initial phase difference, the time to complete synchronization of system (1) also differs from zero and changes rather weakly in a broad interval of variation of the initial phase $\varphi_x(t_0)$ of the driving oscillator. On the other hand, it can be clearly seen from the curves corresponding to small values of the coupling parameter K that there are intervals of the initial phase $\varphi_x(t_0)$ in which the T_s values significantly differ from the typical duration of synchronization. When the coupling parameters K are below certain critical value K_c (for the given control parameters, $K_c \approx 0.145$), there exists an initial phase of the driving oscillator $\varphi_x(t_0) = \varphi_c$ for which the time to synchronization significantly increases.

When the coupling parameter K increases above a certain critical level, the character of the T_s versus $\varphi_x(t_0)$ curves exhibits a qualitative change (see Fig. 1, curves for $K = 0.14$ and 0.15), whereby approximately the same initial phase φ_c of the driving oscillator brings a sharp minimum evidencing that the regime of complete synchronization at this point is attained significantly faster than in the typical case.[1] As the coupling parameter grows further, the time to complete synchronization decreases and all variations in the T_s versus $\varphi_x(t_0)$ curves vanish (see Fig. 1, curve for $K = 0.75$).

Let us consider peculiarities of the complete synchronization settling in system (1) with $K = 0.15$. For this coupling parameter, the curve of the time to complete synchronization T_s versus the initial phase of the driving oscillator $\varphi_x(t_0)$ exhibits a singularity at $\varphi_c = 0.547$ (Fig. 1). In the interval of initial phases of the driving oscillator $\varphi_x(t_0) \in (0, \varphi_c)$, the driven system behaves as follows (Fig. 2a). Initially, the oscillation amplitude sharply decreases and then gradually increases to approach the value corresponding to a stationary regime. This mechanism allows the mismatch between phases of the driving $\varphi_x(t)$ and driven $\varphi_u(t)$ subsystems to be eliminated. The phase trajectory reflecting the behavior of the driven subsystem winds on the limiting cycle from inside. A considerable fraction of time past the moment when the amplitude of oscillations in the driven system attained an initial value is spent for fine adjustment of the phase relation between the two oscillators.

For the initial phases of the driving oscillator $\varphi_x(t_0) \in (\varphi_c, 2\pi)$, the driven system behaves somewhat differently (Fig. 2c). It also sharply drops initially and then starts approaching the value corresponding to a stationary regime, but the phase trajectory winds on the limiting cycle from outside. The case of $\varphi_x(t_0) = \varphi_c$ corresponds to the boundary situation, whereby the system exhibits a change from the first to second scenario in behavior of the driven oscillator (Fig. 2b). This situation is optimum from the standpoint of synchronism settling: as soon as the amplitude of oscillations in the system reaches the value corresponding to a stationary regime, the phases of both subsystems turn out to be equal and no time is spent for their fine adjustment.

For smaller values of the coupling parameter K, the action of the first oscillator upon the second is insufficient to provide for realization of the above mechanism of the phase adjustment involving a sharp initial drop of the oscillation amplitude in the driven system, followed by gradual approach to the initial value and fine phase adjustment. With small K values, the amplitude of oscillations in the driven subsystem changes only slightly and the phase difference between oscillations in the two subsystems is eliminated very slowly. This results in a general increase in the time T_s required for synchronization and in a qualitative change in the char-

[1] It should be noted that variation of the coupling parameter K leads to small changes in the initial phase φ_c corresponding to a sharp difference of T_s from the typical value.

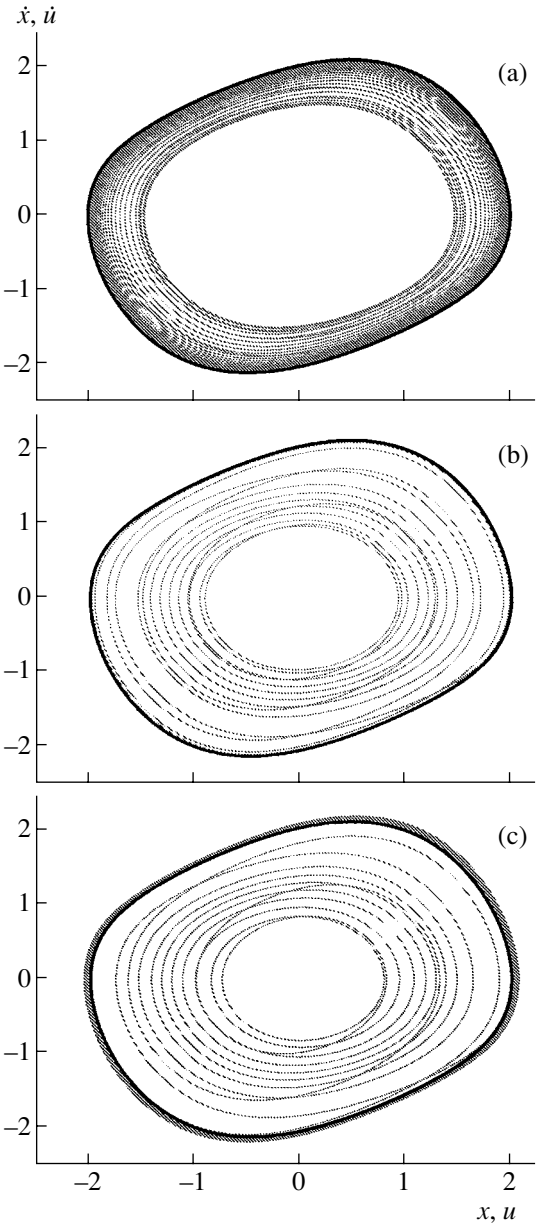

Fig. 2. Phase portraits illustrating the behavior of system (1) with the coupling parameter $K = 0.15$. The limiting cycle (thick solid curve) reflects behavior of the first (driving) oscillator in the coordinates $(x, \dot{x})$; light-gray phase trajectory shows the behavior of the second (driven) oscillator in the coordinates $(u, \dot{u})$ between the time moments t_0 and t_s. The initial phase $\varphi_u(t_0)$ of the driven oscillator is zero, while that of the driving oscillator is $\varphi_x(t_0) = 0.5$ (a), 0.547 ($\varphi_x = \varphi_c$) (b), and 0.55 (c).

acter of singularity (from minimum to maximum) at φ_c in the T_s versus $\varphi_x(t_0)$ curve.

Finally, for greater values of the coupling parameter K (see the curve for $K = 0.75$ in Fig. 1), the mechanism of synchronization settling is as follows. As the coupling is switched on, the driven subsystem exhibits a sharp change in the oscillation amplitude (initial drop followed by increase), at the expense of which the phase mismatch between the two subsystems is eliminated so that no fine adjustment is required. For this reason, the time to complete synchronization at large values of the coupling parameter K is virtually independent of the initial phase difference between the driving and driven oscillators.

Thus, we have demonstrated that the time of complete synchronism settling in two identical subsystems depends on the initial phase difference between these subsystems. It was shown that there are several mechanisms of synchronization, which are realized for various values of the coupling parameter K.

Acknowledgments. This study was supported by the Federal Program "Integration" (project no. B0057), the Program of Support for Leading Scientific Schools in Russia, and the Scientific-Education Center "Nonlinear Dynamics and Biophysics" at Saratov State University (Grant REC-006 from the US Civilian Research and Development Foundation for the Independent States of the Former Soviet Union).

REFERENCES

1. L. M. Pecora and T. L. Carroll, Phys. Rev. Lett. **64**, 821 (1990).
2. L. M. Pecora and T. L. Carroll, Phys. Rev. A **44**, 2374 (1991).
3. K. Pyragas, Phys. Rev. E **58**, 3067 (1998).
4. K. Murali and M. Lakshmanan, Phys. Rev. E **49**, 4882 (1994).
5. K. Murali and M. Lakshmanan, Phys. Rev. E **48**, R1624 (1993).
6. K. M. Cuomo and A. V. Oppenheim, Phys. Rev. Lett. **71**, 65 (1993).
7. D. É. Postnov and S. K. Khan, Pis'ma Zh. Tekh. Fiz. **25** (4), 11 (1999) [Tech. Phys. Lett. **25**, 128 (1999)].
8. V. S. Anishchenko, A. G. Balanov, N. B. Janson, *et al.*, Int. J. Bifurcation Chaos Appl. Sci. Eng. **10**, 2339 (2000).
9. P. Parmananda, Phys. Rev. E **56**, 1595 (1997).
10. B. Blasius and L. Stone, Int. J. Bifurcation Chaos Appl. Sci. Eng. **10**, 2361 (2000).
11. M. Palus, J. Kurths, U. Schwarz, *et al.*, Int. J. Bifurcation Chaos Appl. Sci. Eng. **10**, 2519 (2000).
12. N. J. Corron, Phys. Rev. E **63**, 055203 (2001).
13. M. G. Rosenblum, A. Pikovsky, and J. Kurths, IEEE Trans. Circuits Syst. **44**, 874 (1997).
14. P. Woafo and R. A. Kraenkel, Phys. Rev. E **65**, 036225 (2002).
15. H. K. Leung, Phys. Rev. E **58**, 5704 (1998).
16. V. S. Anishchenko, T. E. Vadivasova, and V. V. Astakhov, *Nonlinear Dynamics of Chaotic and Stochastic Systems* (Saratov. Gos. Univ., Saratov, 1999) [in Russian].
17. A. A. Koronovskiĭ, D. I. Trubetskov, and A. E. Khramov, Dokl. Akad. Nauk **389**, 749 (2003) [Dokl. Phys. **48**, 166 (2003)].

Translated by P. Pozdeev

Technical Physics Letters, Vol. 30, No. 3, 2004, pp. 256–258. Translated from Pis'ma v Zhurnal Tekhnicheskoĭ Fiziki, Vol. 30, No. 6, 2004, pp. 87–94.

Inhomogeneous Character of the Initial Stage of Ion Beam Deposition of Ultrathin Gold Films

A. I. Stognij*, N. N. Novitskii, O. M. Stukalov, A. I. Demchenko, and V. I. Khit'ko**

Research Institute of Radio Materials, Minsk, Belarus

Institute of Solid State and Semiconductor Physics, National Academy of Sciences of Belarus, Minsk, Belarus

*e-mail: * stognij@ifttp.bas-net.by; ** novitski@ifttp.bas-net.by*

Received June 18, 2003; in final form, August 12, 2003

Abstract—Gold films with thicknesses ranging from below 1 nm to 3 nm have been simultaneously deposited by the ion beam sputter technique onto the surface of glass substrates smooth on a subnanometer level and onto Si(001) substrates with nanodimensional inhomogeneities in the form of germanium atomic islands. Irrespective of the substrate surface nature, gold deposition initially leads to the formation of a stable layer with a thickness of several atomic monolayers. The gold films with thicknesses above 2 nm are continuous and homogeneous. Terminated in an intermediate stage, the sputter deposition of gold may result in the formation of an inhomogeneous layer of the island type. The results are interpreted taking into account the well-known fact that a high-energy component is present in the flux of the ion beam sputtered target material. © *2004 MAIK "Nauka/Interperiodica".*

As is known, the process of film nucleation on a substrate surface starts on a nanodimensional level and is not necessarily continuous [1, 2]. For this reason, the properties of films with thicknesses in the nanometer range are determined to a considerable extent by peculiarities of the initial deposition stage. The knowledge of the initial deposition stage is especially important for obtaining films with the properties required for particular practical applications. Transparent gold films with a thickness of several nanometers are widely used in multilayer film structures [1, 3], for the formation of transparent ohmic contacts [4, 5], for the investigation of the surface properties of dielectric materials by scanning electron microscopy [2], etc.

We have studied the process of nucleation of gold films on the surface of silicon plates with nanoislands of germanium formed by molecular beam epitaxy [6]. It was established that the surface of such plates contains nanoislands of two types, large (dome-shaped) and small (pyramidal), spaced by island-free surface areas smooth on a subnanometer level [6]. Therefore, using these samples, it is possible to study (e.g., in an atomic force microscope) the process of gold deposition simultaneously onto a subnanometer-smooth surface and onto areas of the same surface with nanodimensional inhomogeneities of certain size and shape. Using polished glass substrates in the same deposition cycle, it is possible to separate the contribution due to factors independent of the substrate nature.

The gold films were prepared using the ion beam sputter deposition technique. The experimental setup equipped with an ion beam source based on a two-stage self-sustained low-pressure gas discharge with a hollow cold cathode was described in detail elsewhere [5, 7]. A target was sputtered by a beam of argon ions with an energy of 0.8 keV at a beam current density of 0.15 mA/cm^2. The target was a plate of gold with a purity of no less than 99.99% Au. The residual vacuum in the working chamber was below 10^{-3} Pa, and the working pressure during deposition did not exceed 10^{-2} Pa. The flux of gold atoms sputtered from the target was deposited simultaneously onto substrates of two types. Substrates of the first type were prepared by cutting a Si(001) wafer with Ge nanoislands into 5 × 10-mm plates. Substrates of the second type were 20 × 20-mm glass plates with the surface polished by ion beam deposition–sputter cycles to a subnanometer level of smoothness [3].

The surfaces of the initial substrates and deposited gold films were studied using a Femtoscan-001 atomic force microscope (AFM) (Advanced Technology Center, Moscow State University, Moscow). A sample surface area of up to 5 × 5 μm was scanned in a contact mode with a silicon cantilever of the CSC12 type (MicroMasch, www.spmtips.com). The film resistivities ρ determined by the four-point-probe technique for the samples on glass substrates were within 10 kΩ/□. The optical transmission spectra of the same samples in the 300–500 nm range were measured on a Hitachi-340 spectrophotometer.

Figure 1 shows the typical AFM images of a silicon substrate with germanium nanoislands before (a) and after (b–d) gold deposition for a certain period of time: 10 (b), 15 (c), and 20 s (d). An analysis of the AFM images shows that the island-free areas of the initial

substrates are smooth (Fig. 1a). Large dome-shaped islands have a height of about 12 nm and an average lateral size (full width at half-height) of about 62 nm. The lateral size and height distributions of small pyramidal islands reveal two groups: first, with an average lateral size of 35 nm and a height of about 2 nm and, second, with these dimensions of 45 and 4.5 nm, respectively.

After ion beam sputter deposition of gold for 10 s, the height of the dome-shaped islands on silicon decreases to 10 nm, while their average lateral size increases to 88 nm (Fig. 1b). Analogous changes are observed for the pyramidal islands. The trends of decreasing height and increasing lateral size lead to some uncertainty in dividing the islands into groups for statistical analysis. The island-free substrate surface (Fig. 1b) becomes more rough than the initial one, but the size of inhomogeneities does not exceed 1.5 nm. The surface of a glass substrate after 10-s deposition acquires blue color and has a surface resistivity of 1.8–2 kΩ/□ and a transmission on a level of 85% (Fig. 2, curve *1*).

When the time of continuous gold deposition is increased to 15 s, the silicon substrate appears as uniformly covered with small roughnesses with a height of up to 3 nm and a lateral size within 10–25 nm over the entire area, except for the apices of dome-shaped islands, the heights and lateral dimensions of which decrease to 7 and 48 nm, respectively (Fig. 1c). Most of the pyramidal islands cannot be distinguished on this general background, because their average dimensions are comparable with those of inhomogeneities appearing after gold deposition. The inhomogeneities are electrically insulated from one another: the surface resistivity of such film on a glass substrate exceeds 10 kΩ/□. Gold films on the glass substrate upon a 15-s deposition exhibit gray color and have a transparency below 75% (Fig. 2, curve *2*).

After continuous deposition of gold for 20 s, the areas between islands on silicon substrates again appear smooth (Fig. 1d). The dome-shaped islands are still decreased in height (relative to the initial value) on the average to 7.4 nm, but their average lateral size increases to 90 nm (Fig. 1d). The gold films upon a 20-s deposition on a glass substrate have a surface resistivity of 350–400 Ω/□, possess a deep blue color, and have a transmission on a level of 80% (Fig. 2, curve *3*). Further increase in the time of continuous disposition leads to a decrease in the height of dome-shaped islands on silicon substrates, spreading of their lateral dimensions, and merging of these islands together. The corresponding coatings on glass substrates acquire a yellow tint and the surface resistivity decreases below 100 Ω/□.

The results described above show that the ion beam sputter deposition of gold initially leads to the formation of a continuous film with a thickness up to 3–4 atomic monolayers, irrespective of the substrate type. This film remains stable if the deposition process is terminated. Thicker coatings may separate, upon termination of the

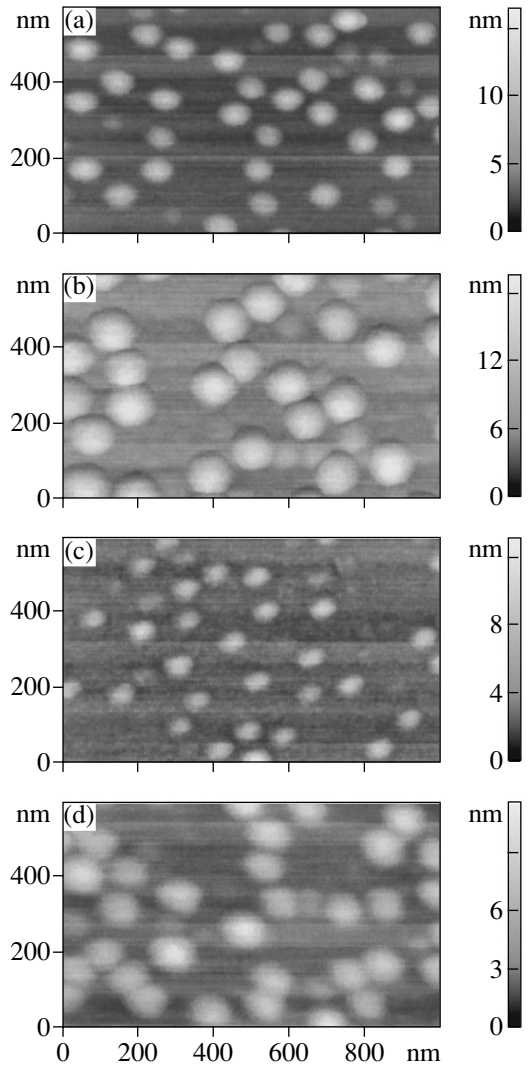

Fig. 1. Typical AFM images of a silicon substrate with germanium nanoislands before (a) and after (b–d) gold deposition for 10 (b), 15 (c), and 20 s (d).

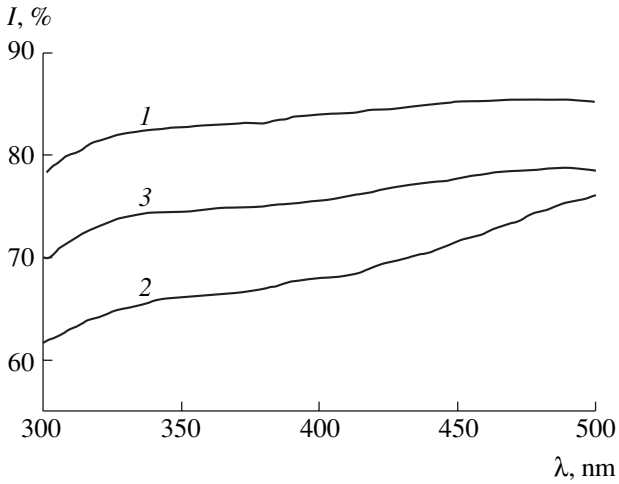

Fig. 2. Optical transmission of gold films deposited for 10 (*1*), 15 (*2*), and 20 s (*3*) onto glass substrates.

deposition process, into isolated islands with a height of about 3 nm. No such island formation is observed and the gold coating appears as a continuous film if the continuous deposition time increases and the deposit thickness is comparable with or greater than the height of these islands. Smearing of the images of pyramidal islands and their spreading and merging together are indicative of the preferred gold deposition into depressions of the surface relief (Figs. 1b and 1d).

Considerable changes in the state of gold films in the initial deposition stages and problems related to the correct determination of thicknesses of such ultrathin films are probably among the factors responsible for the discrepancies of some results reported in literature. When the gold film thicknesses were evaluated based on the deposition time, gold islands of close lateral dimensions were observed for the films with conditional thicknesses of 0.8 nm [8] and 0.4 nm [5]. According to [4], gold films with a conditional thickness of 6 nm had a transmission of up to 85% at a wavelength of 470 nm. In our study, the film thicknesses were evaluated based on the step height in the vicinity of round wells formed on glass substrates as described in [9]. The results of our AFM measurement showed that a 20-s deposition leads to the formation of a gold films with a thickness no greater than 2.4–2.6 nm and a transparency not exceeding 80% (Fig. 2, curve *3*).

Thus, by terminating the ion beam sputter deposition process, it is possible to separate three steps in the initial stages of growth of the gold films. By the order of appearance and the exterior of deposit, these steps can be identified with the film growth stages as described within the framework of the Stranski–Krastanov model [1, 2]. According to this model, a thin continuous stable layer is formed in the first stage. This is followed by the formation of islands as a result of stress relaxation at the film-substrate interface. Finally, a uniform growth of the film takes place.

However, our results reveal two significant differences from the well-known model. The first is a relatively large thickness of the initial continuous film. A possible explanation is related to the effect of "auto-radiation" of the deposited gold flux. Previously [3], we suggested that this effect may account for the appearance of cobalt atoms inside a copper matrix upon the ion beam sputter deposition using cobalt–copper alloy targets [10]. The essence of the "auto-radiation" effect consists in that the average energy of atoms in the flux of sputtered material is on the order of several electronvolts, while the high-energy "tail" extends up to several dozens of electronvolts [11]. Thus, a considerable fraction of atoms in the deposited flux possess energies exceeding the binding energies of atoms in the known materials [12]. Therefore, a part of the high-energy gold atoms in the deposited atomic flux are capable of producing point defects on the substrate surface (in the initial deposition stage) and within several atomic monolayers of the deposit (in the subsequent stages). The former circumstance improves the adhesion of the film to substrate, which explains the formation of a stable continuous film with a thickness of several atomic monolayers (Fig. 1b). The latter circumstance suggests that two to four surface monolayers of gold contain (and retain, in case of termination of the deposition process) additional structural disorder caused by stopping high-energy atoms contained in the deposited flux. If the deposition process is terminated at a moment when the thickness of damaged layers is comparable with that of the previously deposited layer, the deposit may exhibit a transition to a more equilibrium island film (Fig. 1c).

The second difference from the Stranski–Krastanov model is that no island formation is observed if the deposition process is conducted continuously or terminated at a late stage. Indeed, the effect of the surface damage on the equilibrium state of a deposit decreases with increasing thickness. For this reason, the islands are not formed when the deposition process is terminated after a sufficiently long time (Fig. 1d).

Acknowledgments. The authors are grateful to Dr. D. Grützmacher (Paul Scherrer Institute, Switzerland) for kindly providing the heterostructures with germanium on silicon.

REFERENCES

1. *Thin Films: Interdiffusion and Reactions*, Ed. by J. M. Poate, K. Tu, and J. Meier (Wiley, New York, 1978; Mir, Moscow, 1982).
2. L. Feldman and J. Mayer, *Fundamentals of Surface and Thin Films Analysis* (Elsevier, New York, 1986; Mir, Moscow, 1989).
3. A. I. Stognij, N. N. Novitskii, and O. M. Stukalov, Pis'ma Zh. Tekh. Fiz. **29** (2), 6 (2003) [Tech. Phys. Lett. **29**, 43 (2003)].
4. J. K. Sheu, Y. K. Su, G. C. Chi, *et al.*, Appl. Phys. Lett. **74**, 2340 (1999).
5. A. I. Stognij, N. N. Novitskii, S. D. Tushina, and S. V. Kalinnikov, Zh. Tekh. Fiz. **73** (6), 86 (2003) [Tech. Phys. **48**, 745 (2003)].
6. O. Leifeld, R. Hartmann, E. Müller, *et al.*, Nanotechnology **10**, 122 (1999).
7. A. I. Stognij, V. T. Svirin, S. D. Tushina, *et al.*, Prib. Tekh. Éksp., No. 3, 151 (2001).
8. É. I. Tochitskiĭ, *Crystallization and Thermal Processing of Thin Films* (Nauka i Tekhnika, Minsk, 1976).
9. A. I. Stognij, N. N. Novitskii, and O. M. Stukalov, Pis'ma Zh. Tekh. Fiz. **29** (4), 39 (2003) [Tech. Phys. Lett. **29**, 147 (2003)].
10. A. I. Stognij, S. V. Koryakin, and N. N. Novitskii, Zh. Tekh. Fiz. **73** (4), 117 (2003) [Tech. Phys. **48**, 496 (2003)].
11. M. V. Thompson, Nucl. Instrum. Methods Phys. Res. B **18**, 411 (1987).
12. C. Kittel, *Introduction to Solid State Physics*, 5th ed. (Wiley, New York, 1976; Nauka, Moscow, 1978).

Translated by P. Pozdeev